Fermilab

FERMILAB-THESIS-2003-12

Università degli Studi di Ferrara

Facoltà di Scienze Matematiche, Fisiche e Naturali

Measurement of the branching ratios $\psi' \to J/\psi X$ in the experiment E835 at FNAL

Matteo Negrini

Advisor
Chiar. mo Prof. Roberto Calabrese

XIV Ciclo del Dottorato di Ricerca in Fisica
1999-2002

Ai miei familiari

Contents

Introduction

The discovery of charmonium, the bound state of charm quark and its antiquark ($\bar{c}c$), in 1974 was the first evidence of the existence of heavy quarks ($m_c \simeq 1.5$ GeV). Since that moment the spectroscopy of heavy quarkonium has been a very interesting source of informations on the nature of the strong interaction: in the $\bar{Q}Q$ annihilation, quantum chromodynamics (QCD) is expected to apply as a perturbative theory, even if with approximations, and the large mass of the quark (and antiquark) allow a non relativistic approach for the study of the strong binding potential to describe the quarkonium mass spectrum.

The E835 experiment at Fermilab studies the spectroscopy of charmonium states formed in $\bar{p}p$ annihilation. The technique was pioneered at CERN by the experiment R704 and then continued at Fermilab with E760 detector and its upgrade E835, which collected data in 2 periods called E835-I (years 1996-97) and E835-II (year 2000). At e^+e^- colliders, only $J^{PC} = 1^{--}$ states can be directly formed because the lepton pair annihilation proceeds through a virtual photon; the advantage of charmonium spectroscopy in $\bar{p}p$ annihilation is that with this technique all $\bar{c}c$ states are directly accessible. These experiments have to deal with a large hadronic background; however a clean charmonium decay signal can be obtained by looking at electromagnetic final states.

The ψ' (2^3S_1 charmonium state) has the same quantum numbers of the J/ψ , therefore it can be produced in e^+e^- annihilation and, for this reason, it is one of the $\bar{c}c$ states studied in more detail. Its decay modes are similar to those of the J/ψ , as expressed by the well known "12% rule"; however, in addition, it presents radiative decays to $\chi_{cJ}\gamma$ and hadronic deexcitation to a J/ψ , accompanied by the emission of light hadrons. All these additional decay modes explain the larger total width with respect to the J/ψ . Most of the measurements of the ψ' branching ratios to the various J/ψ inclusive decay modes have been done without the full reconstruction of the final state. Moreover, the only experiment that obtained a branching ratio measurement for all the $J/\psi X$ channels on the same data sample is E760.

In this thesis the branching ratios (BR) of the ψ' are measured on a sample of 14.4 pb^{-1} of integrated luminosity collected by E835-II, identifying charmonium decay events from the presence of a high invariant mass e^+e^- pair. The channels

studied are:

$$\begin{aligned}
\psi' &\rightarrow e^+e^-, \\
\psi' &\rightarrow J/\psi X \rightarrow e^+e^- X, \\
\psi' &\rightarrow J/\psi\pi^+\pi^- \rightarrow e^+e^-\pi^+\pi^-, \\
\psi' &\rightarrow J/\psi\pi^0\pi^0 \rightarrow e^+e^- 4\gamma, \\
\psi' &\rightarrow J/\psi\eta \rightarrow e^+e^- 2\gamma,
\end{aligned}$$

and so, for the first time after E760, all the J/ψ inclusive channels are studied on the same data sample[1], providing a complete and consistent view of the ψ' hadronic deexcitation modes. The main difference with E760 is that, because of the improved tracking system, it is also possible to study the features of the $J/\psi\pi^+\pi^-$ channel using a kinematic fit reconstruction of the events.

With this measurement it is also possible to establish the scale of isospin breaking in the strong interaction, measuring the ratio $\mathcal{B}(\psi' \rightarrow J/\psi\pi^0\pi^0)/\mathcal{B}(\psi' \rightarrow J/\psi\pi^+\pi^-)$ which should be 0.5 in the case of perfect isospin conservation.

Chapter 1 is an introduction to charmonium spectroscopy, with a description of the potential models that have been developed to describe the mass spectrum and a look to the various typologies of charmonium decay channels. The phenomenology of ψ' decay modes, for all the channels analized in this thesis, is presented in more detail in Chapter 2, where all the branching ratio measurements obtained by different experiments are briefly described. The chapter also contains some experimental results concerning the dipion invariant mass and the π angular distributions for the $\psi' \rightarrow J/\psi\pi\pi$ decay. The experimental technique, the $\overline{p}$ beam and the detector setup are the subject of Chapter 3. In Chapter 4 the event selection and the background evaluation for all the analized channels is presented and in Chapter 5 all the selection efficiencies are evaluated and used to obtain the measurements of the ψ' BR, which represent our final result. Given the high luminosity collected, it is also possible to obtain a measurement of the dipion invariant mass distribution for both the $J/\psi\pi^+\pi^-$ and $J/\psi\pi^0\pi^0$ channels, as presented in the last chapter.

[1] With the only exception of $J/\psi\pi^0$, because of its very small branching ratio.

Chapter 1

The Charmonium

Until 1974 all the known hadrons were composed by three quark flavors: the "up" (u), "down" (d) and "strange" (s), with masses of a few MeV for the first two and of $\sim 100 \div 200$ Mev for the strange. In 1974, with the discovery of a massive and narrow resonance called J/ψ [1] [2], the existence of a new quark flavor called "charm" (c), with a mass of the order of 1 GeV was demonstrated.

The J/ψ is a member of a family of particles called "charmonium", bound state of charm quark and antiquark ($\bar{c}c$). Since 1974, quarkonium production and decay is one of the most interesting field to test the quantum chromodynamics (QCD), the field theory of the strong interaction, in particular some effective theories like perturbative QCD (PQCD) and, more recently, the non relativistic QCD (NRQCD).

Quarkonium is a good testing ground for QCD because the energy levels are due to the strong interaction. In particular, the heavy quarkonium systems ($\bar{Q}Q$, where Q can be either c, the charm, or b the bottom flavor) can be treated with non-relativistic models for the two valence quarks, with a great semplification of the theoretical treatment.

When two particles form a bound state, the attractive potential can be studied measuring the energy spectrum of the system. In atomic physics, the binding energy of the electron-nucleus system depends on the orbital angular momentum (L), spin (S) and total angular momentum ($J = L + S$) state (neglecting the nucleus angular momentum I). To classify the energy levels of the system the spectroscopic notation $n^{2S+1}L_J$ is used. A similar pattern of energy levels is present in positronium (the e^+e^- bound state); this has been used to study the potential between the electron and the positron.

The same concept can be applied also to the mesons: the quark-antiquark ($\bar{q}q$) bound states. Also in this case the spectroscopic notation $n^{2S+1}L_J$ for the classification of the mesons is used.

The intrinsic parity P and charge conjugation C of a charmonium state are

	$n^{2S+1}L_J$	J^{PC}	M (MeV)	, (MeV)
η_c	1^1S_0	0^{-+}	2979.7 ± 1.5	$16.0^{+3.6}_{-3.2}$
J/ψ	1^3S_1	1^{--}	3096.87 ± 0.04	0.087 ± 0.005
χ_0	1^3P_0	0^{++}	3415.1 ± 0.8	16.2 ± 2.3
χ_1	1^3P_1	1^{++}	3510.51 ± 0.12	0.92 ± 0.13
χ_2	1^3P_2	2^{++}	3556.18 ± 0.13	2.08 ± 0.17
h_c	1^1P_1	1^{+-}	3526.14 ± 0.24	< 1.1 (90%C.L.)
η_c'	2^1S_0	0^{-+}	3594 ± 5	< 8.0 (95%C.L.)
ψ'	2^3S_1	1^{--}	3685.96 ± 0.09	0.300 ± 0.025

Table 1.1: Quantum numbers, masses and width of the charmonium states with mass below the open charm production threshold (PDG 2002 fit values [3]). Recently E835 measured $M_{\chi_0} = 3415.4 \pm 0.4 \pm 0.2$ MeV and , $_{\chi_0} = 9.8 \pm 1.0 \pm 0.1$ MeV [4]. , $_{\chi_0}$ is in disagreement with the PDG 2002 but it is the most precise measurement available today.

related to the angular momentum by the relations:

$$P = (-1)^{L+1},$$
$$C = (-1)^{L+S},$$

and so also the J^{PC} notation can be used to classify the $\bar{c}c$ states.

The charmonium is the most widely studied heavy quarkonium system. Anyway some of the details of its spectrum (shown in Figure 1.1) are unknown or measured with large errors. Better measurement of the $\bar{c}c$ spectrum could lead to a better understanding of the strong interaction. Some of the features of charmonium states are summarized in Table 1.1.

1.1 Mass spectrum and potential models

Even though the charmonium mass spectrum is qualitatively similar to the positronium spectrum, the non perturbative features of QCD prevent the possibility of describing it on the basis of the fundamental theory of the interaction. For this reason the natural approach to the charmonium spectroscopy is to build an effective potential model describing the observed mass spectrum . This approximation allow to integrate out many fundamental effects like gluon emission or light quark pairs and to deal with an effective potential which is the result of the $\bar{Q}Q$ direct interaction as well as the energy of the gluon field. This potential should nevertheless reproduce the two main features of the bound quark states in the two limits of small and large distance: asymptotic freedom and confinement.

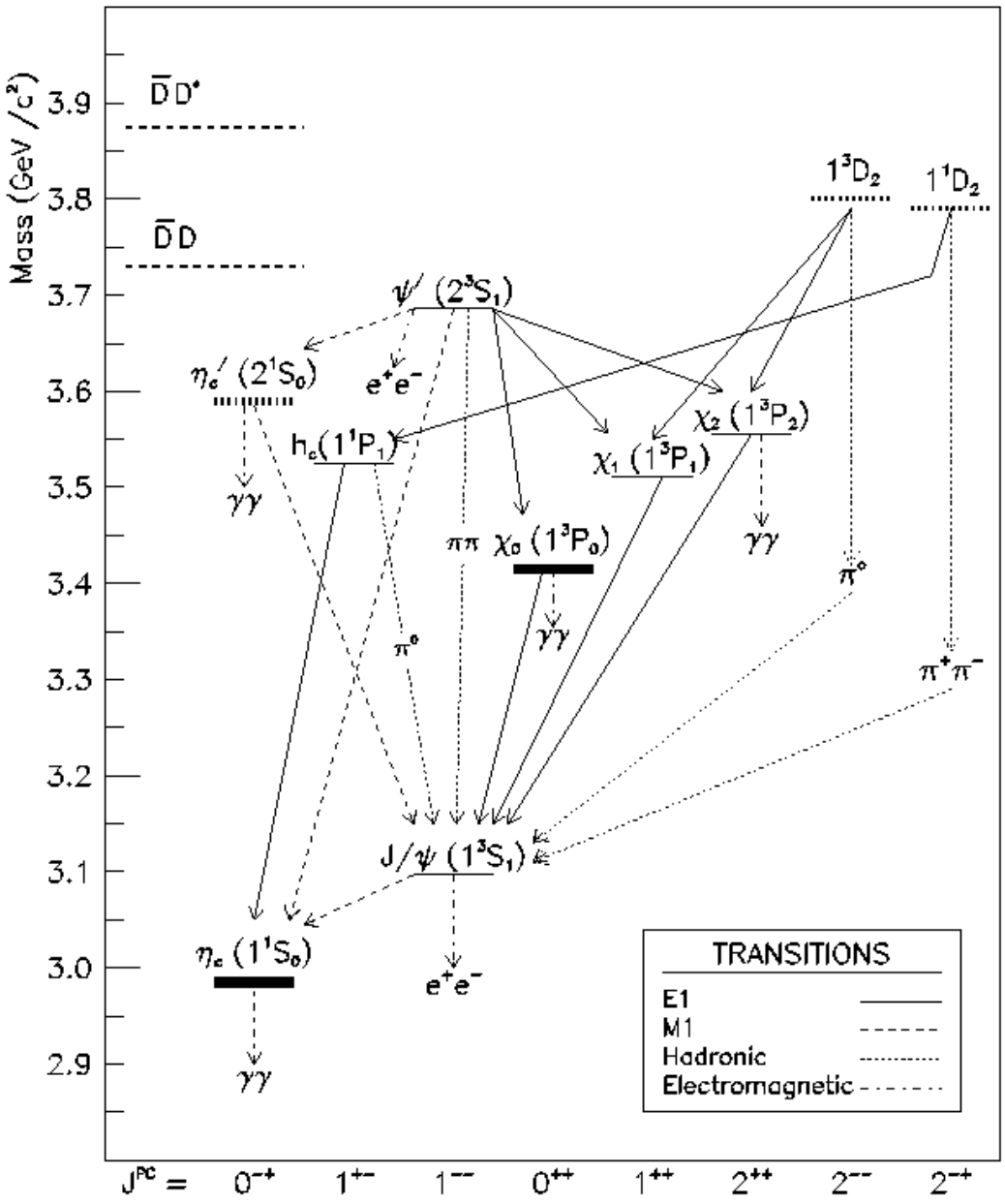

Figure 1.1: The charmonium spectrum.

Any potential written in this way must be flavor independent, so the following discussion made for the charmonium spectrum can be applied directly also to the bottomonium.

The $\bar{c}c$ system can be described with a Schrödinger equation:

$$H\Psi(x) = E\Psi(x),$$

where the hamiltonian for the $\bar{c}c$ system can be written as:

$$H = H_0 + H'$$

and H_0 can be expressed by a free particle hamiltonian plus a non-relativistic potential $V(r)$:

$$H_0 = 2m_c + \frac{p^2}{m_c} + V(r),$$

where m_c is the charm quark mass and p its momentum. H' includes the spin and orbital dependent part of the strong interaction, explaining the charmonium fine structure.

$V(r)$ can be built thinking at the properties of strong interaction in the limit of small and large distances. At small distance the potential between the quarks is coulomb-like:

$$V(r) \sim -\frac{4}{3}\frac{\alpha_s(r)}{r},$$

where r is the distance between the quarks and α_s is the strong coupling constant.

The value of the running coupling constant α_s depends on the energy scale of the interaction μ in the way shown in Figure 1.2. At the leading order in the inverse power of $\ln(\mu^2/\Lambda^2)$, it is described by:

$$\alpha_s(\mu) = \frac{4\pi}{\beta_0 \ln(\mu^2/\Lambda^2)}, \qquad (1.1)$$
$$\beta_0 = 11 - \frac{2}{3}n_f,$$

where $\Lambda \simeq 0.2$ GeV is the non-perturbative scale of QCD (the energy where (1.1) diverges) and and n_f is the number of quarks lighter than the energy scale μ. It is clear from Equation (1.1) that, as the energy scale of a strong process decrease and become closer to Λ, α_s increases and the QCD can not be treated as a perturbative theory.

At large distance the "confinement" term is dominating. It can be written in the form:

$$V(r) \sim kr,$$

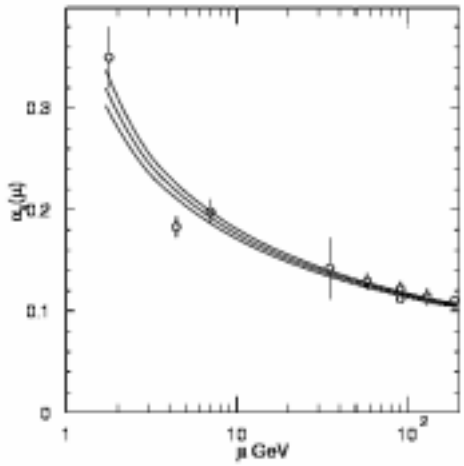

Figure 1.2: Behavior of $\alpha_s(\mu)$ [3].

where $k \simeq 1$ Gev $\cdot$ fm^{-1} is called string constant. The energy of a $\bar{q}q$ system increase with the distance so the absence of free quarks in nature is explained by the confinement term.

The two behaviors can be put together to write the Cornell potential, shown in Figure 1.3 [5]:

$$V(r) = -\frac{4}{3}\frac{\alpha_s(r)}{r} + kr. \tag{1.2}$$

With this potential, the charmonium wave function can be expressed as:

$$\Psi(r, \theta, \phi) = R_{nl}(r) Y_l^m(\theta, \phi) \tag{1.3}$$

but this is not enough accurate to reproduce the mass difference for charmonium states in the same orbital angular momentum or spin multiplets. To explain the charmonium fine structure one needs additional interaction terms depending on S and L [6]:

$$H' = V_{LS} + V_{SS} + V_{tens}; \tag{1.4}$$

the various terms are described in the following:

1. **spin-orbit:** the spin orbit term splits the states with the same orbital angular momentum depending on the $\langle \boldsymbol{L} \cdot \boldsymbol{S} \rangle$ expectation value (fine structure):

$$V_{LS} = (\boldsymbol{L} \cdot \boldsymbol{S}) \left(3\frac{dV_V}{dr} - \frac{dV_S}{dr} \right) / (2m_c^2 r),$$

where V_S and V_V are the scalar and vector components of the non-relativistic potential $V(r)$;

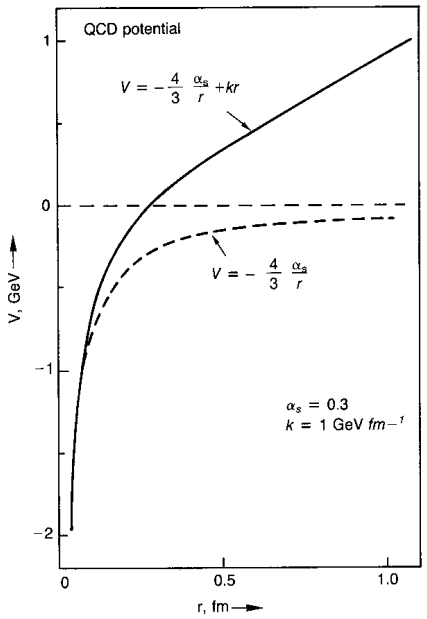

Figure 1.3: Cornell potential.

2. **spin-spin:** this term describes the effect of the interaction between the spin of the quarks and is responsible of the splitting between the spin singlet and triplet (hyperfine structure):

$$V_{SS} = \frac{2(\boldsymbol{S_1} \cdot \boldsymbol{S_2})}{3m_c^2}\nabla^2 V_V(r),$$

the expectation value for $\boldsymbol{S_1} \cdot \boldsymbol{S_2}$ is $+1/4$ for $S = 1$ and $-3/4$ for $S = 0$;

3. **tensor:** the tensor potential, in analogy with electrodynamics, contains the tensor effects of the vector potential:

$$V_T = \frac{S_{12}}{12m_c^2}\left(\frac{1}{r}\frac{dV_V}{dr} - \frac{d^2V_V}{dr^2}\right),$$

$$S_{12} = 2[3(\boldsymbol{S} \cdot \hat{\boldsymbol{r}})(\boldsymbol{S} \cdot \hat{\boldsymbol{r}}) - S^2].$$

The Coulomb-like part of $V(r)$ corresponds to one gluon exchange and contributes only to the vector part V_V of the potential; the scalar part V_S is due to the linear confining potential. The linear confining term could in principle contribute to both V_S and V_V but the fit of the χ_{cJ} masses suggest that the V_V contribution is small [7].

R	$M_R - M_{J/\psi}$ (MeV)			
	PDG 2002	MB (1983) [7]	GRS (1989) [8]	GJRS (1994) [9]
η_c	-117.2 ± 1.5	-113	-115.8	-109.0
χ_0	318.2 ± 0.8	285	315.3	318.6
χ_1	413.64 ± 0.13	391	410.1	414.4
χ_2	459.31 ± 0.14	428	456.6	459.1
h_c	429.27 ± 0.24	405	421.6	429.4
η_c'	497 ± 5	490	522.2	525.4
ψ'	589.07 ± 0.13	560	592.8	588.9

Table 1.2: Charmonium mass states splitting (with respect to the J/ψ). Theoretical predictions obtained with the potential models and comparison with the experimental values.

Other suggestions for the functional form of the binding potential $V(r)$ exist, but they are essentially coincident with the values from (1.2) in the region from 0.1 to 1.0 fm, the dimension scale of the $\bar{c}c$ system, and lead to similar results.

The theory can not predict the coefficients weighting the different contributions from the various terms of the potential (1.4). In addition, all the theoretical energy levels can be corrected to take into account relativistic effects. All those contributions need to be compared with experimental data of charmonium spectroscopy to evaluate the relative weight. Table 1.2 shows the comparison between predictions and experimental values for the mass splitting with respect to the J/ψ .

Another possibility to predict the charmonium mass spectrum is to compute it with the lattice QCD, which is essentially QCD applied to a discrete 4 dimensional space. The field theory fundamental principles and the path integral can be used to calculate, on a computer, the properties of the strong interaction. The value of the lattice spacing, usually denoted with a, can be decided depending on the specific problem that has to be solved. Another important parameter is the QCD bare coupling constant g, or $\beta = 6/g^2$ [10]. Typical values are $\beta \approx 6$ and $a \approx 0.1$ fm. The physical quantities can be obtained in the limit $a \to 0$.

To compute the heavy quarkonia spectrum, the NRQCD can be applied to the lattice calculation. The bottomonium spectrum is well reproduced, even if it is not possible to compare the mass value for the η_b state, which is not observed. The charmonium system, on the other side, is more relativistic and not so well described by NRQCD; anyway the observation of the ground state η_c allows the determination of m_c directly from the M_{η_c} measurement [11].

Table 1.3 show some lattice QCD result for the masses of the charmonium states. These results are less precise than the ones obtained with the non relativistic potential model and have a low predictive power for not observed states, but the advantage

R	M_R (MeV)		
	PDG 2002	Chen (2001) [12]	Okamoto *et al.* (2002) [13]
η_c	2979.7	3012(2)	3003(4)
J/ψ	3096.87	3090(1)	3088(1)
χ_0	3415.1	3465(3)	3442(10)
χ_1	3510.51	3519(2)	3517(11)
χ_2	3556.18	-	3549(15)
h_c	3526.14	3517(5)	3519(11)
η_c'	3594	3700(20)	3806(50)
ψ'	3685.96	3750(40)	3849(49)

Table 1.3: Recent results for the charmonium states masses from lattice NRQCD computation. The masses by P. Chen [12] are obtained with $\beta = 5.9$, the M. Okamoto *et al.* result [13] is obtained setting as input of the simulation the scale of $1P - 1S$ splitting and in the $a \to 0$ limit.

of this approach is that all the mass values come directly from the application of NRQCD just setting the scale for the $1P - 1S$ or $2S - 1S$ and it is not needed to fit the whole spectrum.

The higher discrepancies in both potential and lattice models are in the evaluation of the η_c' mass. Recently BELLE has observed a η_c' candidate with mass $M_{\eta_c'} = 3654 \pm 6 \pm 8$ MeV [14]. If confirmed, this could improve the theoretical description of the $\bar{c}c$ mass spectrum phenomenology.

1.2 Charmonium formation in $\bar{p}p$ annihilation

Charmonium has been studied in detail at e^+e^- colliders. With this technique the lepton pair annihilates in a virtual photon with $J^{PC} = 1^{--}$, as shown in Figure 1.4 (a) and so only the J/ψ and ψ' states can be directly formed. All the other states can be studied via radiative decays, at high energy e^+e^- colliders in two virtual photons interactions or in the decays of B mesons.

When charmonium is formed in $\bar{p}p$ annihilations, as shown in Figure 1.4 (b), the angular momentum and spin of the initial $\bar{p}p$ state is not defined and so, through the annihilation in the appropriate number of gluons, all the J^{PC} charmonium states are directly accessible.

In this thesis charmonium states are selected through the decay modes $J/\psi \to e^+e^-$ and $\psi' \to e^+e^-$, for this reason we will now give a brief look to the expected ψ' polarization and the subsequent e^+e^- angular distribution. In what follows the polar angle is measured with respect to the z axis, defined as the antiproton direction in the center of mass system.

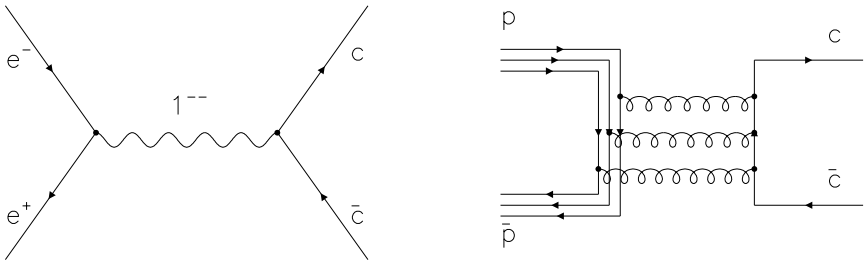

(a) (b)

Figure 1.4: Charmonium formation in e^+e^- (a) and $\bar{p}p$ (b) annihilation.

In the processes $\overline{p}p \to J/\psi \to e^+e^-$ and $\overline{p}p \to \psi' \to e^+e^-$, since the total angular momentum J is conserved, the angular distribution of the $e^{\pm}$ depends on the helicity of the initial state.

Let's consider the variables as shown in Figure 1.5. In the limit of negligible mass electron, $\lambda_{e^-} = -1/2$ and $\lambda_{e^+} = +1/2$. The polar angle of the leptons for the processes $\overline{p}p \to J/\psi \to e^+e^-$ and $\overline{p}p \to \psi' \to e^+e^-$ in the center of mass frame are distributed like:

$$\frac{dN}{d\cos\theta_e} \propto 1 + \lambda\cos^2\theta_e \tag{1.5}$$

where the coefficient λ is given by:

$$\lambda = \frac{E_{CM}^2 - 4\left|\frac{G_E}{G_M}\right|^2 m_p^2}{E_{CM}^2 + 4\left|\frac{G_E}{G_M}\right|^2 m_p^2}. \tag{1.6}$$

In (1.6) E_{CM} is the center of mass energy; the G_E and G_M form factors are related to the Pauli form factors by the expressions [15]:

$$\begin{aligned} G_E(q^2) &= F_1(q^2) + \frac{q^2}{4m_p^2}F_2(q^2), \\ G_M(q^2) &= F_1(q^2) + F_2(q^2). \end{aligned}$$

For charmonium states produced in e^+e^- annihilation $\lambda = 1$, because of the helicity of the initial state. If the protons were pointlike particles, the Pauli form

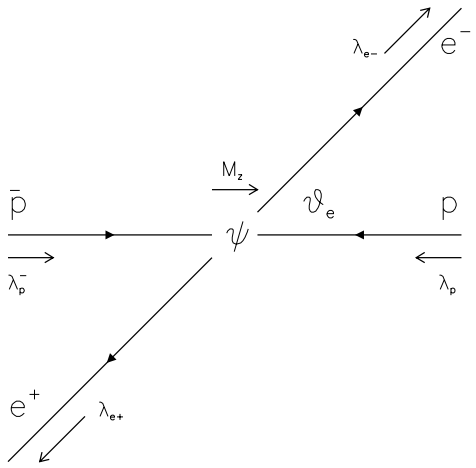

Figure 1.5: Conventions for variables used in helicity formalism.

factor F_2 would be 0. In this case $\lambda_{J/\psi} = 0.46$ and $\lambda_{\psi'} = 0.59$. Deviations from these values are indications of the proton structure. In the limit of high E_{CM} annihilations (if the proton mass can be neglected) $\lambda \simeq 1$. The only available measurement for the ψ' was obtained at FNAL by E760: $\lambda_{\psi'} = 0.69 \pm 0.26$ [16].

For the decay $\psi' \to J/\psi\pi\pi$, the dipion and the J/ψ are emitted mainly in S wave in the ψ' system and also the two pions in the $(\pi\pi)$ CM system are mainly in $L = 0$ state, therefore the J/ψ has the same polarization than the ψ' . This means that also the angular distribution of e^+e^- from the J/ψ decay will be $1 + \lambda_{\psi'} \cos^2\theta_e$.

For the $J/\psi\eta$ decay channel the situation is complicated by the fact that the η has odd parity. The e^+e^- angular distribution for this channel is proportional to $(5\lambda_{\psi'} + 4) - 4\lambda_{\psi'} \cos^2\theta_e$ [17].

1.3 Charmonium decay

Since the discovery of the J/ψ , a really surprising feature of such a massive resonance was its narrowness. The measurement of the width (,) of a resonance is very important because it gives information about the lifetime of the particle, which is related to the kind of interaction causing the decay and to the number of accessible channels.

Also the partial widths , $_{ab}$, related to the specific decay channel of the resonance $R \to a + b$ (or the branching ratios $\mathcal{B}_{ab} =$, $_{ab}/$,) play an important role in the understanding of the physics mechanism of the particle decay.

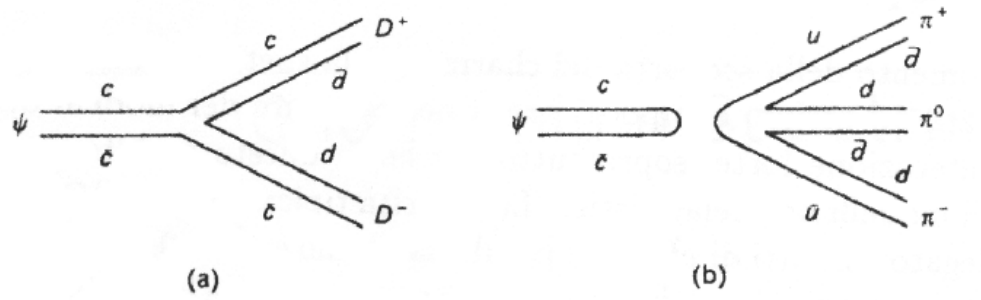

Figure 1.6: OZI (Okubo - Zweig - Iizuka) rule: the favorite decay modes are the ones with the quark lines from initial to final states connected, as shown in (a); the decay channels with quark lines not connected, as the one shown in (b), are suppressed.

The J/ψ has a very large mass and small decay width, if compared with the light quark (u, d, s) mesons. In fact the small width can be explained observing that its decay can occur only violating the OZI rule (see Figure 1.6). While the $\bar{c}c$ states above the open charm threshold can quickly decay into $\overline{D}D$ pairs, which is OZI favorite, the situation for the states with mass below 3740 MeV is different. In QCD, the rule can be explained observing that the favorite decay modes can be the result of a single gluon interaction while the suppressed decays must proceed through the annihilation of the $\bar{c}c$ pair in 2 or more gluons.

The dominant decay modes of charmonium are hadronic and electromagnetic ones. The widths for the electromagnetic processes, such as radiative transitions or lepton pair decay, can be calculated with good approximation within QED. When hadrons are present in the final state the process should be described using QCD but, because of its non perturbative nature, all the calculations of strong processes have always a high theoretical uncertainty.

1.3.1 Electromagnetic decay

Electromagnetic processes are calculable with high accuracy within the QED. At the leading order (LO) in α (fine structure constant) the annihilation of a $\bar{c}c$ pair can occur into a lepton pair via a virtual photon for the 1^{--} states or in $\gamma\gamma$ for the states with $C = +1$, as shown in Figure 1.7. The annihilation into three photons (for the $C = -1$ states) is at the next-to-leading order (NLO) and it is not observed in experiments. In the following we will look in more detail all the tipology and give some numerical expressions for the electromagnetic decay widths for $\bar{c}c$ states. The strong corrections, calculated at the LO in α_s, are due to gluon exchange between the quark and the antiquark in the initial state.

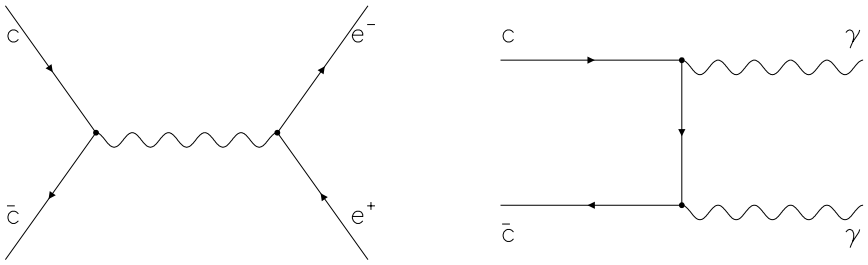

(a) (b)

Figure 1.7: Charmonium e.m. decay at the LO in α. (a) e^+e^- (or $\mu^+\mu^-$, $\tau^+\tau^-$ and $\bar{q}q$) final state, allowed for J/ψ or ψ' decay and (b) $\gamma\gamma$ final state, for η_c, χ_{c0} and χ_{c2}.

1. Exclusive decay into a couple of leptons ($e^{\pm}, \mu^{\pm}$) or light quarks (u, d, s) via a virtual photon. The diagram relative to this process is shown in Figure 1.7 (a). This decay mode is possible only for 1^{--} charmonium states, i.e. the J/ψ and the ψ' . The decay width can be calculated using the Van Royen-Weisskopf formula [18]. For the J/ψ (at the LO in α_s):

$$, (J/\psi \to e^+e^-) = 16\pi\alpha^2 e_c^2 \frac{|\Psi(0)|^2}{4m_c^2} (1 - 16\alpha_s/3\pi),$$

   where $|\Psi(0)|$ is the module of the $\bar{c}c$ wave function in the origin, m_c is the charm quark mass and $e_c = +2/3|e|$ the charm quark electric charge. The same formula can be applied to ψ' decay, in this way one can obtain:

$$\frac{|\Psi_{J/\psi}(0)|^2}{|\Psi_{\psi'}(0)|^2} = \frac{, (J/\psi \to e^+e^-)}{, (\psi' \to e^+e^-)} \simeq 2.4. \tag{1.7}$$

2. Two photon decay, as shown in Figure 1.7 (b). This decay is forbidden for $J = 1$ states, such as the χ_1, because of Yang's theorem[1]. For C conservation, $L = 0$ states should be in spin singlet and $L = 1$ states in spin triplet.

   The partial decay widths to $\gamma\gamma$ can be calculated within QED as it is done for the positronium decay $e^+e^- \to \gamma\gamma$, using $\frac{4}{9}\alpha$ instead of α because of the

[1] Yang's theorem states that $J = 1$ particles can not decay into two massless 1^{--} particles such as photons or gluons.

charm quark charge, and substituting m_e with m_c [19]:

$$, (\eta_c \to \gamma\gamma) = 12\pi\alpha^2 e_c^4 \frac{|\Psi(0)|^2}{m_c^2} (1 - 3.4\alpha_s/\pi), \quad (1.8)$$

$$, (\chi_{c0} \to \gamma\gamma) = 27\alpha^2 e_c^4 \frac{|R'(0)|^2}{m_c^4} (1 + 0.2\alpha_s/\pi), \quad (1.9)$$

$$, (\chi_{c2} \to \gamma\gamma) = \frac{36}{5}\alpha^2 e_c^4 \frac{|R'(0)|^2}{m_c^4} (1 - 16\alpha_s/3\pi), \quad (1.10)$$

where $R'(0)$ is the derivative of the non relativistic P wave function at the origin (see Equation (1.3)).

3. Three photon decay. The photon (and the gluon) has $J^{PC} = 1^{--}$. This imply that, for C conservation, the annihilation in n photons can occur only for states with $C = (-1)^n$. This decay channel is not observable experimentally for any $\bar{c}c$ state because of the small branching ratio, however it is possible to calculate its partial width. We will give now the theoretical expression for the decay width for the case of the J/ψ or ψ' , having in mind to extend it later to the three gluon decay, which is one of the main decay modes for $C = -1$ states:

$$, ({}^3S_1 \to \gamma\gamma\gamma) = \frac{16}{3}(\pi^2 - 9)\alpha^3 e_c^6 \frac{|\Psi(0)|^2}{m_c^2} (1 - 12.6\alpha_s/\pi). \quad (1.11)$$

1.3.2 Radiative transitions

The radiative transitions, as in atoms, occur from an excited to a lower mass $\bar{c}c$ state with the emission of a photon; they can be subdivided in electric dipole transitions (E1), obeying to the selection rules $\Delta L = \pm 1$, $\Delta S = 0$, and magnetic dipole transitions (M1), with the selection rules $\Delta L = 0$, $\Delta S = \pm 1$.

All the widths of the radiative transitions between $\bar{c}c$ states below the open charm threshold are measured, with the only exception of the decay $h_c \to \eta_c\gamma$ (see Table 1.4).

The electric dipole decay widths depend on the mass (M) and the spatial part of the $\bar{c}c$ wave function of the initial and final states. The transitions widths between S and P waves are calculable using the expressions (where subscripts i and f indicate the initial and final states):

$$, (S \to P + \gamma) = \frac{2J_f + 1}{2J_i + 1} \cdot \frac{4}{9} e_Q^2 \alpha k^3 |E_{if}|^2, \quad (1.12)$$

$$, (P \to S + \gamma) = \frac{4}{9} e_Q^2 \alpha k^3 |E_{if}|^2, \quad (1.13)$$

$i \to f$	kind	$M_i - M_f$ (MeV)	$\Gamma_{i\to f}$ (keV)
$\psi' \to \chi_2$	E1	129.78 ± 0.16	26 ± 3
$\psi' \to \chi_1$	E1	175.45 ± 0.16	25 ± 3
$\psi' \to \chi_0$	E1	270.9 ± 0.8	20 ± 2
$\chi_2 \to J/\psi$	E1	459.31 ± 0.14	170 ± 40
$\chi_1 \to J/\psi$	E1	413.64 ± 0.13	290 ± 50
$\chi_0 \to J/\psi$	E1	318.2 ± 0.8	390 ± 60
$h_c \to \eta_c$	E1	546.4 ± 1.5	-
$J/\psi \to \eta_c$	M1	117.2 ± 1.5	1.1 ± 0.4
$\psi' \to \eta_c$	M1	706.3 ± 1.5	0.84 ± 0.19

Table 1.4: Partial widths for charmonium radiative transitions [3].

Transition	Γ_{exp} (MeV)	Γ_{theo} (MeV)
$\chi_{c0} \to J/\psi\gamma$	0.17 ± 0.04	0.131
$\chi_{c1} \to J/\psi\gamma$	0.29 ± 0.05	0.299
$\chi_{c2} \to J/\psi\gamma$	0.39 ± 0.06	0.418
$h_c \to \eta_c\gamma$	-	0.59

Table 1.5: World averages of the partial widths for the radiative decay of χ_J mesons [3]. A fit of the three values with (1.13) gives $|E_{if}| = (1.8 \pm 0.1) \times 10^{-3}$ (with a $\chi^2/ndf = 1.1/2$), which has been used to calculate the expected theoretical values Γ_{theo}.

where $k = (M_i^2 - M_f^2)/(2M_i)$ is the photon momentum, $|E_{if}|$ the transition dipole matrix element:

$$|E_{if}| = \int_0^\infty dr r^3 \cdot R_i(r) R_f(r), \tag{1.14}$$

and $R(r)$ is the radial part of the charmonium wave functions.

Using (1.13) and experimental data for $\chi_J \to J/\psi\gamma$, it is possible to fit $|E_{if}|$, and obtain a prediction for Γ, $(h_c \to \eta_c\gamma)$. Using world averages (see Table 1.5) we obtained $|E_{if}| = (1.8 \pm 0.1) \times 10^{-3}$, that corresponds to Γ, $(h_c \to \eta_c\gamma) = 0.59 \pm 0.07$ MeV (where the error comes directly from the error on $|E_{if}|$)

The only magnetic dipole transitions between charmonium states experimentally observed are:

$$J/\psi, \psi' \to \eta_c\gamma,$$

and the decay width can be calculated to be:

$$\Gamma, ({}^3S_1 \to {}^3S_0 + \gamma) = \frac{4}{3} e_Q^2 \alpha \left(\frac{k}{m_c}\right) \frac{k}{1 + k/\sqrt{M({}^3S_0)^2 + k^2}} |I_{if}|^2 \tag{1.15}$$

where:

$$|I_{if}| = \int \Psi_f^*(\vec{x}) \cos(\vec{k} \cdot \vec{x}/2) \Psi_i(\vec{x}) d^3x. \tag{1.16}$$

1.3.3 Strong decay

The strong decay can be treated by applying the same conservation laws used for the electromagnetic decays. The differences, from a qualitative point of view, are:

- gluons have color charge: they are SU(3) color octet states. Since all observable particles, such as charmonium states, are color singlets, the annihilation of the $\bar{c}c$ pair is forced by the color conservation to proceed through at least 2 gluons;
- gluons and quarks do not exist as free states in nature: they can only exist in color singlet combinations. This is why gluonic decay is always followed by hadronization of the final state;
- given the high value of α_s, especially for low momentum transfer, QCD can not be always treated as a perturbative theory.

Two main kind of strong decay processes can occur. The first, related to the complete annihilation of the heavy $\bar{Q}Q$ (through the emission of high momentum gluons) as shown in Figure 1.8 (a), can be treated in a perturbative way. The second is the hadronic deexcitation of charmonium, accompanied by the emission of 2 or more soft gluons and followed by their hadronization, as shown in Figure 1.8 (b). This is for example the case of the $\psi' \to J/\psi\pi\pi$ and $\psi' \to J/\psi\eta$ decays. The low momentum carried by the gluons do not allow a perturbative treatment of the subject. Nevertheless, some of the features of these decays, such as the dipion invariant mass distribution, the π angular distributions in $\psi' \to J/\psi\pi\pi$ and the relative branching ratio of $\psi' \to J/\psi\eta$ with respect to $\psi' \to J/\psi\pi\pi$ can be calculated within theoretical models and can provide information on the strong interaction at low momentum transfer. Since the latter decay modes of the ψ' are the subject of this work, more details will be given in Chapter 2. In the following part of this section we will describe the strong perturbative theory of charmonium decay.

The PQCD theoretical calculation for charmonium annihilation are similar to QED calculation where the photon are replaced by gluons (and so α becomes α_s), then the hadronization of the final state is supposed to happen with probability 1. Under these assumptions, the decay of the $\bar{c}c$ pair into light hadrons can be considered as the annihilation into gluons (as shown in the diagram of Figure 1.8 (a)).

In particular, for the two gluons decay width we have:

$$\frac{\Gamma_{gg}}{\Gamma_{\gamma\gamma}} = \frac{2}{9} \frac{\alpha_s^2}{\alpha^2 e_c^4}, \tag{1.17}$$

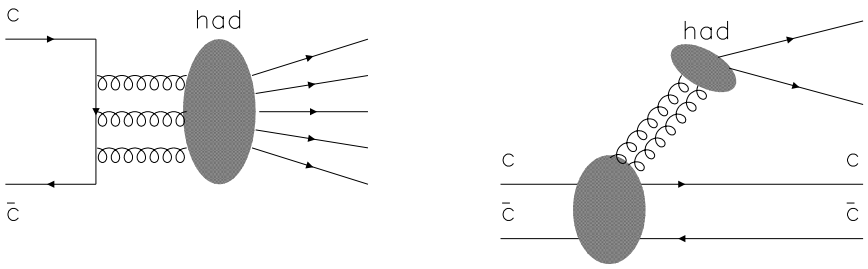

(a) (b)

Figure 1.8: Charmonium strong decay into light hadrons (a) and strong radiative decay (b).

and for the three gluons:

$$\frac{\Gamma_{ggg}}{\Gamma_{\gamma\gamma\gamma}} = \frac{5}{54}\frac{\alpha_s^3}{\alpha^3 e_c^6}, \tag{1.18}$$

where the factors 2/9 in (1.17) and 5/54 in (1.18) come from color algebra.

Using (1.17) and (1.18) together with (1.8-1.11) it is easy to calculate the partial widths at the leading order in α_s for the decays:

$$\Gamma_0(\eta_c \to gg) = \frac{8}{3}\pi\alpha_s^2\frac{|\Psi(0)|^2}{m_c^2}, \tag{1.19}$$

$$\Gamma_0(\chi_{c0} \to gg) = 6\alpha_s^2\frac{|R'(0)|^2}{m_c^4}, \tag{1.20}$$

$$\Gamma_0(\chi_{c2} \to gg) = \frac{8}{5}\alpha_s^2\frac{|R'(0)|^2}{m_c^4}, \tag{1.21}$$

and for the $^3S_1$ states, for which the LO is α_s^3:

$$\Gamma_0(^3S_1 \to ggg) = \frac{40}{81}(\pi^2 - 9)\alpha_s^3\frac{|\Psi(0)|^2}{m_c^2}, \tag{1.22}$$

where the gg and ggg final states in the previous formulas are ment to be inclusive light hadrons (LH) final states. The fact that the J/ψ annihilation must proceed through 3 gluons gives a rough explanation of the narrowness of its width with

respect to the η_c. From (1.22) we can roughly estimate by using (1.7) that[2] , $(\psi' \to LH) \simeq$, $(J/\psi \to LH)/2.4 \simeq 77$ keV. For the η_c, the $\bar{c}c$ ground state, the (1.19) is the main decay mode. The triplet P wave states $\chi_{0,1,2}$ (1^3P_J) decay mainly via hadronic decay or radiative decay to J/ψ .

In the strong interaction case the first loop corrections can be of the same order of magnitude of the leading order (LO); the decay widths can be written as:

$$, (\overline{c}c \to f) = , _0 \left(1 + \frac{B\alpha_s}{\pi}\right), \tag{1.23}$$

the B coefficients have been evaluated in reference [19]:

$$\begin{aligned} B_{\eta_c} &= 4.8 \\ B_{J/\psi} &= -3.7 \\ B_{\chi_{c0}} &= 9.5 \\ B_{\chi_{c2}} &= -2.2 \end{aligned}$$

Bodwin, Braaten and Lepage [20] proposed a rigorous way for handling the inclusive annihilation of heavy quarks, by using the NRQCD, that can be used to calculate the decay widths of quarkonia states to light hadrons.

In the non relativistic case, the quark velocity v is small ($v^2 \approx 0.3$ for charmonium and $v^2 \approx 0.1$ for bottomonium). So it is is possible to identify different momentum scales that play different roles in the quarkonium dynamics: a short distance scale ($\sim 1/m_Q$, where m_Q is the heavy quark mass), describing the $\bar{Q}Q$ annihilation, that can be treated in a perturbative way, and a long distance scale ($\sim 1/m_Q v$), which is the quarkonium size scale and so it is suitable for the description of the $\bar{Q}Q$ interaction in the bound state, such as the soft gluon emission.

This approach allows the decoupling of the "hard" (short distance) processes, that can be treated in a perturbative way, from the "soft" (long distance) gluon emission, that can not be treated perturbatively because of the high α_s value, with a complete factorization of the two scales.

In the theory, the quarkonium state $|H\rangle$ is considered as the sum of several Fock states. The dominant Fock state is composed by the heavy antiquark - quark pair in a color singlet state and in angular momentum state $^{2S+1}L_J$; another Fock state that contributes to the charmonium decay amplitude at the leading perturbative

[2] This is usually called the "12% rule". For any hadronic final state h it is reasonably well satisfied that:

$$\frac{\mathcal{B}(\psi' \to h)}{\mathcal{B}(J/\psi \to h)} = \frac{, (\psi' \to h)}{, _{\psi'}} \cdot \frac{, _{J/\psi}}{, (J/\psi \to h)} = \frac{1}{2.4} \cdot \frac{, _{J/\psi}}{, _{\psi'}} \simeq 12\%.$$

order is the state in which the $\bar{Q}Q$ emit a soft gluon remaining in a color octet state:

$$|H\rangle = c_0|^{2S+1}L_J^{[1]}\rangle + \sum c_1|^{2S'+1}L_{J'}^{\prime[8]}g\rangle + ...$$

The color octet states can annihilate at the LO into one gluon, so their contribution to the total width of $\bar{c}c$ states is of the same order of the color singlet ones.

Bodwin, Braaten and Lepage have shown that quarkonium decay rate can be written as a sum of terms, each of them being the product of a long distance matrix element with a short distance coefficient (f and g) that can be calculated perturbatively within QCD. The long distance matrix elements have to be fitted from the experimental values of the charmonium states widths. The correct way to calcualte hadronic widths for S and P wave states in NRQCD is:

$$\begin{aligned}
, \left(^{2S+1}S_J \to LH\right) &= \frac{2\mathrm{Im}f_1\left(^{2S+1}S_J\right)}{m_c^2}\left\langle ^{2S+1}S_J|\mathcal{O}_1\left(^{2S+1}S_J\right)|^{2S+1}S_J\right\rangle \\
&+ \frac{2\mathrm{Im}g_1\left(^{2S+1}S_J\right)}{m_c^4}\left\langle ^{2S+1}S_J|\mathcal{P}_1\left(^{2S+1}S_J\right)|^{2S+1}S_J\right\rangle \\
&+ O(v^3,), \qquad (1.24) \\
, \left(^{2S+1}P_J \to LH\right) &= \frac{2\mathrm{Im}f_1\left(^{2S+1}P_J\right)}{m_c^4}\left\langle ^{2S+1}P_J|\mathcal{O}_1\left(^{2S+1}P_J\right)|^{2S+1}P_J\right\rangle \\
&+ \frac{2\mathrm{Im}f_8\left(^{2S+1}S_J\right)}{m_c^2}\left\langle ^{2S+1}P_J|\mathcal{O}_1\left(^{2S+1}S_J\right)|^{2S+1}P_J\right\rangle \\
&+ O(v^2,), \qquad (1.25)
\end{aligned}$$

where the index 1 and 8 correspond to singlet and octet charmonium state annihilation. While (1.24) is at the NLO in v, the two terms of (1.25) are of the same order, so the color octet contribution become very important in the calculation of the hadronic decay width of charmonium P waves. Color octet contributions to P wave states decay amplitudes have been calculated and can be found in [21] and [22].

It is also possible to determine the matrix element values from lattice calculation [23], but the uncertainty is large and do not allow a real comparison with experimental values.

1.4 Isospin breaking scale in ψ' strong decay

Isospin (I) has been introduced to describe groups of particles which have nearly the same mass but different electric charge. The name is due to the fact that isospin, as a mathematical object, has the same properties of the spin.

It was introduced to describe the proton and the neutron: these two particles can be considered as a single particle (the nucleon) with $I = 1/2$ and isospin projection $I_3 = +1/2$ for the proton and $I_3 = -1/2$ for the neutron.

Also the three pions are grouped in a $I = 1$ triplet assigning $I_3 = +1$ to π^+, $I_3 = 0$ to π^0 and $I_3 = -1$ to π^-.

Isospin has been naturally extended at the quark level: the up and down quark form an isospin doublet ($I = 1/2$) with projections $I_3 = +1/2$ and $-1/2$ respectively. In this way, for each light hadron it is possible to calculate:

$$\frac{q}{e} = I_3 + \frac{S+B}{2} \tag{1.26}$$

where S is the strangeness and B the baryon number.

Isospin is expected to be conserved in the strong but not in the electromagnetic and weak interactions. This is due to the fact that the strong interaction is independent on the electric charge, and that the u and d quarks have nearly the same mass.

Deviation to the exact isospin conservation should arise as a consequence of the mass difference between up and down quarks at the scale:

$$\sim \frac{m_d - m_u}{\Lambda_{QCD}} \simeq 2 \times 10^{-2}, \tag{1.27}$$

where $m_u \simeq 5$ MeV, $m_d \simeq 9$ MeV, $\Lambda_{QCD} \simeq 0.2$ GeV, and from the coexistence of the strong and the electromagnetic interaction in many processes, with an effect of the order of few percent[3]. Anyway it was soon realized that the QCD hamiltonian could also contain isospin breaking terms, and so isospin violation could arise as a straightforward consequence of the strong interaction [24].

The largest isospin violations in strong interaction processes are observed in πN elastic scattering. The analysis of the $\pi N \to \pi N$ data at low energy show a possible isospin violation of the order of about 7% [25] [26].

The presence of an isospin violating contribution in the strong interaction is particularly interesting from a theoretical point of view: it has been recently demonstrated that such a contribution will affect the Standard Model prediction for the CP violation parameter ϵ'/ϵ in a significant way, introducing also a relevant theoretical uncertainty [27].

1.4.1 Isospin violation in ψ' decay

The charmonium decay channels are a good testing ground for isospin conservation in the strong interaction. Some of the decay processes are unambiguosly due to the strong interaction and their branching ratios are known with the necessary precision of a few percent. Moreover, the isospin of the initial $\bar{c}c$ state is $I = 0$ so, in the decay $\psi' \to J/\psi X$, the isospin conservation can be checked by looking at the isospin of the X system.

[3] The scale of e.m. to strong interaction can be obtained from α_{em}/α_s at the typical meson dimension scale ($0.2 \div 0.3$ fm) and is $\approx 2\%$.

The pion can be considered as an element of an isospin 1 multiplet, namely:

$$|I, I_3\rangle = \begin{cases} |1, \pm 1\rangle \equiv |\pi^{\pm}\rangle \\ |1, 0\rangle \equiv |\pi^0\rangle \end{cases} .$$

The decay channel:

$$\begin{aligned} \psi' &\rightarrow J/\psi + \pi^0 \\ |I, I_3\rangle = |0, 0\rangle &\rightarrow |0, 0\rangle + |1, 0\rangle \end{aligned} \tag{1.28}$$

is obviously isospin violating. Roughly, the scale of isospin violation can be obtained in this case by comparing the $J/\psi\pi^0$ with the $J/\psi\eta$ branching ratio and it is of the order of , $(J/\psi\pi^0)/$, $(J/\psi\eta) \simeq 3 \times 10^{-2}$, which is the scale of electromagnetic to strong interaction at the typical distance of the meson dimension.

If we consider a dipion system, the total wave function is given by:

$$\Psi(total) = \psi(space) \cdot \chi(isospin). \tag{1.29}$$

The isospin of the dipion can be expressed in terms of the isospin of the two pions by using the Clebsch-Gordan coefficients. For a neutral ($I_3 = 0$) dipion it is possible to have three different isospin states:

$$|0, 0\rangle = \sqrt{\frac{1}{3}}|\pi^+\pi^-\rangle - \sqrt{\frac{1}{3}}|\pi^0\pi^0\rangle + \sqrt{\frac{1}{3}}|\pi^-\pi^+\rangle, \tag{1.30}$$

$$|1, 0\rangle = \sqrt{\frac{1}{2}}|\pi^+\pi^-\rangle - \sqrt{\frac{1}{2}}|\pi^-\pi^+\rangle, \tag{1.31}$$

$$|2, 0\rangle = \sqrt{\frac{1}{6}}|\pi^+\pi^-\rangle + \sqrt{\frac{2}{3}}|\pi^0\pi^0\rangle + \sqrt{\frac{1}{6}}|\pi^-\pi^+\rangle, \tag{1.32}$$

Bose statistics requires that $\Psi(total)$ is symmetric under the particle exchange. If isospin is a perfect symmetry, an even L wave ($\pi\pi$) system must have a symmetric spin wave function, so only $I = 0$ and 2 are allowed.

In ψ' decay two channels are observed:

$$\psi' \rightarrow J/\psi + \pi^0\pi^0 \tag{1.33}$$

$$\psi' \rightarrow J/\psi + \pi^+\pi^- \tag{1.34}$$

$$|I, I_3\rangle = |0, 0\rangle \rightarrow |0, 0\rangle + |I, 0\rangle$$

where, for the isospin conservation, the dipion in the final state should be in the state $|I, I_3\rangle = |0, 0\rangle$. Looking at (1.30), in the case of isospin conservation it is expected that , $(J/\psi\pi^0\pi^0)/$, $(J/\psi\pi^+\pi^-) \simeq 0.5$.

The PDG fit value is [3]:

$$\frac{, (J/\psi\pi^0\pi^0)}{, (J/\psi\pi^+\pi^-)} = 0.60 \pm 0.06, \tag{1.35}$$

which is compatible with isospin conservation within 2σ but suggests the possibility of isospin violation.

The scale of isospin violation in this process can be easily obtained looking at the amount of $I = 2$ in the dipion system. The isospin transition matrix $\mathcal{T}_I$ for the process $\psi' \to J/\psi\pi\pi$ can be expressed as the sum of isospin conserving ($\mathcal{T}_0$) and isospin breaking ($\mathcal{T}_2$) contributions. The dipion due to the decay of the initial $|0,0\rangle$ state will be in an isospin state:

$$|\pi\pi\rangle = \mathcal{T}_I|0,0\rangle = \mathcal{T}_0|0,0\rangle + \mathcal{T}_2|0,0\rangle, \tag{1.36}$$

or, introducing the amplitudes:

$$c_0 = \langle 0,0|\mathcal{T}_I|0,0\rangle = \langle 0,0|\mathcal{T}_0|0,0\rangle, \tag{1.37}$$

$$c_2 = \langle 2,0|\mathcal{T}_I|0,0\rangle = \langle 2,0|\mathcal{T}_2|0,0\rangle, \tag{1.38}$$

the isospin of the dipion in the final state can be expressed as:

$$|\pi\pi\rangle = c_0|0,0\rangle + c_2|2,0\rangle, \tag{1.39}$$

where the coefficient are chosen to be real and the normalization is $c_0^2 + c_2^2 = 1$. The scale of isospin violation for the interaction is given by the coefficient $|c_2|$. Using (1.30) and (1.32) in (1.39) the final state dipion can be expressed as:

$$|\pi\pi\rangle = \left(\frac{c_0}{\sqrt{3}} + \frac{c_2}{\sqrt{6}}\right)|\pi^+\pi^-\rangle + \left(-\frac{c_0}{\sqrt{3}} + \frac{2c_2}{\sqrt{6}}\right)|\pi^0\pi^0\rangle + \left(\frac{c_0}{\sqrt{3}} + \frac{c_2}{\sqrt{6}}\right)|\pi^-\pi^+\rangle, \tag{1.40}$$

and the probabilities of observing a $\pi^+\pi^-$ or a $\pi^0\pi^0$ are:

$$|\langle\pi^+\pi^-|\pi\pi\rangle|^2 = |\langle\pi^-\pi^+|\pi\pi\rangle|^2 = \frac{c_0^2}{3} + \frac{c_2^2}{6} + \frac{\sqrt{2}}{3}c_0c_2, \tag{1.41}$$

$$|\langle\pi^0\pi^0|\pi\pi\rangle|^2 = \frac{c_0^2}{3} + \frac{2}{3}c_2^2 - \frac{2\sqrt{2}}{3}c_0c_2. \tag{1.42}$$

The observable quantity is:

$$\frac{,\,(J/\psi\pi^0\pi^0)}{,\,(J/\psi\pi^+\pi^-)} = \frac{|\langle\pi^0\pi^0|\pi\pi\rangle|^2}{|\langle\pi^+\pi^-|\pi\pi\rangle|^2 + |\langle\pi^-\pi^+|\pi\pi\rangle|^2} = \frac{c_0^2 + 2c_2^2 - 2\sqrt{2}c_0c_2}{2c_0^2 + c_2^2 + 2\sqrt{2}c_0c_2}; \tag{1.43}$$

the solution of (1.43), with the value from (1.35), gives $|c_2| = (4.4 \pm 2.5) \cdot 10^{-2}$, which is the scale of isospin violation in $\psi' \to J/\psi\pi\pi$ decay, and is compatible with the electromagnetic and quark mass difference effects.

As we will see in Chapter 2, recently only E760 was able to measure the $\mathcal{B}(J/\psi\pi^+\pi^-)$ and $\mathcal{B}(J/\psi\pi^0\pi^0)$ with the capability to check for the isospin violation given by (1.35). The experimental value seems to suggest an isospin violation larger than the one obtained from the PDG fit. This is why it is important to perform a precision measurement of the two branching ratios.

Chapter 2

Phenomenology of $\psi' \to e^+e^-$ and $\psi' \to J/\psi X \to e^+e^- X$

The ψ' , 2^3S_1 excited state, has a mass $M_{\psi'} = 3685.96 \pm 0.09$ MeV and a width , $_{\psi'} = 0.300 \pm 0.025$ MeV [3]. It is one of the most investigated charmonium states because it can be produced directly in e^+e^- annihilation ($J^{PC} = 1^{--}$) and so its observation and study dates back to the first period of charmonium spectroscopy [28]. From 1974, a large amount of data on ψ' decay modes have been collected, but more precise measurements are still needed for the comparison with the theoretical predictions.

The largest contribution to the total decay width of the ψ' is given by the hadronic deexcitation channels, where the transition to a J/ψ state for the $\bar{c}c$ is accompanied by the emission of light hadrons, with an overall branching ratio $\mathcal{B}(\psi' \to J/\psi X) \simeq 56\%$. These decay modes are the subject of this thesis. The other two main decay modes are the radiative decays $\psi' \to \chi_{cJ}\gamma$, with total BR $\sim 24\%$, and the annihilation of the $\bar{c}c$ into light hadrons (LH) with $\mathcal{B}(\psi' \to LH) \sim 25\%$ (as obtained theoretically in Section 1.3.3). These two processes are calculable in a perturbative way, within QED and QCD respectively, as was discussed in Chapter 1. To complete the picture of the ψ' decay modes, both the leptonic decay to e^+e^- and $\mu^+\mu^-$ occur with a BR of $\sim 0.7\%$; $\mathcal{B}(\psi' \to e^+e^-)$ is another subject of this thesis. Table 2.1 summarizes some ψ' branching ratios.

As we will see in more detail in Chapter 3, final states with a high invariant mass e^+e^- pair due to ψ' or J/ψ decay can be selected by the E835 detector. It has the capability to reconstruct the exclusive final states by observing in the electromagnetic calorimeter system the additional photons due to π^0 or η decay or using the inner tracking system to detect the charged particles. This chapter presents the current experimental situation for all the channels analized in this thesis.

chan	$\mathcal{B}(\psi' \to chan)$ (%)
hadrons	98.10 ± 0.30
$J/\psi + anything$	55.7 ± 2.6
$J/\psi + neutrals$	23.9 ± 1.2
$J/\psi\pi^+\pi^-$	30.5 ± 1.6
$J/\psi\pi^0\pi^0$	18.2 ± 1.2
$J/\psi\eta$	3.13 ± 0.21
$J/\psi\pi^0$	0.096 ± 0.021
e^+e^-	0.73 ± 0.04
$\mu^+\mu^-$	0.70 ± 0.09
$\tau^+\tau^-$	0.27 ± 0.07
$\chi_0\gamma$	8.7 ± 0.8
$\chi_1\gamma$	8.4 ± 0.7
$\chi_2\gamma$	6.8 ± 0.6

Table 2.1: Branching ratios for ψ' decay modes from the global fit values of the PDG 2002 [3].

2.1 Measurements of $\psi' \to e^+e^-$ branching ratio

The ψ' partial width to e^+e^- is well measured in e^+e^- colliders. The PDG fit gives [3]:

$$, (e^+e^-) = 2.19 \pm 0.15 \text{ keV}. \tag{2.1}$$

This value was measured at the beginning of charmonium spectroscopy at SLAC by V. Lüth *et al.* in 1975, that found , $(e^+e^-) = 2.1 \pm 0.3$ keV [29]. Later, in 1979, the DASP collaboration at DESY obtained , $(e^+e^-) = 2.0 \pm 0.3$ keV [30].

E760 [16] and E835 [31] studying ψ' formed in $\bar{p}p$ annihilation achieved a good precision on the measurement of the ratio:

$$\frac{\mathcal{B}(\psi' \to e^+e^-)}{\mathcal{B}(\psi' \to J/\psi X)\mathcal{B}(J/\psi \to e^+e^-)}.$$

and, using the PDG values for $\mathcal{B}(\psi' \to J/\psi X)$ and $\mathcal{B}(J/\psi \to e^+e^-)$, obtained:

$$\mathcal{B}(\psi' \to e^+e^-) = 0.0083 \pm 0.0009 \quad \text{(E760)}, \tag{2.2}$$
$$\mathcal{B}(\psi' \to e^+e^-) = 0.0074 \pm 0.0007 \quad \text{(E835)}, \tag{2.3}$$

with a precision comparable to the one achieved at e^+e^- colliders.

More recently BABAR measured the branching fractions [32]:

$$\frac{\mathcal{B}(e^+e^-)}{\mathcal{B}(J/\psi\pi^+\pi^-)} = 0.0252 \pm 0.0030, \quad (2.4)$$

$$\frac{\mathcal{B}(\mu^+\mu^-)}{\mathcal{B}(J/\psi\pi^+\pi^-)} = 0.0216 \pm 0.0030, \quad (2.5)$$

obtaining $\mathcal{B}(e^+e^-) = 0.0078 \pm 0.0012$ and $\mathcal{B}(\mu^+\mu^-) = 0.0067 \pm 0.0011$, which are consistent with the earlier measurements.

As expected from QED calculations, $\mathcal{B}(\psi' \to e^+e^-)$ and $\mathcal{B}(\psi' \to \mu^+\mu^-)$ are compatible. Using their value it is possible to give an estimate of the electromagnetic contribution to the hadronic decay width, as was done in [29]:

$$\frac{,(\psi' \to \gamma^* \to had)}{,_{tot}} = \frac{,(\psi' \to l^+l^-)}{,_{tot}} \times R \simeq 2\%, \quad (2.6)$$

where $R = \frac{\sigma(e^+e^- \to had)}{\sigma(e^+e^- \to \mu^+\mu^-)} \simeq 3$ in this energy region.

2.2 ψ' branching ratio measurements for the inclusive J/ψ decay channels

In the early times of charmonium spectroscopy only the J/ψ and the ψ' could be easily produced and observed at e^+e^- machines. Among the various ψ' decay modes, the inclusive decay to J/ψ gave one of the most evident signal because of the high branching ratio and the presence of two high energy leptons from the J/ψ decay.

From the study of 30000 ψ' decays at SPEAR, made by G. S. Abrams *et al.* [33], it was obtained:

$$\frac{,(\psi' \to J/\psi X)}{,_{tot}} = 0.57 \pm 0.08, \quad (2.7)$$

$$\frac{,(\psi' \to J/\psi\pi^+\pi^-)}{,_{tot}} = 0.32 \pm 0.04, \quad (2.8)$$

$$\frac{,(\psi' \to J/\psi + neutrals)}{,(\psi' \to J/\psi X)} = 0.44 \pm 0.03. \quad (2.9)$$

The presence of the J/ψ among the ψ' decays products was revealed in two ways:

- detecting its decay into $\mu^+\mu^-$;
- measuring the value of the missing mass recoiling against each pair of oppositely charged particles and looking for the two pions from the decay $\psi' \to \pi^+\pi^- J/\psi$.

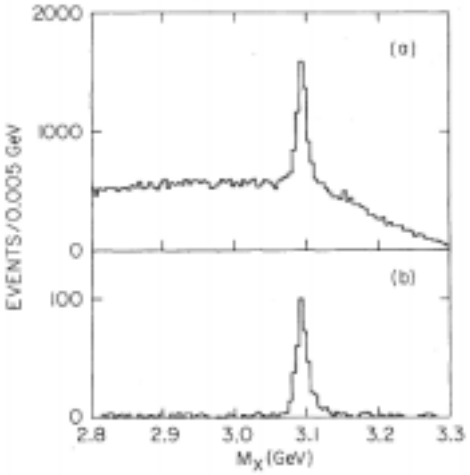

Figure 2.1: (a) distribution of missing mass recoiling against all pair of oppositely charged particles observed at SPEAR by G. S. Abrams *et al.*; when requiring four-prong events conserving the total four-momentum the observed spectrum reduces to the one shown in (b) [33].

Figure 2.1 shows the clean J/ψ signal obtained with the second method.

From (2.7) and (2.8), in reference [33] it was obtained:

$$\frac{, (\psi' \to J/\psi\pi^+\pi^-)}{, (\psi' \to J/\psi X)} = 0.56, \tag{2.10}$$

and using (2.9) it was possible to state that, for isospin conservation, the neutral decays other than $J/\psi\pi^0\pi^0$ should be less than 10% of the total $J/\psi X$.

Revising these data, in 1976 W. Tanenbaum *et al.* [34] observed 48 $\psi' \to J/\psi\eta$ candidates by measuring the invariant mass recoiling against a $J/\psi\pi^\pm$ pair, where the J/ψ was detected via its $\mu^+\mu^-$ decay. The η in this case were supposed to decay to both $\pi^+\pi^-\pi^0$ and $\pi^+\pi^-\gamma$ channels. They measured:

$$\frac{, (\psi' \to J/\psi\eta)}{, \, tot} = 0.043 \pm 0.008 \tag{2.11}$$

and applying this result at (2.7-2.9) it was obtained:

$$\frac{, (\psi' \to J/\psi\pi^0\pi^0)}{, (\psi' \to J/\psi\pi^+\pi^-)} = 0.53 \pm 0.06. \tag{2.12}$$

In 1975 E. Hilger *et al.* measured [35]:

$$\frac{, (\psi' \to J/\psi\pi^0\pi^0)}{, (\psi' \to J/\psi\pi^+\pi^-)} = 0.64 \pm 0.15. \tag{2.13}$$

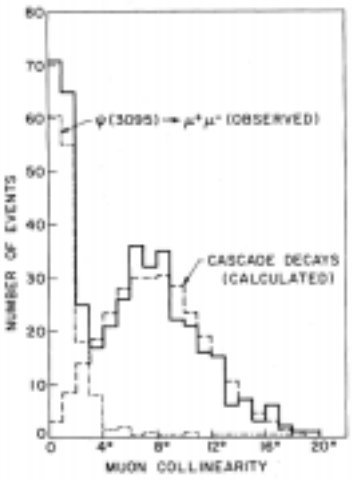

Figure 2.2: $\mu^{\pm}$ collinearity distribution observed at SPEAR by E. Hilger *et al.*. It is based on 444 events [35].

This measurement was made by detecting $J/\psi \to \mu^+\mu^-$ decays in the ψ' energy region and separating exclusive from inclusive decays by looking at the collinearity of the two tracks. Figure 2.2 shows the observed collinearity distribution. They found 126 events in which the $\mu^+\mu^-$ were accompanied by one or two additional charged track (tagged as $J/\psi\pi^+\pi^-$ events) and 69 with one or more γ rays (tagged as $J/\psi\pi^0\pi^0$ events).

Until the end of the 90s, no other measurements on $\psi' \to J/\psi X$ branching ratios were done. In 1996, A. Gribushin *et al.* [36] published the measurement for the ratio:

$$\frac{,(\psi' \to J/\psi\pi^+\pi^-)}{,(\psi' \to \mu^+\mu^-)} = 30.2 \pm 7.1 \pm 6.8, \tag{2.14}$$

obtained by detecting charmonium resonances in π^--Be collisions using a 515 GeV π^- beam. J/ψ and ψ' were detected by their decay to $\mu^+\mu^-$. This number is in very good agreement with the measurements of leptonic decay and $J/\psi\pi^+\pi^-$ branching ratios. Only in 2002 this ratio have been measured with higher precision by BABAR, as was shown in (2.5).

The only experiment that was able to measure simultaneously the BR of all the major J/ψ inclusive decay channels, performing a full reconstruction of the exclusive final states, is Fermilab E760 [16]. The selection was done by identifying the high energy e^+e^- pair coming from $\bar{c}c$ decay, then looking for additional photons due to $J/\psi\pi^0\pi^0 \to e^+e^-4\gamma$ or $J/\psi\eta \to e^+e^-2\gamma$. The only channel selected just applying topological cuts, requiring two charged tracks out of e^+e^- ones but without the capability to obtain a precision measurement for the charged particles directions, was the $J/\psi\pi^+\pi^-$.

E760 collected 3 pb^{-1} of data in the ψ' energy region. With this sample they

observed 2022 $J/\psi X$ candidates; among them 416 were tagged as $J/\psi\pi^+\pi^-$, 157 $J/\psi\pi^0\pi^0$ and 40 $J/\psi\eta$ candidates, obtaining:

$$\frac{\Gamma(\psi' \to J/\psi\pi^+\pi^-)}{\Gamma(\psi' \to J/\psi X)} = 0.496 \pm 0.037, \tag{2.15}$$

$$\frac{\Gamma(\psi' \to J/\psi\pi^0\pi^0)}{\Gamma(\psi' \to J/\psi X)} = 0.323 \pm 0.033, \tag{2.16}$$

$$\frac{\Gamma(\psi' \to J/\psi\eta)}{\Gamma(\psi' \to J/\psi X)} = 0.061 \pm 0.015. \tag{2.17}$$

Although the (2.15) is the only measurement quoted by the PDG, the PDG fit value 0.547 ± 0.011 tends to be slightly larger, for this reason it would be nice to measure it with higher accuracy. From (2.16) and (2.15) it can be easily calculated:

$$\frac{\Gamma(\psi' \to J/\psi\pi^0\pi^0)}{\Gamma(\psi' \to J/\psi\pi^+\pi^-)} = 0.65 \pm 0.10, \tag{2.18}$$

which seems to suggest isospin violation in strong interaction[1].

E835 collected 10 pb^{-1} of data in the ψ' energy region in the first data taking period (1996-97). The measurement of $J/\psi\pi^+\pi^-$ could not be performed in the first data taking period, however the measurements for $J/\psi\pi^0\pi^0$ and $J/\psi\eta$ are compatible with E760 [31]:

$$\frac{\Gamma(\psi' \to J/\psi\pi^0\pi^0)}{\Gamma(\psi' \to J/\psi X)} = 0.328 \pm 0.015, \tag{2.20}$$

$$\frac{\Gamma(\psi' \to J/\psi\eta)}{\Gamma(\psi' \to J/\psi X)} = 0.072 \pm 0.009, \tag{2.21}$$

but the sample was largely increased, containing 11446 $J/\psi X$, 691 $J/\psi\pi^0\pi^0$ and 193 $J/\psi\eta$ candidates. With this method, E760 and E835 are the only experiments that recently obtained a measurement of $\mathcal{B}(\psi' \to J/\psi\pi^0\pi^0)$.

The most precise measurement of the ψ' branching ratio to $J/\psi\pi^+\pi^-$ at present has been obtained by BES, with the analysis of 1149 nb^{-1} of data around the ψ' resonance [38]:

$$\mathcal{B}(\psi' \to J/\psi\pi^+\pi^-) = 0.323 \pm 0.014. \tag{2.22}$$

[1] In a review paper, Y. F. Gu and X. H. Li [37] performed a different analysis on E760 data by applying a global fit to all the measured branching ratios and obtaining:

$$\frac{\Gamma(\psi' \to J/\psi\pi^0\pi^0)}{\Gamma(\psi' \to J/\psi\pi^+\pi^-)} = 0.61 \pm 0.08, \tag{2.19}$$

which is still more than one standard deviation far from the theoretical value 0.5.

Experiment	N_{evts}	$\mathcal{B}(\psi' \to J/\psi\eta)$
E835 [31]	167	$0.041 \pm 0.003 \pm 0.005$
E760 [16]	36	$0.032 \pm 0.010 \pm 0.002$
MRK2 [39]	166	0.025 ± 0.006
CBAL [40]	386	$0.0218 \pm 0.0014 \pm 0.0035$
DASP [41]	17	0.035 ± 0.009
CNTR [42]	164	0.036 ± 0.005
MRK1 [34]	44	0.043 ± 0.008

Table 2.2: $\mathcal{B}(\psi' \to J/\psi\eta)$ obtained from measurement by several experiments. The number of events observed in each experiment is also indicated. E835 and E760 actually measured the ratio , $(\psi' \to J/\psi\eta)/$, $(\psi' \to J/\psi X)$ while MRK2 measured , $(\psi' \to J/\psi\eta)/$, $(\psi' \to J/\psi\pi^+\pi^-)$. All the other results come from , $(\psi' \to J/\psi\eta)/$, $_{tot}$ measurement.

Experiment	N_{evts}	$\mathcal{B}(\psi' \to J/\psi\pi^0)$
MRK2 [39]	7	$(15 \pm 6) \times 10^{-4}$
CBAL [40]	23	$(9 \pm 2 \pm 1) \times 10^{-4}$

Table 2.3: $\mathcal{B}(\psi' \to J/\psi\pi^0)$ obtained from measurement by MARK-II and Crystal Ball. The number of events observed in each experiment is also indicated.

Since all the recent measurement of the ratio , $(\psi' \to J/\psi\pi^0\pi^0)/$, $(\psi' \to J/\psi\pi^+\pi^-)$ are systematically larger than 0.5 it is worthwhile to measure this ratio with high accuracy to check for isospin violation in strong decays. E835 seems to be today the only experiment capable to measure the ψ' partial width to $J/\psi\pi^0\pi^0$, having at the same time the possibility to check the E760 result with a larger statistics and using a kinematic fit selection for $J/\psi\pi^+\pi^-$ events.

$\mathcal{B}(\psi' \to J/\psi\eta)$ have been measured several times with different experimental techniques. The measurements from various experiments are summarized in Table 2.2.

For the reaction $\psi' \to J/\psi\pi^0$ the isospin is not conserved and so this decay has a very small BR. Only two experiment were capable of observe this channel, for a total world sample of 30 events. Table 2.3 summarizes the measured BR for this channel.

2.3 Theoretical framework for the description of $\psi' \to J/\psi\pi\pi$

In QCD, the hadronic transitions between quarkonium states proceed in two steps: the emission of gluons by the heavy quarks and their subsequent conversion into light hadrons [43].

The gluon momentum scale for these processes is $(M_{\psi'} - M_{J/\psi})/2 \simeq 300$ MeV, so the coupling α_s is large (see Figure 1.2) and the QCD can not be treated perturbatively. Anyway, the heavy quarkonium system dimensions are small compared to the dimension of the light quark emission[2] and the velocity of the heavy quarks is low, allowing a non relativistic treatment and the application of the multipole expansion for the gluon field [44]. In this model, different hadronic final states are originated by different multipole gluon emission.

In analogy to the electric dipole transition, the chromoelectric dipole transition is described by the hamiltonian [45]:

$$\mathcal{H}_d = -\frac{1}{2} g \xi^a \mathbf{r} \cdot \mathbf{E}^a, \tag{2.23}$$

where g is the strong coupling ($g^2 = 4\pi\alpha_s$), $\xi^a = T_1^a - T_2^a$, with T^a the color SU(3) generators acting on the quark (T_1) and antiquark (T_2), $E_i^a = G_{0i}^a$ is the chromoelectric field ($G_{\mu\nu}$ is the gluon field tensor), so $\mathbf{r} \cdot \mathbf{E}^a$ is the chromoelectric dipole moment.

Voloshin and Zakharov showed that the decay amplitude for $\psi' \to J/\psi\pi\pi$ is proportional to the matrix element describing the soft gluon hadronization [45]:

$$A(\psi' \to J/\psi\pi\pi) = A^{\pi\pi}_{\psi' J/\psi} \cdot \langle \pi\pi | \alpha_s \mathbf{E}^a \mathbf{E}^a | 0 \rangle, \tag{2.24}$$

where the higher multipoles can be neglected. The $A_{\psi' J/\psi}$ coefficient, depending only on the initial and final quarkonium wave function, can be factorized from the hadronization matrix element.

Novikov and Shifman [46], revising the Voloshin - Zakharov model, analized in more detail the transition, introducing the possibility of a small fraction of D wave to the dominant S wave state for the pions in the $(\pi\pi)$ CM system. The decay amplitude can be subdivided into two contributions:

$$A(\psi' \to J/\psi\pi\pi) \sim \sqrt{(S\ wave)^2 + (D\ wave)^2}. \tag{2.25}$$

Their result is that the dipion invariant mass distribution and the π angular distribution are strictly correlated and a single parameter $\mathcal{K}$ can be used to fit both the

[2] The charmonium dimension is of the order of $0.2 \div 0.3$ fm while the dimension scale of the light quark emission is the π wavelength $\lambda \simeq h/p$, of the order of $3 \div 5$ fm.

distributions; the expression for the decay amplitude in this model is:

$$A(\psi' \to J/\psi\pi^+\pi^-) \propto \left[m^2_{\pi\pi} - \mathcal{K}\Delta M^2\left(1 + \frac{2m^2_\pi}{m^2_{\pi\pi}}\right)\right] + \left[\frac{3}{2}\mathcal{K}(\Delta M^2 - m^2_{\pi\pi})\left(1 - \frac{4m^2_\pi}{m^2_{\pi\pi}}\right)\left(\cos^2\theta^*_\pi - \frac{1}{3}\right)\right] \quad (2.26)$$

where $m_{\pi\pi} = \sqrt{(q_1+q_2)^2}$ is the dipion invariant mass, with q_1 and q_2 the four-momentum of the two pions, $\Delta M = M_{\psi'} - M_{J/\psi}$ and $\cos^2\theta^*_\pi$ is the angle between the π and the J/ψ directions of motion in the dipion rest frame. $\mathcal{K} \propto \alpha_s(\mu)\rho^G(\mu)$ is predicted to be in the range $0.15 \div 0.2$, assuming that the fraction of the π momentum carried by gluons $\rho^G(\mu)$ is $\simeq 1/2$. The first term in (2.26) describes the S wave and the second the D wave.

The observable quantity is the decay width, which is given by:

$$\frac{d,\,(\psi' \to J/\psi\pi\pi)}{dm_{\pi\pi}} = (PS)\cdot A^2(\psi' \to J/\psi\pi\pi), \quad (2.27)$$

where (PS) is the three body phase space. The following part of the section describes the comparison of the measured distributions with the theory.

2.3.1 Dipion mass distributions in $\psi' \to J/\psi\pi\pi$

When a 2^3S_1 state decays in a 1^3S_1 state, some phenomenological and theoretical formulas can be obtained which describe the data with good approximation. Measuring the dipion mass distribution is therefore a goor test of QCD.

The mass distribution formula can be parametrized as [47, 45]:

$$\frac{d,}{dm_{\pi\pi}} \propto (PS)\cdot(m^2_{\pi\pi} - \lambda_{\pi\pi}m^2_\pi)^2 \quad (2.28)$$

where the phase space PS is given by:

$$(PS) = \sqrt{\frac{(m^2_{\pi\pi} - 4m^2_\pi)[M^4_\psi + M^4_{\psi'} + m^4_{\pi\pi} - 2(M^2_\psi m^2_{\pi\pi} + M^2_{\psi'}m^2_{\pi\pi} + M^2_\psi M^2_{\psi'})]}{4M^2_{\psi'}}}$$

and $\lambda_{\pi\pi}$ is a parameter that can be obtained from data.

In 1975 T. N. Pham, B. Pire and T. N. Truong [47] suggested a dipion mass distribution with a $\lambda_{\pi\pi}$ in the range 2 to 4, on the basis of transition matrix elements. The theoretical value $\lambda_{\pi\pi} = 2$ was obtained also from T. M. Yan [48]. Anyway, it is not possible to give a model independent theoretical prediction for the factor $\lambda_{\pi\pi}$.

E760 looked at the $m_{\pi\pi}$ distribution for both $J/\psi\pi^+\pi^-$ and $J/\psi\pi^0\pi^0$ channels, as shown in Figure 2.3. The only $\lambda_{\pi\pi}$ measurement comes from BES that obtained

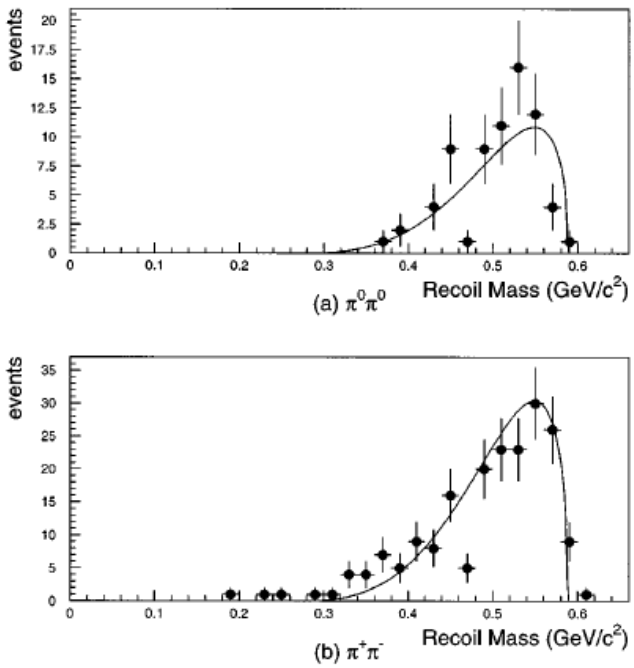

Figure 2.3: Invariant mass recoiling against the J/ψ for (a) $J/\psi\pi^0\pi^0$ and (b) $J/\psi\pi^+\pi^-$ events as observed by E760 experiment [16]. The solid curve is the fit of the data using (2.28) with $\lambda_{\pi\pi} = 4$.

$\lambda_{\pi\pi} = 4.35 \pm 0.06 \pm 0.17$ for the $J/\psi\pi^+\pi^-$ channel [49]. The BES data are reproduced in Figure 2.4.

Novikov and Shifman, revising the Voloshin - Zakharov model, proposed an alternative theoretical approach to describe the features of $\psi' \to J/\psi\pi\pi$ decay [46]. Their result for the dipion mass distribution,obtained integrating (2.26) over the π angular distribution, is:

$$\frac{d,}{dm_{\pi\pi}} \propto (PS) \cdot \left\{ \left[m_{\pi\pi}^2 - \mathcal{K}\Delta M^2 \left(1 + \frac{2m_\pi^2}{m_{\pi\pi}^2} \right) \right]^2 + \frac{\mathcal{K}^2}{5} (\Delta M^2 - m_{\pi\pi}^2)^2 \left(1 - \frac{4m_\pi^2}{m_{\pi\pi}^2} \right)^2 \right\}, \tag{2.29}$$

where $\Delta M = M_{\psi'} - M_{J/\psi}$. By fitting the dipion invariant mass BES found $\mathcal{K} = 0.186 \pm 0.003$ with a $\chi^2/ndf = 55/45$ [49].

2.3.2 π angular distribution for $\psi' \to J/\psi\pi\pi$

In this section we will discuss the expected pion angular distribution for the decay $\psi' \to J/\psi\pi\pi$ on the basis of general assumptions and conservation laws.

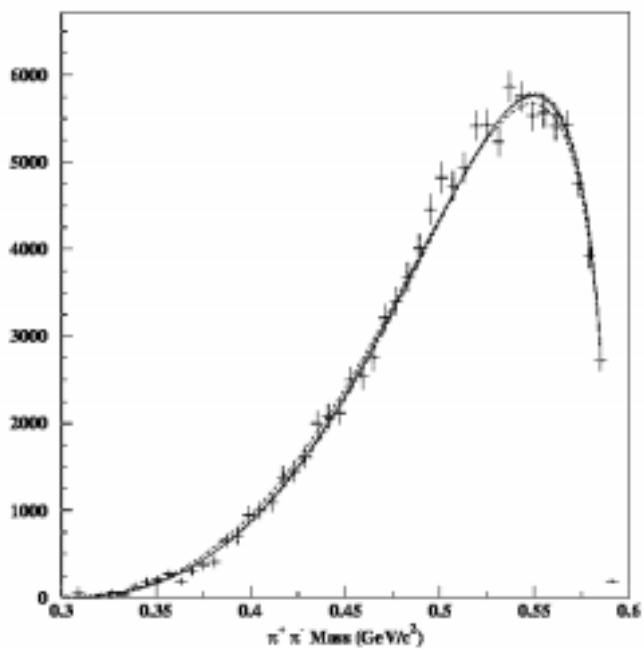

Figure 2.4: $m_{\pi\pi}$ distribution as measured by the BES experiment. The curves refer to fit of the data with three different models, as explained in [49].

Under the hypothesis that the J/ψ and the dipion are in a relative S wave state, supported by the small Q-value of the reaction, we have:

$$\begin{aligned} & 2^3S_1 \;\to 1^3S_1 + (\pi\pi) \\ J^{PC}: \quad & 1^{--} \;\to 1^{--} + L^{++} \\ I^G: \quad & 0^- \;\to 0^- + 0^+ \end{aligned}$$

where L is the angular momentum of the $(\pi\pi)$ system. The parity of the dipion is given by:

$$P = (-1)^L = +1,$$

therefore L must be even; the experimental observations suggest that the decay occurs mainly in a $L = 0$ dipion with at most a small fraction of $L = 2$.

The angular momentum state of $\bar{c}c$ system for the ψ' can be described as:

$$|J, L, S, m_J\rangle = |1, 0, 1, m_J\rangle, \tag{2.30}$$

where m_J gives the charmonium polarization. The theoretical framework for the description of the transition is, as for the dipion mass distribution, the gluon emission followed by hadronization. For chromoelectric dipole $E1$ gluon radiation it is $\Delta L =$

± 1, $\Delta S = 0$; in the gluon multipole expansion the transition is dominated by $E1E1$ gluon radiation and the $\bar{c}c$ system, after the transition, will be in the state:

$$|J', L'(= L, L \pm 2), S, m_{J'}\rangle = |1, (0,2), 1, m_{J'}\rangle. \tag{2.31}$$

In the transition from ψ' to J/ψ , the angular momentum of the $\bar{c}c$ system does not change ($L' = 0$) and this means that the two gluons g_1 and g_2 are emitted with opposite polarizations, i.e. $m_J(g_1) + m_J(g_2) = 0$. For the angular momentum conservation $m_J(g_1) + m_J(g_2) = m_J(\psi') - m_J(J/\psi)$, meaning that the ψ' and the J/ψ have the same polarization, as was mentioned in Section 1.2.

The wave function describing the dipion decay can be written as:

$$\Psi(\theta^*_\pi, \phi^*_\pi) = AY^0_0(\theta^*_\pi, \phi^*_\pi) + BY^0_2(\theta^*_\pi, \phi^*_\pi) \tag{2.32}$$

where θ^*_π, ϕ^*_π are the polar and azimuthal angles in the dipion rest frame between the π and the J/ψ directions. The expected pion distribution can be described with:

$$\Psi^*\Psi = A^2|Y^0_0(\theta^*_\pi, \phi^*_\pi)|^2 + 2AB|Y^0_0(\theta^*_\pi, \phi^*_\pi)Y^0_2(\theta^*_\pi, \phi^*_\pi)| + B^2|Y^0_2(\theta^*_\pi, \phi^*_\pi)|^2 \tag{2.33}$$

and integrating over ϕ^*_π:

$$\frac{d,}{d\cos\theta^*_\pi} \propto \frac{1}{2} + \frac{B}{A}\sqrt{5}\left(\frac{3}{2}\cos^2\theta^*_\pi - \frac{1}{2}\right) + \frac{B^2}{A^2}\frac{5}{2}\left(\frac{3}{2}\cos^2\theta^*_\pi - \frac{1}{2}\right)^2, \tag{2.34}$$

where the amount of D with respect to S wave is given by the ratio B/A.

The only experiment that was able to measure the amount of D wave dipion in $\psi' \to J/\psi\pi^+\pi^-$ decay is BES [49]. Their data are shown in Figure 2.5; they used the parametrization (2.34) fitting the parameter:

$$\frac{D}{S} = \frac{B}{A}\sqrt{5}\frac{3}{2}. \tag{2.35}$$

Because of their large statistics, BES could also measure the $m_{\pi\pi}$ dependence of D/S; their result is summarized in Figure 2.6.

BES also performed a fit to the data using the Novikov - Shifman parametrization. The function that they used to fit the observed θ^*_π angular distribution is obtained by integrating the theoretical amplitude (2.26) over their measured $m_{\pi\pi}$ distribution and obtaining $\mathcal{K} = 0.210 \pm 0.027$ with a $\chi^2/ndf = 26/40$.

Within the Novikov - Shifman model [46], the $m_{\pi\pi}$ and θ^*_π distribution are strongly correlated. In this approach, the only parameter $\mathcal{K}$ describes both the dipion invariant mass and angular distributions. From the fit to the joint $\cos\theta^*_\pi$ and $m_{\pi\pi}$ distribution with the single parameter $\mathcal{K}$, BES obtained $\mathcal{K} = 0.183 \pm 0.002$ with a $\chi^2/ndf = 1618/1482$ [49].

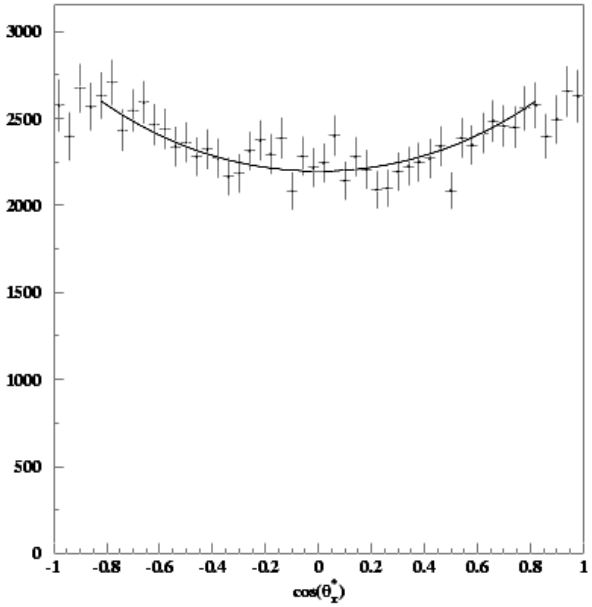

Figure 2.5: $\cos\theta^*_\pi$ (angle between the π and the J/ψ directions of motion in the dipion rest frame) from BES. The points are the data corrected for the efficiency. The curve is the fit result using (2.26) integrated over $m_{\pi\pi}$ [49].

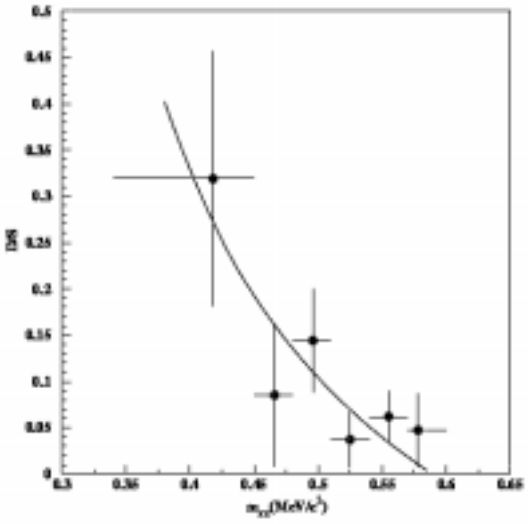

Figure 2.6: Plot of D/S versus $m_{\pi\pi}$ measured by BES. The curve is the prediction of the Novikov-Shifman model [49].

Chapter 3

The Fermilab E835 Experiment

The experiment E835 [50] at Fermilab and its predecessor E760 [51] are designed to study charmonium spectroscopy by forming all $\bar{c}c$ states directly in $\bar{p}p$ annihilation. Until the 90s charmonium was mainly studied in e^+e^- colliders, where e^+e^- pairs annihilate in a virtual photon, and so only $J^{PC} = 1^{--}$ states are directly accessible. All the other states could be accessed only in indirect way, and the detector resolution limits the precision of the measurement.

On the other hand, the annihilation of $\bar{p}p$ allows the formation of all $\bar{c}c$ states directly with a precision which depends only on the knowledge of $\bar{p}$ beam parameters. With the development of the stochastic cooling for the antiproton accumulators during the 80s, $\bar{p}$ beams with very precisely controlled momentum and extremely narrow momentum spread become available, opening the possibility of the study of the charmonium spectroscopy in $\bar{p}p$ annihilation.

The experiments E760 and E835 achieved very precise measurements of mass, widths and branching ratios of all the known charmonium resonances below the open charm threshold.

3.1 Experimental technique

The charmonium can be formed in $\bar{p}p$ collisions with the complete annihilation of the three valence quarks of the proton with the three valence antiquarks of the antiproton, as discussed in Section 1.2.

The antiprotons stored in the Fermilab antiproton accumulator are cooled and decelerated at the desired energy, so the center of mass energy (E_{CM}) of the reaction is determined very accuratey from the measurement of the antiproton beam energy. The resulting error on E_{CM} measurement in E835 is less than 100 keV, as it will be shown in Section 3.2.1.

The cross section of the reaction

$$a + b \to R \to c + d$$

where a resonance R is produced, is given by the Breit-Wigner formula:

$$\sigma_{BW}(E) = \frac{\pi}{k^2}\frac{(2J+1)}{(2s_a+1)(2s_b+1)}\frac{, _{ab}, _{cd}}{(M_R - E)^2 + , ^2/4}, \tag{3.1}$$

where E is the center of mass energy of the reaction, k is the a (and b) momentum in the CM system, s_a, s_b are the initial state particles' spin and M_R is the resonance mass.

The experimental method of E835 consists in a point by point resonance scan obtained moving the energy of the beam on the resonance, as illustrated in Figure 3.1. The beam width (200 $\div$ 300 keV) is in fact narrower than the typical charmonium resonance width (with the exception of J/ψ and ψ').

The shape of the resonance is obtained by simply counting the number of events due to charmonium decay at each point of the scan, which is given by:

$$N_i = \int \mathcal{L}_i dt \left[\sigma_{bkg} + \epsilon \int \sigma_{BW}(E') \cdot G(E' - E) dE'\right], \tag{3.2}$$

where $\mathcal{L}$ is the instantaneous luminosity, σ_{bkg} a term due to the contribution of background events, ϵ the product of acceptance and events detection efficiency, $\sigma_{BW}(E)$ the resonance shape to be measured, as in (3.1), and $G(E' - E)$ is the normalized center of mass energy distribution around the central value E. The mass and width of the resonance are then measured fitting with a Breit-Wigner the measured points after deconvolution of the observed shape with the antiproton beam distribution (which has a gaussian shape).

Once measured the background level σ_B, the area under the excitation curve is independent of the beam spectrum $G(E' - E)$ and is given by:

$$A = \int_0^\infty \sigma_{BW}(E) dE = \frac{\pi}{2}\sigma_{peak}, \tag{3.3}$$

where:

$$\sigma_{peak} = \frac{2J+1}{4}\frac{16\pi\epsilon, _{ab}, _{cd}}{(M_R^2 - 4m_p^2) \cdot , ^2} \tag{3.4}$$

and the product σ_{peak}, can be obtained directly from the measured area of the excitation curve.

3.2 The machine

The Fermilab antiproton accumulator was built to store $\bar{p}$ before their injection into the Tevatron collider. The $\bar{p}$ beam supplied is suitable for the formation of charmonium in $\bar{p}p$ annihilation, that can be obtained with the insertion of a proton

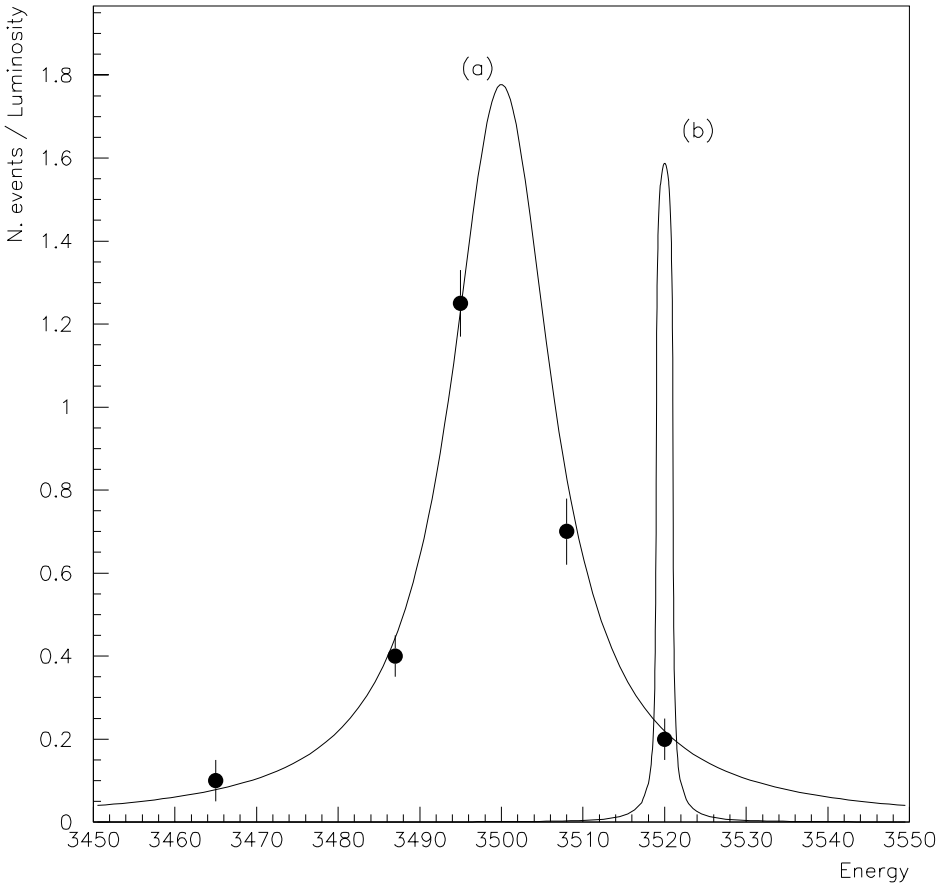

Figure 3.1: Resonance scanning procedure (arbitrary units on axis). The plot shows a 5 points scan of the resonance (a). Each point is obtained moving the beam energy, with the center of mass energy distribution represented in (b), on each desired energy value and counting the number of events in a given final state. Then the number of events is divided by the luminosity (black dots). The resonance parameters are obtained from the observed distribution by deconvolution of the beam width.

target in the accumulator. The E835 detector is located into the AP50 pit of the antiproton accumulator. A hydrogen cluster target has been developed to allow data taking at high and constant luminosity. The luminosity is measured counting $\bar{p}p$ elastic collisions by means of a solid state detector in a small solid angle at $\sim 90°$ in the laboratory.

3.2.1 Antiproton accumulator

The Fermilab antiproton accumulator is used mainly to store $\bar{p}$ and to cool and debunch them before being injected into the Tevatron. During E835 data taking it is used in a different way: antiprotons are accumulated for several hours at a rate of ~ 3 mA/hour until a current of about 50 mA is reached (corresponding to $\sim 5 \cdot 10^{11}$ $\bar{p}$).

Then the debunching and cooling of the $\bar{p}$ takes place: the antiprotons are decelerated to the desired center of mass energy. At this point the H_2 jet target is turned on and annihilation reactions can occur. Accumulation is not possible with the jet target on: data taking lasts until $\bar{p}$ beam is completely used. Since the hydrogen target is at rest in laboratory, the center of mass energy of the reaction products is:

$$\sqrt{s} = \sqrt{2m_p(m_p + E_{\overline{p}})}.$$

The energy of the antiproton beam is obtained by measuring the antiprotons speed β, given by the product of the orbit length L and the revolution frequency f:

$$\beta = L \cdot f.$$

The orbit length measurement is calibrated with respect to a reference orbit, with length L_0, determined with a scan of the ψ' resonance whose mass is known from e^+e^- experiments with an uncertainty of ± 90 keV; the error on L_0 obtained in this way is $\simeq 2 \cdot 10^{-6}$. The $\bar{p}$ energy can be changed by moving the beam orbit. The length $L = L_0 + \Delta L$ is calculated from the measurement of the transverse beam position, using the Beam Position Monitor (BPM) system, with a precision of half a millimeter [52].

The precision on the energy measurement is related to the orbit length L and to the revolution frequency f measurements through the relation:

$$\frac{\delta\sqrt{s}}{\sqrt{s}} = \frac{\beta^2\gamma^3}{2(1+\gamma)}\sqrt{\left(\frac{\delta f}{f}\right)^2 + \left(\frac{\delta L}{L}\right)^2},$$

where

$$\gamma = \frac{E_{\overline{p}}}{m_p} = \frac{1}{\sqrt{1-\beta^2}}.$$

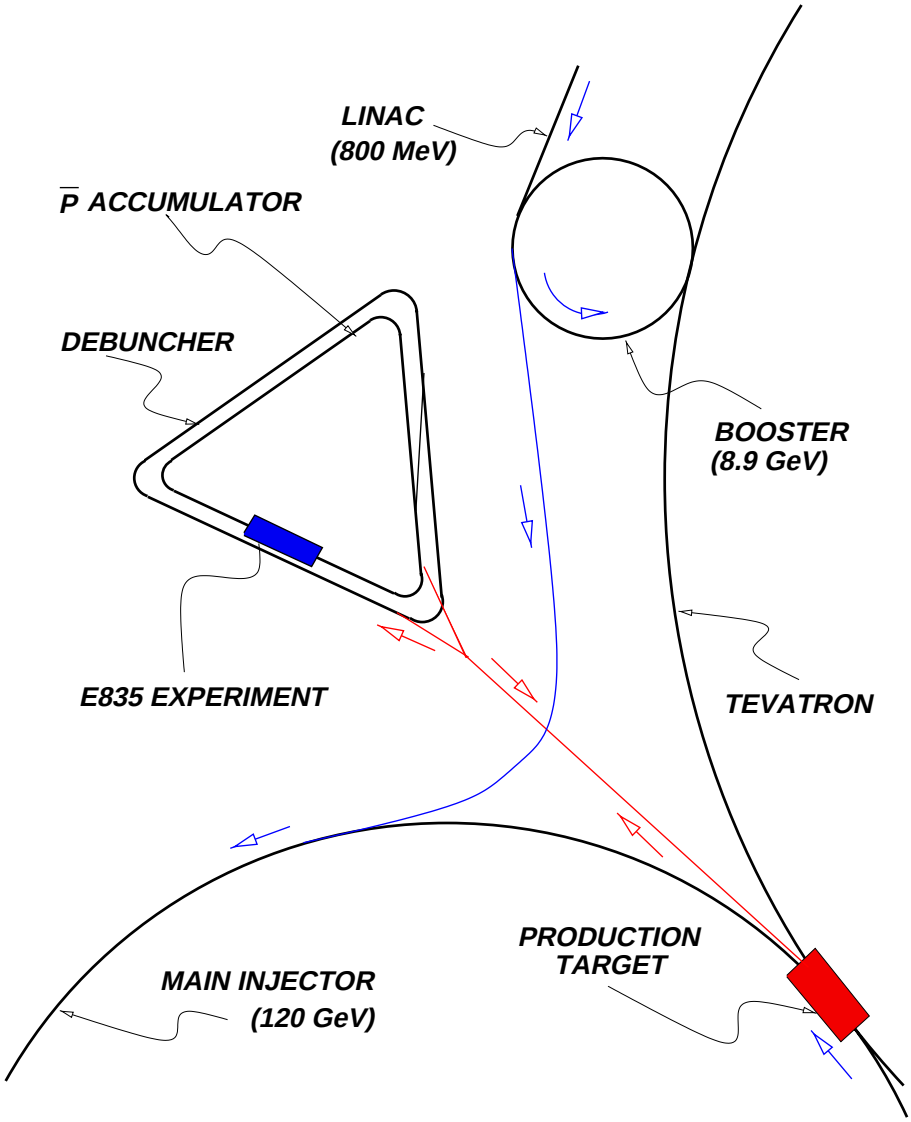

Figure 3.2: Fermilab antiproton accumulator and location of the E835 experiment.

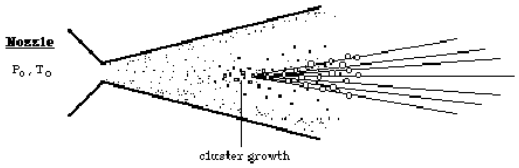

Figure 3.3: Nozzle with illustration of cluster growth mechanism.

With this procedure the total error on center of mass energy is of the order of 100 keV.

The momentum spread of the beam is given by:

$$\frac{\Delta p}{p} = \frac{1}{\eta}\frac{\Delta f}{f},$$

where η is the slip factor of the machine. The typical Δp value for E835 is 200 keV in the center of mass frame.

3.2.2 Jet target

The target [53] is composed of high density and low temperature hydrogen clusters at rest in the laboratory. It is located on the Fermilab antiproton accumulator. The clusters are produced by the expansion of H_2 gas through a convergent and divergent nozzle (see Figure 3.3), operated at a temperature around 30 K. The nozzle is trumpet-shaped with an opening angle of 3.5°, a divergent length of 8 mm and a throat diameter of 37 μm.

The operating conditions can be obtained from Figure 3.4. The cluster density can be increased during the data taking in order to collect data at high luminosity, while the antiproton beam current decreases. An example of luminosity measurement during 16 hours of data taking is showed in Figure 3.5.

3.2.3 Luminosity monitor

The luminosity is measured by counting the number of $\overline{p}p \to \overline{p}p$ events in a small solid angle region.

The luminosity monitor [54] consists of three solid state detector located below the interaction point at a polar angle of 86.4°, as shown in Figure 3.6, at the bottom of a vacuum horn. One of the solid state detectors is mounted on a movable tray, the other two are fixed and located at its sides. The presence of three detectors gives also informations on the possible radial displacement of the interaction region with respect to the luminosity monitor by looking for the asymmetry in the number of counts of the two fixed detectors. The active surface of each detector is (1×5) cm^2 and their thickness is 0.5 mm.

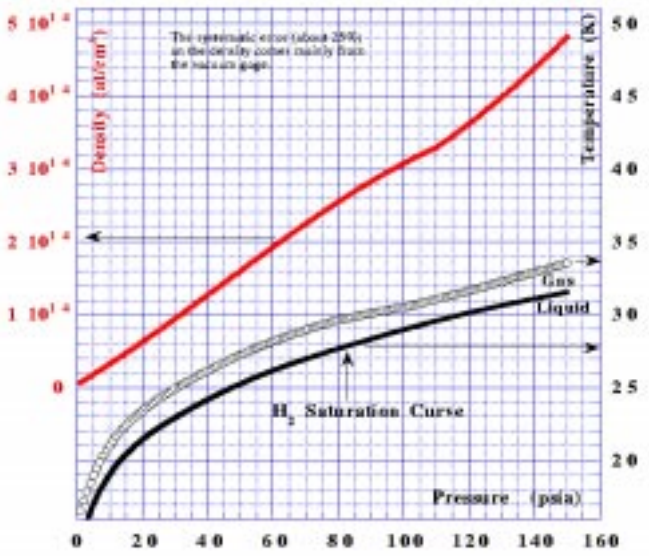

Figure 3.4: Plot of the dependence of the jet density as a function of the temperature and of the pressure at the nozzle. To obtain a high luminosity, the operating temperature - pressure (open circles) is set close to the liquid - gas border (black solid line).

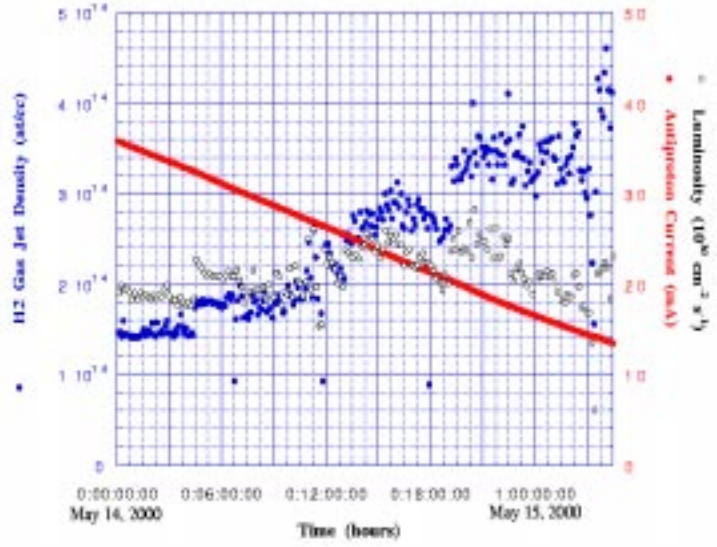

Figure 3.5: Luminosity control during one day of data taking. As the antiproton beam current decreases the jet density is increased to keep the instantaneous luminosity constant at $2 \cdot 10^{31}\mathrm{cm}^{-2}\mathrm{s}^{-1}$.

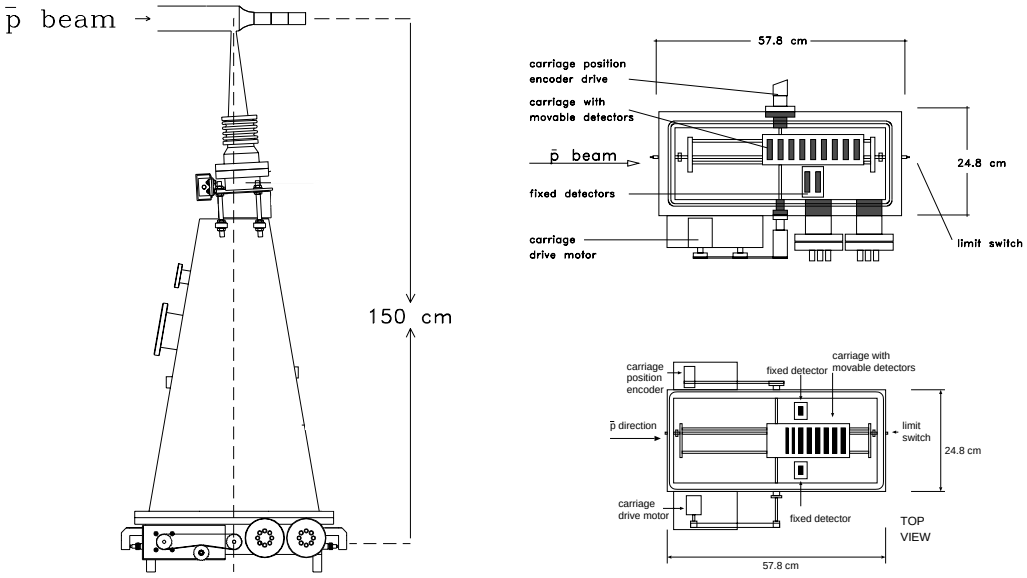

Figure 3.6: Luminosity monitor.

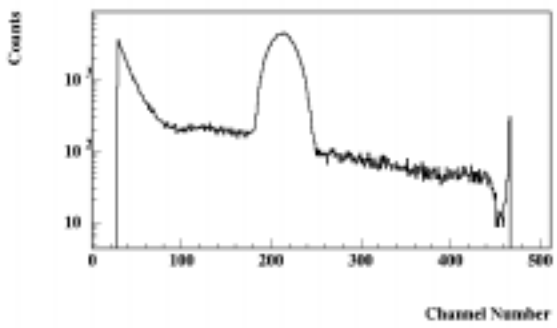

Figure 3.7: Typical proton recoil spectrum from one solid state detector.

A typical proton recoil spectrum is shown in Figure 3.7. The background is at the level of $\sim 2-3\%$ of the peak and can be easily subtracted. The instantaneous luminosity is determined averaging on a two minutes period of data taking. The error on the luminosity measurement is below 3%.

The differential cross sections for $\bar{p}p$ elastic scattering are shown in Figure 3.8.

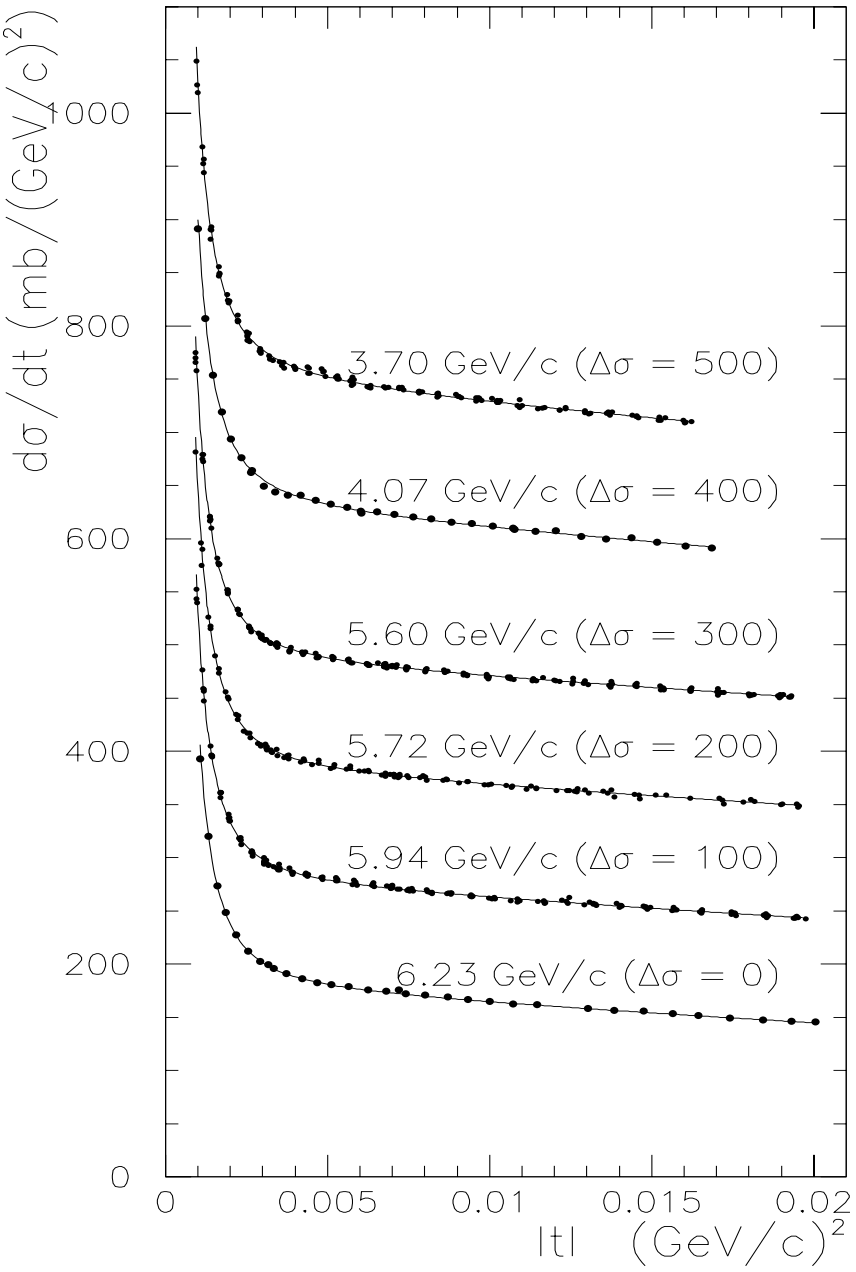

Figure 3.8: The measured differential cross sections for six $\bar{p}$ beam momentum. The data were taken by Fermilab E760 with the luminosity monitor movable detectors [55].

3.3 The detector

E835 detector is a non magnetic spectrometer, with a cylindrical geometry around the beam axis, designed in order to detect electromagnetic final states. The charmonium is produced with a boost in the laboratory so the detector is located downstream with respect to the interaction region to increase the total acceptance. Figure 3.9 shows a sketch of the detector.

An electromagnetic calorimeter system and a Čerenkov counter system are designed to detect the e^+e^- decay of the J/ψ and to separate it from the huge hadronic background. Also multi-γ final states are detectable with the calorimeter.

The detector is completed by the inner tracking system, allowing the study of channels with charged hadrons in the final state.

3.3.1 Electromagnetic calorimeter system

The calorimetric system is composed by two electromagnetic calorimeters: the central (CCAL) and the forward (FCAL), with different properties.

Central calorimeter

The central calorimeter [56] has a cylindrical symmetry and is composed of 1280 Schott F2 lead glass Čerenkov counter blocks (a summary of characteristics is given in Table 3.1), arranged in 20 rings and 64 wedges and with length varying from 37.80 cm (ring 1) to 50.00 cm (ring 20). Each block points at the interaction region. The blocks layout is shown in Figure 3.10.

The CCAL allows the measurement of the position and the energy of electrons, positrons and photons. The angular resolution is 11 mrad for the azimuthal angle ϕ and 6 mrad for the polar angle θ. The energy resolution is given by:

$$\frac{\sigma(E)}{E} = 1.4\% + \frac{6\%}{\sqrt{E(\mathrm{GeV})}}. \tag{3.5}$$

The angular coverage is between 10.6° and 70.0° in the laboratory, corresponding to a range from 37° to 137° in the center of mass for $e^{\pm}$ at the ψ' energy.

Forward calorimeter

FCAL [57] is formed by an array of 144 parallelepiped lead glass blocks of 3 different kind (16 large, 80 medium and 48 small blocks) located as shown in Figure 3.11). Each block is optically coupled through its rear end to a photomultiplier.

The angular coverage is between 3.3° and 11.0° and the thickness corresponds to $13 \div 21$ radiation lengths.

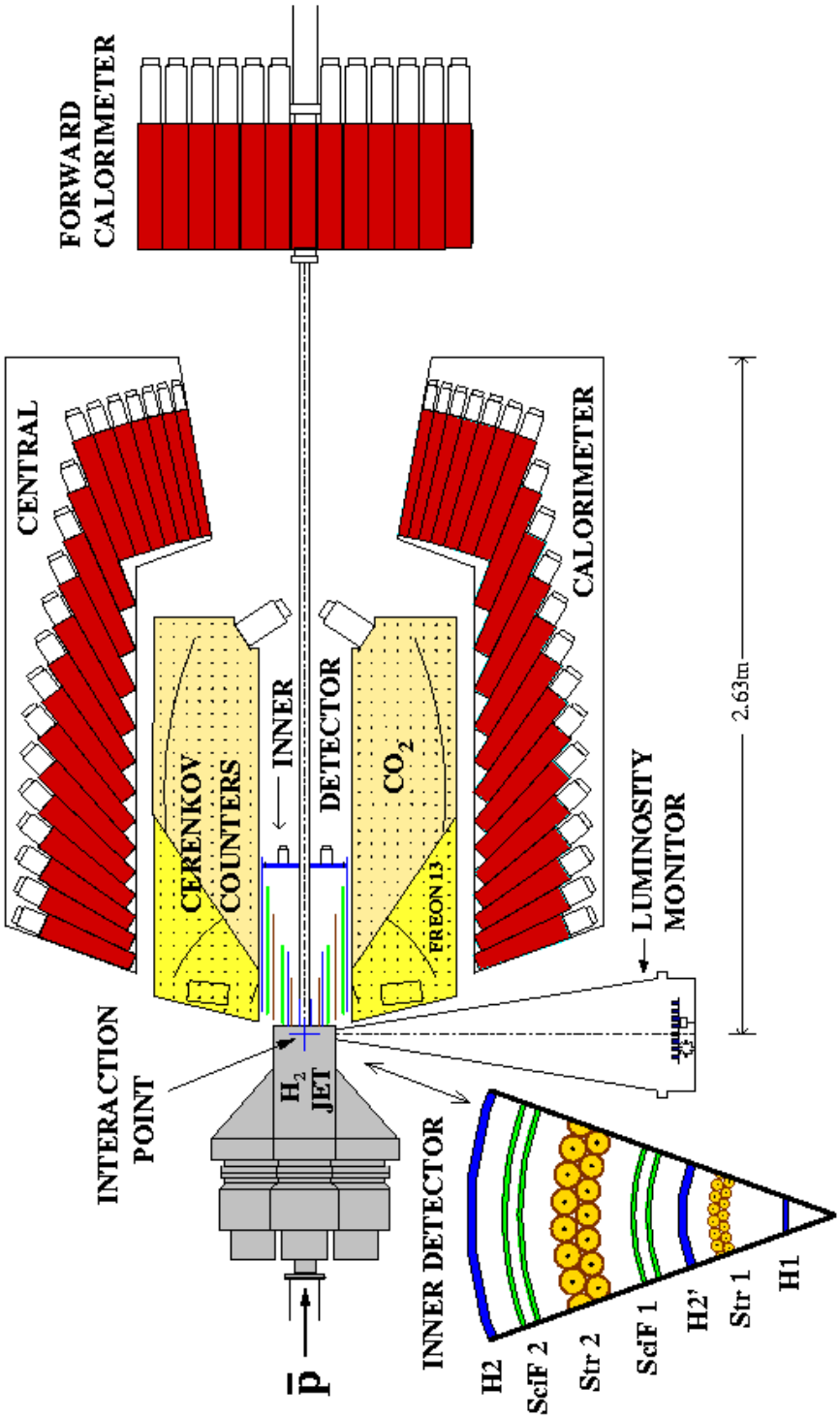

Figure 3.9: Schematic of E835 detector.

Radiation length	3.141 cm
Density	3.61 g cm^{-3}
Refractive index at 404.7 nm	1.651
Composition by weight:	
Lead	42.2 %
Oxygen	29.5 %
Silicon	21.4 %
Potassium	4.2 %
Sodium	2.3 %
Arsenic	0.15 %
Transmittance through 10 cm:	
Wavelength (nm)	Transmittance
335 - 344	56.9 %
385 - 394	95.5 %
435 - 444	97.9 %
485 - 494	98.4 %
535 - 544	98.9 %
585 - 594	99.4 %

Table 3.1: Summary of characteristics of Schott F2 lead glass.

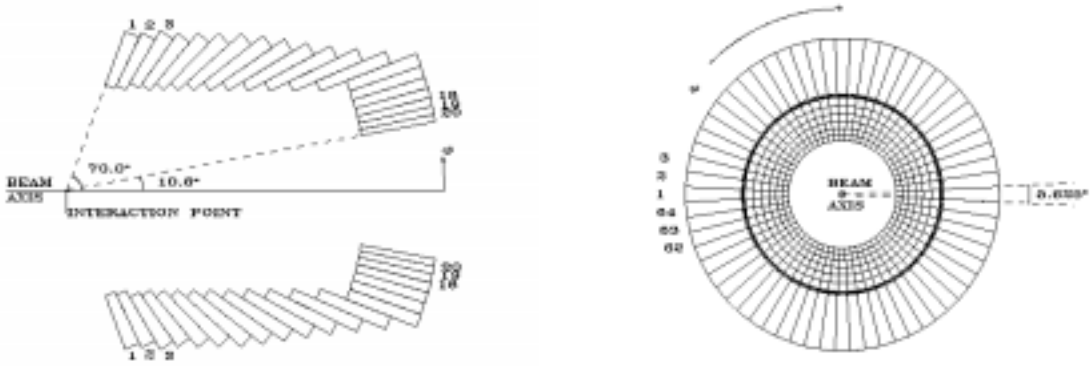

Figure 3.10: CCAL sections and numbering scheme for blocks.

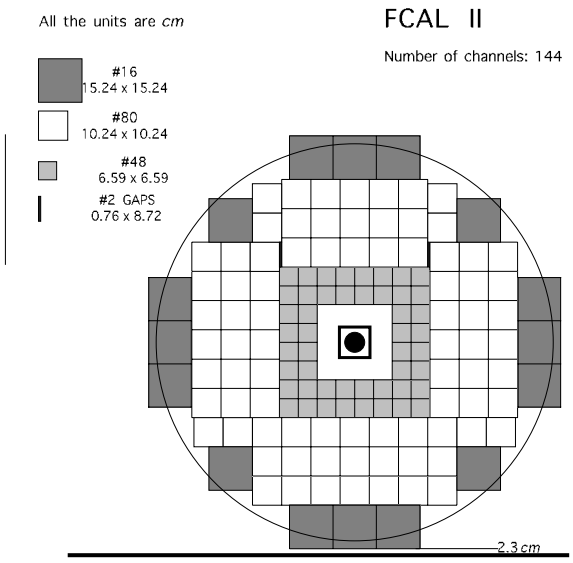

Figure 3.11: FCAL front view.

3.3.2 Čerenkov counters

The disadvantage of the charmonium spectroscopy in $\bar{p}p$ annihilation is that $\bar{c}c$ decay signal have to be identified in an overwhelming hadronic background produced in $\bar{p}p$ interaction. One solution, adopted by E835, is to select electromagnetic final states by looking for high invariant mass e^+e^- due to $J/\psi, \psi' \to e^+e^-$ decays.

When a relativistic charged particle crosses a medium with an index of refraction $n > 1/\beta$, light is produced. The E835 Čerenkov detector [58] has been built to give light signal only if crossed by high energy $e^{\pm}$. The charged hadrons with highest velocity that are produced in the E835 apparatus are $\pi^{\pm}$ from $p\overline{p} \to \pi^+\pi^-$. If the Čerenkov threshold is set above these $\pi^{\pm}$ velocity, all the hadronic background produced can be rejected.

The detector is composed by 16 gas cell Čerenkov counters located around the beam pipe with cylindrical symmetry (each octant has an upstream and a downstream cell, because of the different velocity for charged hadrons at different angles due to the Lorentz boost). The inner radius is 17 cm, the outer one 59 cm. Each octant has an angular coverage between 15° and 65° and is divided in a forward and in a backward chamber between 34° and 38° (see Figure 3.12).

The selection of the gas filling for both kind of cell is based on the capability to distinguish $e^{\pm}$ from $\pi^{\pm}$: the forward chamber is filled with CO_2, for the backward one Freon 13 (CF_3Cl) or Freon 12 (CF_3Cl_2), which have an higher refraction index to compensate the smaller boost of the particles, have been used. A summary of Čerenkov counter parameters is shown in Table 3.2.

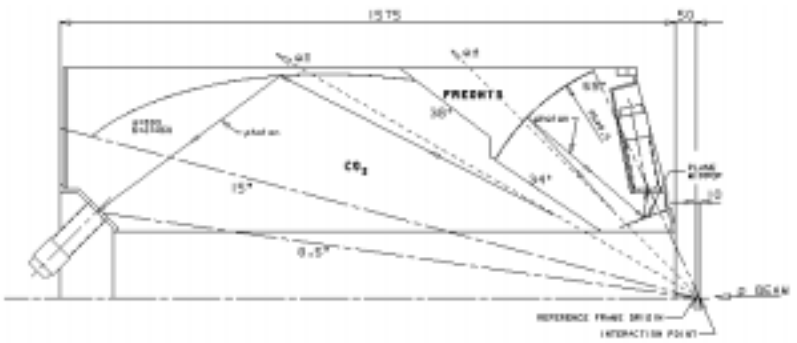

Figure 3.12: Čerenkov octant section.

	Forward	Backward	
Angular aperture	$15° < \theta < 38°$	$34° < \theta < 65°$	
Gas	CO_2	Freon 13	Freon 12
Refractive index	1.000410	1.000720	1.001080
π threshold (GeV/c)	4.873	3.677	3.003
Light collection efficiency	$0.84 \div 0.90$	$0.84 \div 0.98$	$0.75 \div 0.88$

Table 3.2: Physical parameters of the Čerenkov counter.

3.3.3 Charged tracking system

The charged tracking system is the innermost part of the detector. It is composed by 4 hodoscopes (3 around the beam axis and one in the forward direction, used as a veto), 2 straw chambers (for ϕ measurement) and 2 scintillating fiber detectors (for θ measurement).

It is used both to trigger on charged events and to obtain a precision measurement of the charged track directions. It allows the reconstruction of channels with charged hadrons in the final state, like $p\overline{p} \to J/\psi\pi^+\pi^-$ and $p\overline{p} \to \phi\phi \to 4K^{\pm}$.

Hodoscopes and veto

Three scintillator detectors with cylindrical geometry are installed in the inner detector. They are located around the beam pipe and are segmented along the azimuthal angle ϕ. The innermost, called H1, is made of 8 plastic scintillators, 2 mm thick, located at a radius of 2.5 cm. The geometrical θ acceptance is from 9° to 65°. The second hodoscope, H2', is composed of 24 rectangular elements at 7 cm from the beam pipe axis. Each element is 4 mm thick and covers the angular region $9° < \theta < 65°$. The outermost, H2, is made of 32 elements and is located at 17 cm from the beam pipe axis. Its θ angular coverage goes from 12° to 65°. The hodoscopes have full acceptance in ϕ (in fact, because of the cracks between its elements, the acceptance of H1 is 96%).

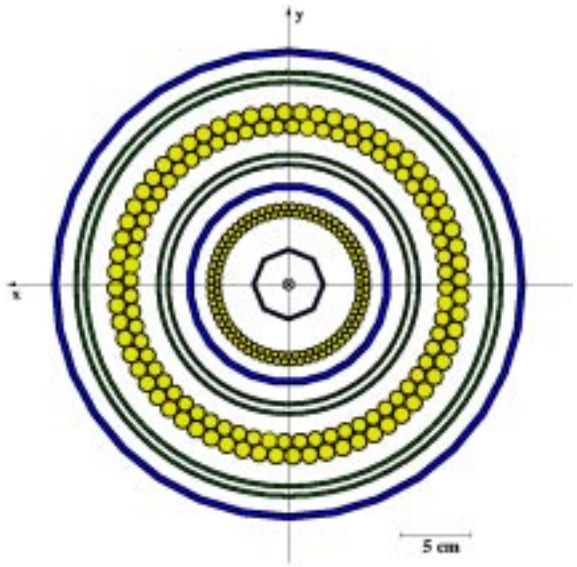

Figure 3.13: Front section view of the charged tracking system. Starting from the center one can see: H1 (8 segments), inner straw chamber (2 layers), H2′ (24 segments), inner scintillating fiber detector (2 layers), outer straw chamber (2 layers), outer scintillating fiber detector (2 layers) and H2 (32 segments).

An additional hodoscope (VETO) is located at the forward endcap of the tracking system. It is composed of 8 trapezoidal scintillators 2 mm thick, covering the θ angular region below 12°, where no tracking devices are present.

Straw chambers

Two cylindrical chambers, each one consisting of two staggered layer of 64 proportional tubes, are used to determine the azimuthal angle for charged particles: for each mylar tube (80 μm thickness), a 20 μm gold plated tungsten anode wire was taut on its axis. The staggered design allows to solve the left-right ambigu-

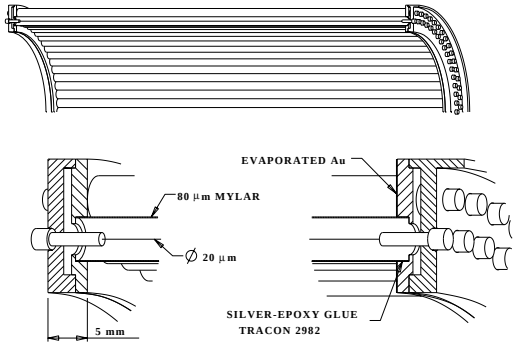

Figure 3.14: Sketch of the mechanical structure of a Straw Chamber.

	R (cm)	θ	$\oslash$ (mm)	L (mm)
Inner	5.4	$15° \div 58°$	5.0 - 5.4	182
Outer	12.0	$15° \div 65°$	11.1 - 12.1	414

Table 3.3: Geometrical parameters of the straw chambers.

Layer	R (mm)	n. fibers	pitch (mm)	θ
1	85.0	240	1.10	$15° \div 55°$
2	92.0	240	1.19	$15° \div 55°$
3	144.0	430	1.10	$15° \div 65°$
4	150.6	430	1.15	$15° \div 65°$

Table 3.4: Geometrical parameters of the scintillating fibers tracker.

ity of the position of the track with respect to the anode wire. The geometrical parameters are summarized in Table 3.3. The straw chambers are operated with Ar:C_4H_{10}:$(OCH_3)CH_2$ - 82:15:3 at 1320 V (inner) and 1530 V (outer).

The efficiency in the E835 fiducial region ($15° < \theta < 60°$) for the reconstrucion of a track is above 95%, with an efficiency of $\sim 90\%$ per layer.

Scintillating fiber tracker

The scintillating fiber tracker [59] is the device used to measure the polar angle θ for charged particles. It is composed of four layers of scintillating fibers wounded around plexiglas cylinder supports, with full ϕ acceptance. They are subdivided in two detectors, each of them being composed of two layers of fibers in staggered positions to increase the acceptance. The main construction characteristics are summarized in Table 3.4. A sketch of the tracker is shown in Figures 3.15 and 3.16.

The scintillating fibers used, Kuraray SCSF-3HF-1500, have a diameter of 0.835 mm (0.760 mm diameter active core). They are thermally spliced to clear fibers at one end to bring the light signal to the photodetectors. The other end has been made reflective by deposition of a thin alluminum layer, in this way the light is reflected back into the fiber and so the light yield to the photodetector is increased.

The photons from the fibers are then converted in electric signal by the Visible Light Photon Counters (VLPC), semiconductor devices developed by Rockwell International, with high gain and quantum efficiency. The working point of the VLPCs is at a temperature of about 6.5 K, so they are located in a liquid He cryostat. The layout of the tracker and readout electronics is shown in Figure 3.17.

The detector efficiency is above 98% at small angles (where more than one fiber per layer is expected to be crossed by a track) and decreases to $\sim$80% at large angles, where the geometrical acceptance is reduced by the spacing between the fibers.

The intrinsic angular resolution of the detector ranges from $\sim$1 mrad (at small angles) to $\sim$4 mrad and has been measured with $\bar{p}p$ events. Anyway, for slow charged

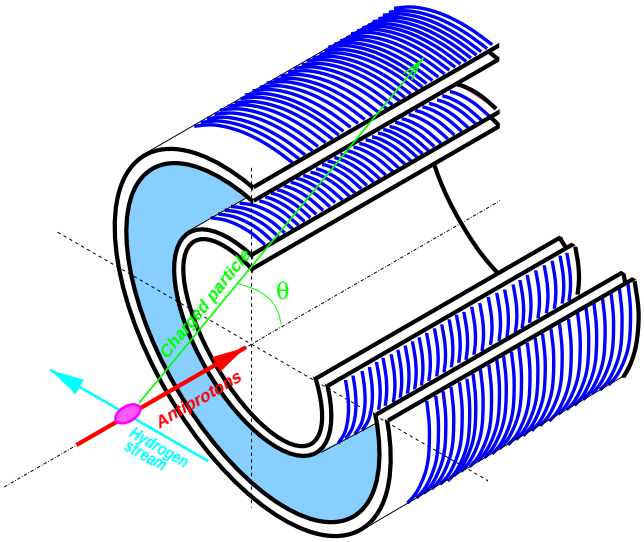

Figure 3.15: Schematic view of the scintillating fiber tracker. Fibers are wounded around plexiglas cylinders around the beam pipe for the measurement of the polar angle θ of charged particles.

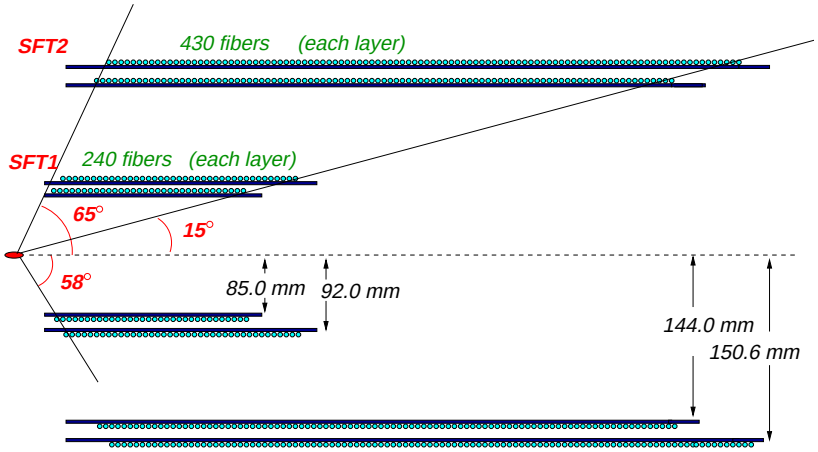

Figure 3.16: Section of scintillating fiber tracker.

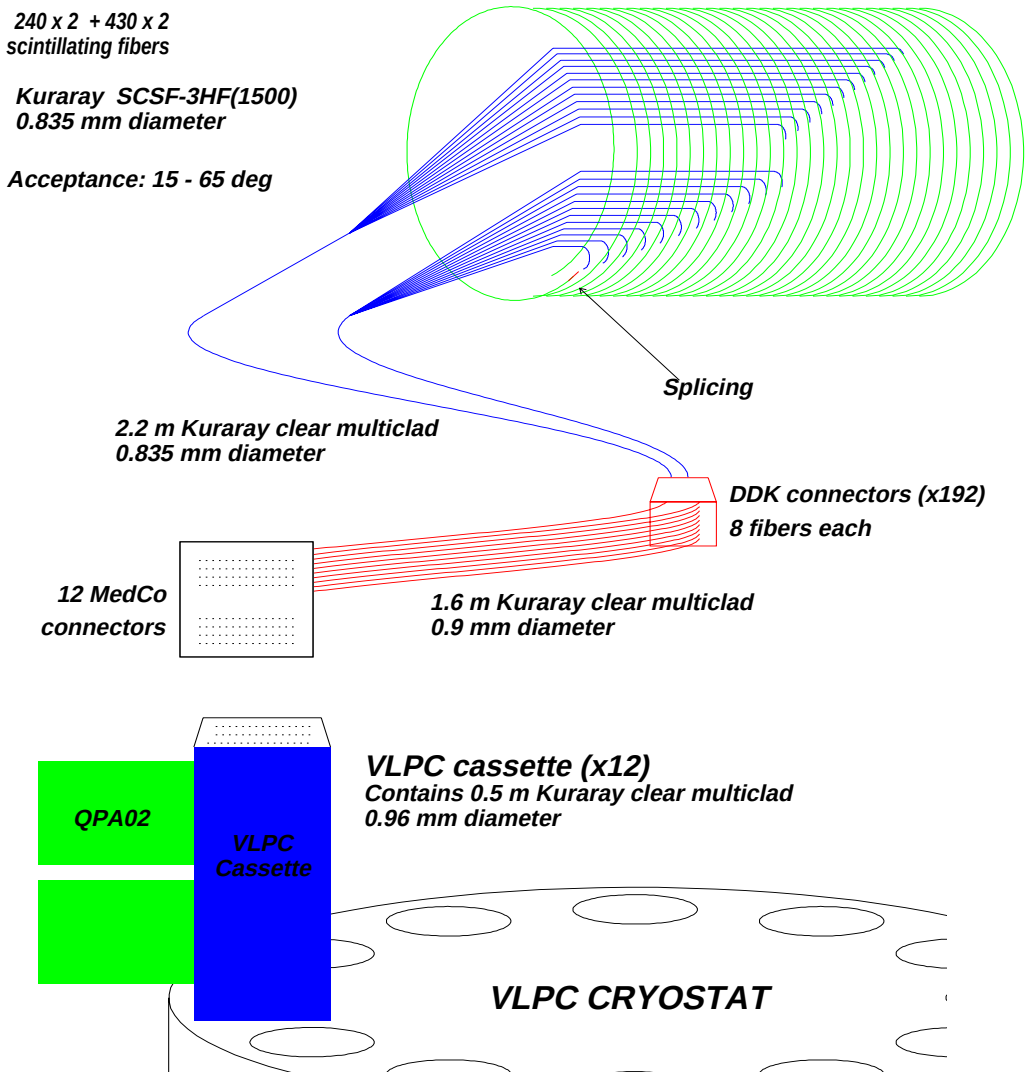

Figure 3.17: Layout of scintillating fiber tracker and readout electronics.

particles, the angular resolution is dominated by the multiple scattering and this has to be taken into account in the event reconstruction stage.

3.4 The trigger

E835 has two different main triggers:

1. the charged trigger to detect charged events, mainly from $J/\psi,\ \psi' \to e^+e^-$ events and $\phi\phi \to 4K^\pm$ events;

2. the neutral trigger to detect $\gamma\gamma$ events and multiphotons final states coming from $\bar{p}p$ annihilation in light neutral hadrons (π^0, η, ω).

3.4.1 Charged trigger

The charged trigger has been designed mainly to select the electromagnetic decay of the charmonium states, i.e. $J/\psi, \psi' \to e^+e^-$. The only charged hadronic channel that has been studied is the decay into two ϕ mesons through $\phi\phi \to 4K^\pm$. In this channel it is possible to study $^1S_0$ and $^1P_1$ $\bar{c}c$ resonances such as $\eta_c \to \phi\phi$ and $h_c \to \eta_c\gamma \to \phi\phi\gamma$.

The input signals for the charged trigger are the outputs of the hodoscopes, the scintillating fiber detectors, the Čerenkov counters and CCAL.

e^+e^- events are selected using the information on the energy deposition in CCAL and requiring the 2 Čerenkov hits corresponding to the e^+e^- candidates.

For the $\phi\phi$ selection, the selection is based mainly on the peculiar kinematics of the $4K^\pm$. The scintillating fiber detectors provide the θ information to the first level trigger, used for the kinematics cuts. More details about the $\phi\phi$ trigger can be found in [60].

For the final states studied in this thesis the relevant trigger is the one which selects e^+e^-X events, which is described as follows:

$$\begin{aligned}(e^+e^-) &= (2e) \otimes (H2 \leq 5) \otimes (PBG3) \\ &\oplus (1e) \otimes (2h) \otimes (H2 = 2) \otimes (H2copl1/3) \otimes (PBG3) \\ &\oplus (2e) \otimes (H2 = 2) \otimes (H2copl1/3) \otimes \overline{(FCH)}\end{aligned}$$

where $\oplus$ is the logic OR, $\otimes$ is the AND between:

- $(1h)$: we call *hadron track* the AND between one H1 element and the OR of the corresponding 6 H2 elements[1];

- $(2h)$: requires 2 hadron tracks $(1h)$;

[1] Because of the cracks between the eight H1 elements, the ϕ coverage of H1 is the 96% of the full azimuthal angle. This is one of the most important sources of (e^+e^-) trigger inefficiency.

- $(1e)$: an *electron track* is the AND of $(1h)$ and the OR of the two (backward and forward mirrors) corresponding Čerenkov counters;
- $(2e)$: requires 2 electron tracks $(1e)$;
- $(H2 \leq 5)$: requires a number of H2 elements ≤ 5;
- $(PBG3)$: CCAL trigger logic; it will be described in Section 3.4.2;
- $(H2copl1/3)$: if one H2 element is hit, this logic requires that at least one of the 3 opposite elements must be hit;
- $\overline{(FCH)}$: forward hodoscope in veto.

The (e^+e^-) trigger can be schematized as the OR of three branches:

$$\begin{aligned}(b1) &= (2e) \otimes (H2 \leq 5) \otimes (PBG3),\\ (b2) &= (1e) \otimes (2h) \otimes (H2 = 2) \otimes (H2copl1/3) \otimes (PBG3),\\ (b3) &= (2e) \otimes (H2 = 2) \otimes (H2copl1/3) \otimes \overline{(FCH)}.\end{aligned}$$

While all the three (e^+e^-) branches will trigger on $J/\psi + neutral$ events, the presence of the requirement $(H2 = 2)$ in $(b2)$ and $(b3)$ makes them very inefficient for the detection of $J/\psi\pi^+\pi^-$ events. Therefore, the trigger efficiency for this channel is expected to be lower than the one for $J/\psi + neutral$ events.

3.4.2 Neutral trigger

The neutral trigger [61] is constructed using signals from CCAL alone and is designed to trigger mainly on the charmonium electromagnetic final states, with two high invariant mass clusters coming from two photons or electrons, and multiphoton final states coming from $\bar{p}p$ annihilation into light mesons (π^0, η, ω).

The 20 CCAL rings are grouped into 5 "super rings" and the 64 wedges into 8 "super wedges". Each "super cluster" spans 5 rings and 9 wedges (with one overlapping channel to avoid border hit inefficiencies).

The output of the neutral trigger are the following:

- $(PBG1)$ requires that the inputs corresponding to two back to back super wedges are both on (consistency with two body kinematics, mainly to trigger on e^+e^- and $\gamma\gamma$ events);
- $(PBG3)$ similar to $(PBG1)$ but looser: the coincidence is between one super wedge and the opposite three (mainly for $e^+e^-\gamma$, where coplanarity should not be strictly required);
- $(ETOT-HI)$ requires the total sum of CCAL blocks energy deposition above 80% of the available energy;

- $(ETOT - LO)$ same as $(ETOT - HI)$ but the threshold is at 70% of the available energy.

3.5 The data acquisition system

Figure 3.18 shows the E835 data acquisition system (DAQ). Three SGI computers are used to coordinate, process, filter, log and monitor the data streams. An Indy does the run control (coordination of independent data streams), monitors the DAQ streams and communicates with the CAMAC branches; a Challenge-L with four 150 MHz processors is used for the event building, filtering and logging; an Indigo for the event display.

Data from the detector are read out by FERA ADC (LRS4300) and TDC (LRS3377), organized in CAMAC crates. All the information from the modules in a single crate are passed to DYC modules, intermediate FIFO buffers, and then to Access Dynamics DC2/DM115 modules. Then the gateway process writes the two DC2 sets of data in a reserved part of the Challenge-L memory. When a gateway buffer is available, the online filter process runs on the stored events and all the non rejected events are copied to logging buffers for the recording to tape and transfer to Indigo for monitoring.

The event size is approximately 1kbyte. The total trigger rate is of the order of the kHz yielding a rate of events to tape of $\sim$ Mbyte/s.

The beam parameter data stream is controlled by a network system called ACNET (accelerator control network).

The readout electronics of the luminosity monitor data stream is arranged in a CAMAC crate. Every two minutes a process running on the Indy computer reads the three silicon detectors data and writes the luminosity value to disk.

The luminosity monitor crate contains also the electronic readout of the scaler data stream.

3.6 Offline event reconstruction software

All the detector hits are grouped into clusters, used to form the tracks for the event reconstruction. The two detectors giving information about particles direction and energy are the charged tracking system and the calorimeters. In this section we will explain how the information is used to identify the final state.

3.6.1 Cluster formation

All the straw chamber, scintillating fibers tracker and calorimeter hits are grouped in clusters. A cluster is composed by a pattern of adjacent hits and is considered to be generated by a single particle crossing the detector.

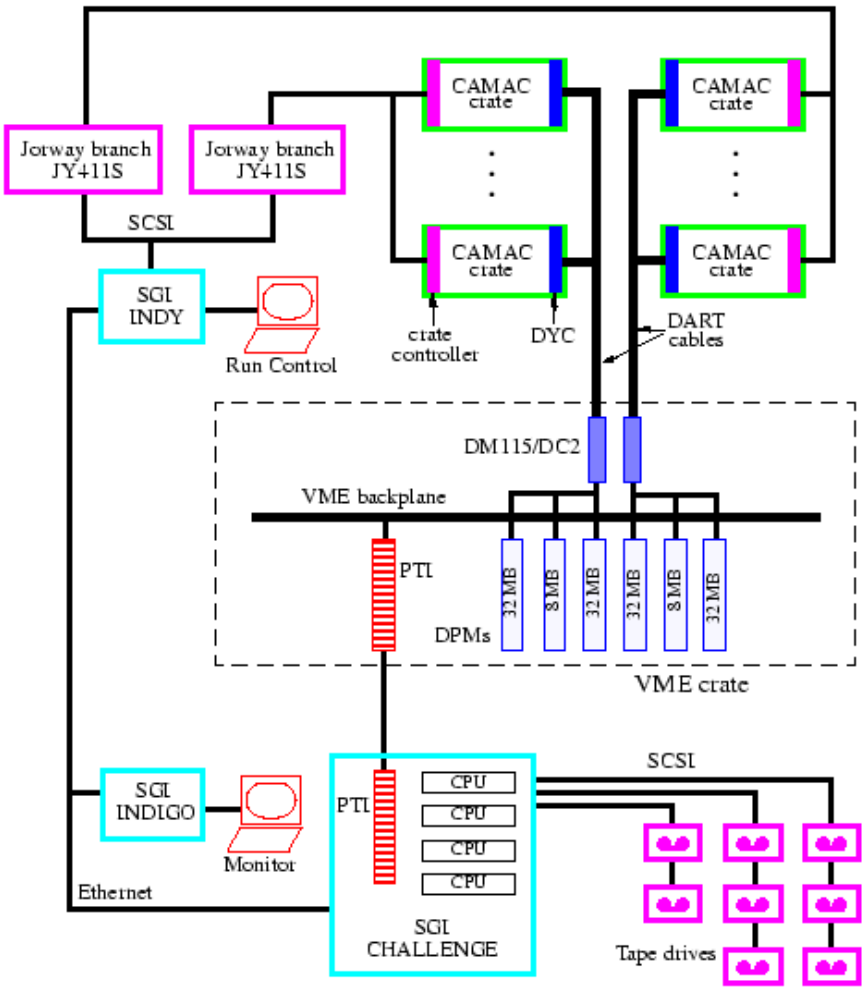

Figure 3.18: E835 data acquisition system layout.

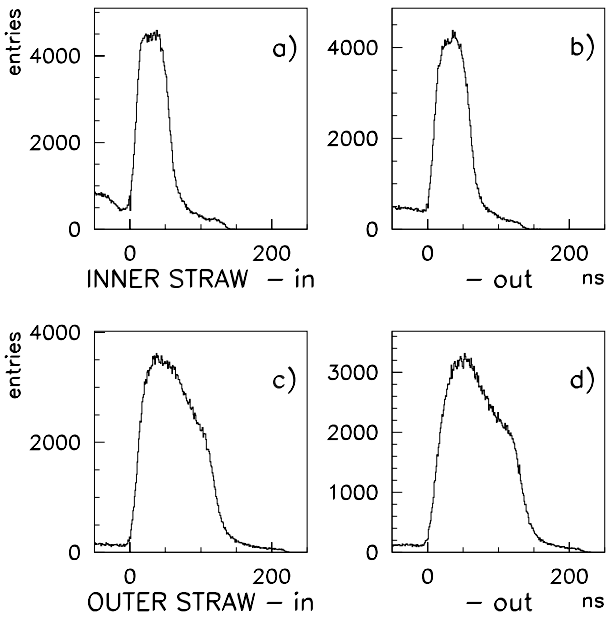

Figure 3.19: Drift time distribution for the four layers of straw chambers. Smaller drift time is obtained for particles crossing the straw close to the wire.

Straws

A charged particle passing into one of the two straw chambers ionizes the gas, then the electrons drift to the wire. For each tube the drift time is measured as the delay between the straw signal and the event time (defined by the strobe signal built with CCAL). The time distribution for the four layers is shown in Figure 3.19. From the drift time measurement a precise determination of the distance between the crossing point and the wire can be obtained. The left-right ambiguity can be solved using the information from the two staggered layers of each detector.

Fibers

A fiber cluster is defined as the group of adjacent hit fibers at the event time. When a charged particle crosses a scintillating fiber layer at small angle, it can cross more than one fiber. The light yield of each fiber is proportional to the length of the particle path inside the fiber. The coordinate of the cluster is calculated by weighting all the fiber coordinates z_i with the energy deposits in the fibers Q_i:

$$z_{cl} = \frac{\sum_i Q_i z_i}{\sum_i Q_i}.$$

If a cluster is composed of 2 or more fibers, it is splitted if there is a decrease and an increase in its fiber ADC signal pattern.

Calorimeters

The CCAL cluster contains information about angles and energy deposition. The clusterizer works in the following way:

- identification of the cluster seed. It is defined as the block with more energy than the 8 blocks around it. Depending on the analysis to be performed, the cluster seed has an energy deposition threshold (called seed threshold); also the cluster has a minimum energy deposition value (called cluster threshold);
- a 3×3 bloks grid around the seed form a cluster;
- if two clusters overlap, the energy deposition of the overlapping blocks is shared between the two clusters according with fractions f_i calculated depending on position and energy of both clusters.

The cluster energy is obtained summing over all the energies of the blocks. The position (x, y) is obtained by:

$$x = \frac{\sum_{i=1}^{9} f_i E_i x_i}{\sum_{i=1}^{9} x_i},$$

$$y = \frac{\sum_{i=1}^{9} f_i E_i y_i}{\sum_{i=1}^{9} y_i},$$

where x_i and y_i are the positions of the center of the blocks.

The position and energy of the clusters are corrected for the energy loss in the steel partitions supporting the blocks (cracks), which are the 2% of the surface area in ϕ and the 0.5% in θ.

When two photons from a π_0 decay hit adjacent blocks, only one cluster is found instead of two. To look for such events, the cluster mass, defined as:

$$M_{cl} = \sqrt{\left(\sum_i E_i\right)^2 - \left(\sum_i \vec{p}_i\right)^2},$$

can be calculated, where the sum is made over a 5×5 grid around the seed and $\vec{p}_i = E_i \vec{r}_i$ with $\vec{r}_i$ the unit vector pointing to the center of the block. Any cluster with $M_{cl} > 120$MeV is splitted into two clusters by identifying a second cluster center.

The time information for calorimeter clusters is essential for the rejection of spurious clusters, due to background events overlapping to the triggered event. Each

calorimeter block is connected to an ADC and a TDC (through a discriminator). The time of the hit is measured with respect to the event time. Then for pulses of different height the measured time is corrected for the slewing, or the fact that different size pulses will cross the discriminator threshold at different times. Since a cluster can have up to 9 blocks, only the times of the two counters with the highest ADC values are considered for the timing classification of the clusters: if neither block has any TDC information the cluster is labeled "undetermined", if one of the two blocks has a time within 10 ns of the event time the cluster is labeled "in-time", otherwise it is labeled "out-of-time". The timing information is present on almost all the clusters with energy above 75 MeV, below this value the fraction of events with timing informations decrease becoming 0 for energy values around 20 MeV [62].

3.6.2 Charged track definition

All the inner tracking detector cluster informations are used for the detection of charged tracks.

Straws and hodoscopes

The measurement of a charged ϕ line is made using straw chambers and hodoscopes. A ϕ line is required to have at least two straw layer hits, in coincidence with at least two hodoscope hits. The azimuthal angle measurement and the associated error are obtained with a linear fit of all the straw clusters positions. The resolution on a single track is $\sim$ 8mrad (constant over all ϕ and θ ranges).

Fibers

The reconstruction of a θ line is performed using the scintillating fiber tracker. To open a θ line, at least one cluster in both inner and outer detectors is required to exist and overlap within a given θ cut (using the interaction vertex position). Then the θ measurement is obtained by fitting all the clusters positions with a straight line. The intrinsic angular resolution varies with θ and ranges from $\sim$ 1 mrad at small θ (around 15°) to $\sim$ 4 mrad at large θ (around 55°).

Sometimes multiple scattering effect is higher than the intrinsic θ resolution. When using kinematic fits, the error on the θ measurement should be corrected to take into account this effect, depending on the kind of particle, as discussed in Appendix A.

3.6.3 Track reconstruction

Once θ and ϕ lines are formed they need to be associated in order to obtain the direction of the particles. The only detector usable for this purpose is CCAL. This

association defines a charged track. All the CCAL clusters that cannot be associated to inner tracking lines are defined as neutral tracks (γ).

3.6.4 Event classification

For $e^{\pm}$ and γ tracks we can measure angle and energy. High energy $e^{\pm}$ can also be easily identified by using the Čerenkov counters (see Appendix C). For other kind of particles that could be present in the channels analyzed by E835, like $\pi^{\pm}$ or $K^{\pm}$, only the direction can be measured. The information on the kind of hadron can not be obtained directly from the detector. For this reason, all the final states need to be completely reconstructed by means of kinematic fits.

3.7 Simulations

Two different simulation programs have been developed and used for data analysis. The first one is based on the standard package GEANT 3[63]; the second one is a parametric description of the CCAL response which has been preferred to GEANT because of the smaller amount of CPU time required. This second simulation has been extensively used in the neutral channels analysis and will not be used for this thesis. The GEANT simulation is built in a standard way, for this reason it will not be described in detail here.

Chapter 4

Analysis

The following analysis is based on an integrated luminosity $L_I = 14.4$ pb^{-1} of data in the ψ' energy region, 12.5 pb^{-1} taken on the resonance and 1.9 pb^{-1} on the background, yielding an amount of $\sim$ 30000 e^+e^- pairs from charmonium decay. The channels analyzed in this thesis are the ones presenting a high invariant mass e^+e^- pair due to charmonium decay in the final state, i.e. $\psi' \to e^+e^-$ and $\psi' \to J/\psi X$, with the J/ψ subsequently decaying into e^+e^- . The identification of these events is easily done by looking at the invariant mass of the two e^+e^- candidates and using the electron weight (see Appendix C). Then the full event reconstruction can be performed for those events having also all the other final state particles within the detector acceptance.

4.1 Data sample

During the year 2000, the second period of data taking of the experiment, E835 collected about 110 pb^{-1} of data for the study of the charmonium resonances, mainly for the study of the χ_{c0}, the confirmation of the h_c and the study of the ψ' .

The whole E835-II ψ' data sample is summarized in Table 4.1. As was mentioned in Chapter 3, after the accumulation of a desired quantity of antiprotons in the antiproton accumulator, the interactions with the hydrogen target can occur until the beam is completely used. The amount of data collected in this way is called "stack". During the stack the energy of the $\bar{p}$ beam can be changed to take data at several E_{CM} so the data are organized in "runs", data samples with $L_I \simeq 250$ nb^{-1}, with a constant nominal beam energy and roughly constant running conditions.

Some important comments to Table 4.1:

- stacks 54a and 54c are not in the ψ' resonance energy region. They are used for the evaluation of the background;
- during stack 29 a special "one electron" trigger has been used to evaluate the trigger efficiency;

Stack	Runs	Date	Energy (MeV)	L_I (pb^{-1})
1	5006 - 5038	27 Jan 00	ψ' scan	0.7478
2	5076 - 5084	31 Jan 00	3686.1	1.0082
14	5571 - 5574	30 Apr 00	3686.0	0.9919
29	5818 - 5837	14 Jun 00	ψ' scan	0.9918
30	5840 - 5842	16 Jun 00	3687.7 - 3686.0	0.3962
49	7143 - 7148	26 Aug 00	3686.1	2.5664
50	7248 - 7252	09 Oct 00	3686.1	1.2750
51	7254 - 7259	15 Oct 00	3686.1	2.1033
54a	7269 - 7271	06 Nov 00	3704.9	1.1532
54b	7273 - 7278	07 Nov 00	3686.1	2.4009
54c	7280 - 7283	09 Nov 00	3666.1	0.7795

Table 4.1: E835-II ψ' data sample.

- in stack 51 the VLPC (used for the scintillating fibers detector readout) temperature was not stable for runs 7257 to 7259, this can affect the fiber detector efficiency. The problem is discussed in Appendix B.

4.2 General description of the analysis

The channels studied in this thesis are[1]:

- $\psi' \to e^+e^-$;
- $\psi' \to J/\psi X \to e^+e^- X$;
- $\psi' \to J/\psi\pi^+\pi^- \to e^+e^-\pi^+\pi^-$;
- $\psi' \to J/\psi\pi^0\pi^0 \to e^+e^-4\gamma$;
- $\psi' \to J/\psi\eta \to e^+e^-2\gamma$;

the η is identified only through its $\gamma\gamma$ decay mode ($\mathcal{B}(\eta \to \gamma\gamma) = 39.43 \pm 0.26\%$). All the above decays are characterized by a high invariant mass e^+e^- coming from ψ' or J/ψ decay. The selection is therefore based on the identification of the events with a high invariant mass e^+e^- pair; within this sample we will look for all the above mentioned channels.

The selection procedure can be subdivided in the following steps.

[1]The $\psi' \to J/\psi\pi^0$ channel will not be considered because its tiny branching ratio makes the extraction of the signal from the background very difficult.

a. The events passing the e^+e^- hardware trigger (see Section 3.4) are written on tape and sent to the software filter (2^{nd} level trigger) for a further selection. The filter unpacks the CCAL hits and selects the events having at least two on-time clusters with invariant mass greater than 2.0 GeV (named "goldee"). The goldee data are written to disk for a fast analysis.

b. The goldee sample is then sent to a software filter, called "mini-dst" (mdst), that selects events having invariant mass for the e^+e^- candidates $m_{ee} > 2.6$ GeV, calculated with the measured 4-momentum of all the on-time CCAL clusters pair. Another requirement is that each $e^\pm$ candidate must have at least 2 out of 3 hodoscopes and a Čerenkov hit associated.

c. For those events with the e^+e^- candidates in the detector fiducial region, $15° < \theta_{e^\pm} < 60°$, the selection of e^+e^- coming from charmonium decay is done by cutting on the products of the electron weights (EW) of the two tracks. The cut chosen:

$$EW_1 \cdot EW_2 > 1.5, \tag{4.1}$$

has high efficiency and good background rejection. It is discussed in more detail in Appendix C.

d. For the reconstruction of the exclusive channels all the final state particles are required to be within the detector acceptance: $12° < \theta_\gamma < 68°$ for the photons and $15° < \theta_{\pi^\pm} < 55°$ for the charged pions.

e. Once all candidates for the reconstruction of a specific channel are identified, the hypothesis is tested with a kinematic fit, cutting on the χ^2 probability (called "prob($chan$)" in the following).

The kinematic fit constraints are the 4-momentum conservation and the mass of intermediate resonances, like $J/\psi \to e^+e^-$ or $\pi^0,\ \eta \to \gamma\gamma$, namely:

$$\sum_{i=1}^{N} p_{x,i} = 0; \tag{4.2}$$

$$\sum_{i=1}^{N} p_{y,i} = 0; \tag{4.3}$$

$$\sum_{i=1}^{N} p_{z,i} = p_{lab}; \tag{4.4}$$

$$\sum_{i=1}^{N} E_i = E_{lab}; \tag{4.5}$$

$$(E_i + E_j)^2 - (\vec{p}_i + \vec{p}_j)^2 = M_R^2; \tag{4.6}$$

where N is the number of particles detected, E_{lab} and p_{lab} the $\bar{p}p$ total energy and momentum in the laboratory and the four-momentum of the i^{th} particle is $p_i = (E_i, \vec{p}_i)$. When the decay proceeds through intermediate resonances, the invariant mass of the daughter particles i and j is constrained to be M_R. Only in the case of the inclusive J/ψ selection, where it is not required the detection of all the particles in the final state, it is not possible to use the constraints on the conservation of the total four-momentum. The total number of constraints of the kinematic fit is obtained subtracting the number of unmeasured variables from the total number of constraints.

Data for all the analyzed channels are taken at the same time. This makes it possible to cancel many sources of systematic error in the evaluation of ratios of BR for different channels, as will be explained in Chapter 5.

4.3 Events selection

From the mdst sample, a total of 32862 events with an e^+e^- pair from charmonium decay are selected with the cuts:

- $EW_1 \cdot EW_2 > 1.5$;
- $15° < \theta_{e^\pm} < 60°$;

applied to the e^+e^- candidates tracks. In the following the event sample obtained with these two cuts will be called "ee_{tot}". Their invariant mass distribution m_{ee} is shown in Figure 4.1, where the two peaks due to J/ψ and ψ' decay can be clearly distinguished; nevertheless, from the overlapping of the two tails in the region around 3.35 GeV, it is also evident the possibility of contamination between the two $\psi' \to e^+e^-$ and $J/\psi \to e^+e^-$ samples. Therefore the two subsamples can not be completely separated just cutting on m_{ee}.

The same selection applied to the background data (stacks 54a and 54c) yield a total of 66 events. Their invariant mass distribution is also shown in Figure 4.2.

The angular and energy distributions of all the e^+e^- pair are shown in Figure 4.3.

4.3.1 $\psi' \to e^+e^-$

For $\psi' \to e^+e^-$ event selection from the ee_{tot} sample, the following cuts are applied:

- $\text{prob}(e^+e^-) > 10^{-4}$;
- $\text{prob}(e^+e^-) > \text{prob}(J/\psi X)$.

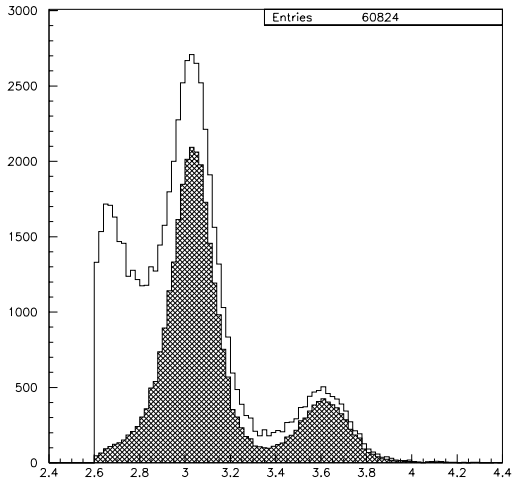

Figure 4.1: m_{ee} distribution for all e^+e^- candidates in the mdst sample (open) and for events with the e^+e^- in the detector fiducial region ($15° < \theta_{e^\pm} < 60°$) with $EW_1 \cdot EW_2 > 1.5$ (cross hatched).

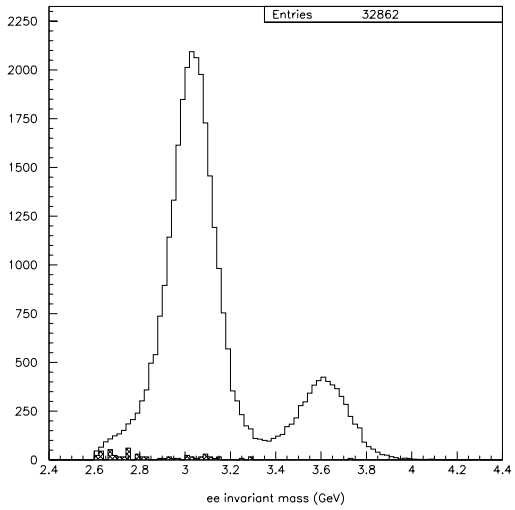

Figure 4.2: m_{ee} distribution for all events with both e^+e^- candidates in the fiducial region ($15° < \theta_{e^\pm} < 60°$), after the $EW_1 \cdot EW_2 > 1.5$ cut. The cross hatched area are the backgound events, obtained from stacks 54a and 54c, scaled with the luminosity.

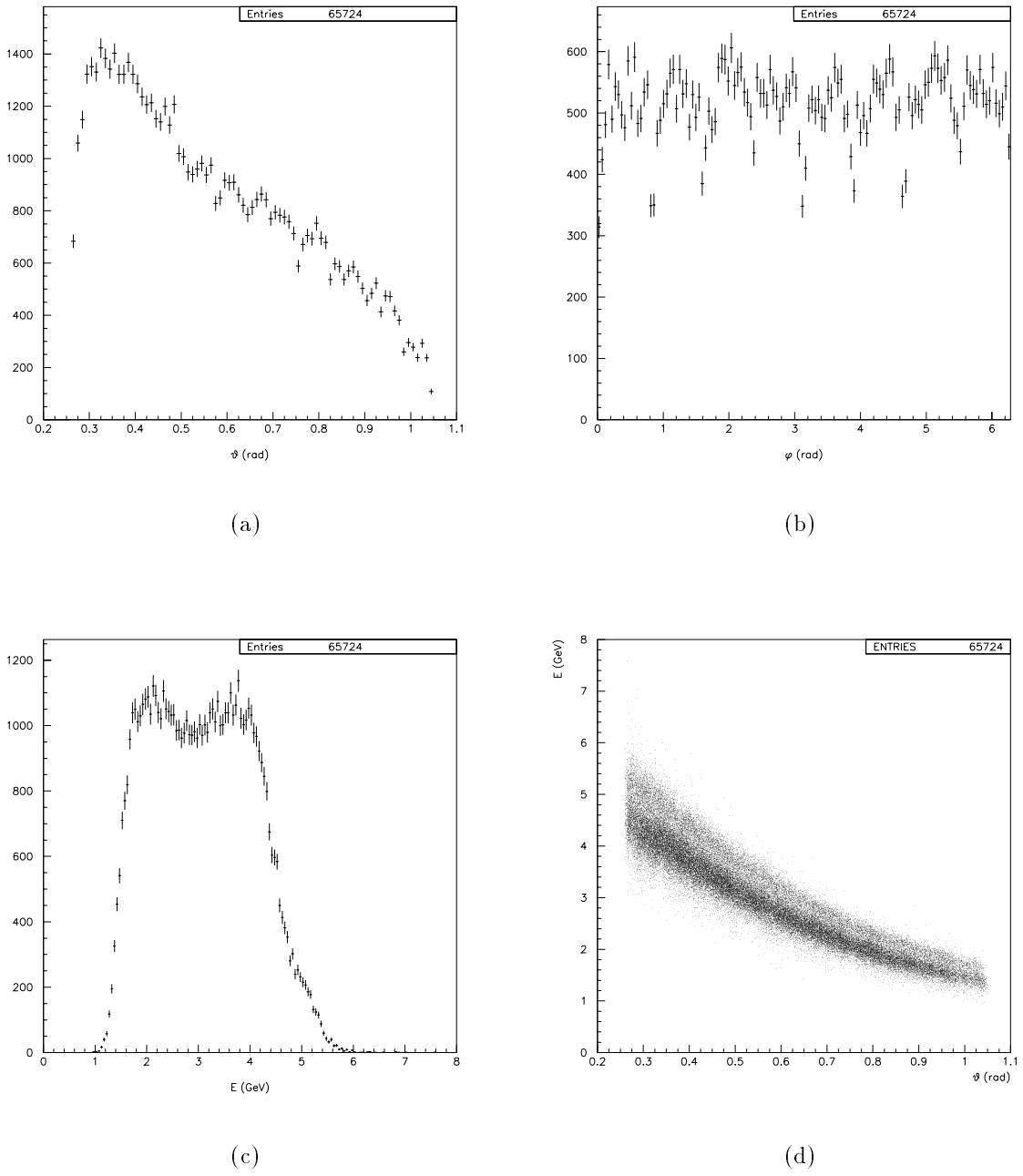

Figure 4.3: (a) $\theta_{e^\pm}$, (b) $\phi_{e^\pm}$, (c) $E_{e^\pm}$ and (d) its $\theta_{e^\pm}$ dependence distributions for all e^+e^- candidates in acceptance (2 entries per event). The 8 regions slightly depleted in (b) correspond to the cracks between the H1 elements, causing (e^+e^-) trigger inefficiency.

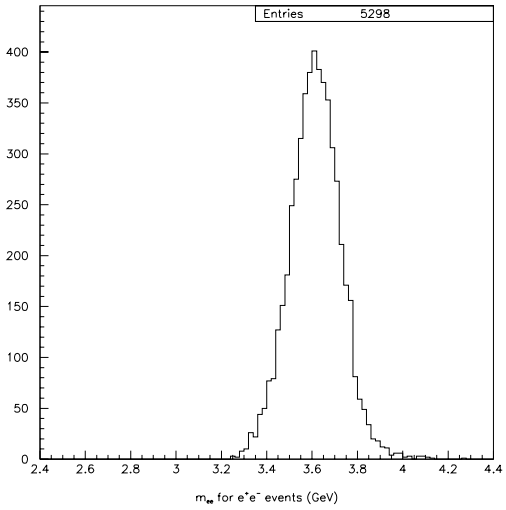

Figure 4.4: m_{ee} distribution for $\psi' \to e^+e^-$ events.

The identification of the event is based on the 4 constraints (4-C) kinematic fit probability cut. All the events are tested with both the hypothesis $\psi' \to e^+e^-$ and $\psi' \to J/\psi X \to e^+e^-X$ and the most probable one is chosen.

The number of e^+e^- exclusive events selected on the whole sample is 5298. Figure 4.4 shows the m_{ee} distribution for such events.

4.3.2 $\psi' \to J/\psi X \to e^+e^-X$

For the selection of $J/\psi X$ final state the presence of an e^+e^- pair with the J/ψ invariant mass is required. This is the only constraint of the kinematic fit. The cuts applied for the selection are:

- prob$(J/\psi X) > 10^{-4}$;
- prob$(J/\psi X) >$ prob(e^+e^-).

Figure 4.5 shows the m_{ee} distribution for the 26805 selected events.

4.3.3 $\psi' \to J/\psi\pi^0\pi^0 \to e^+e^-4\gamma$

For all the events of the ee_{tot} sample presenting at least 4 additional clusters in CCAL we checked the possibility of the reconstruction of a $J/\psi\pi^0\pi^0$. All the additional CCAL clusters are paired, trying all the possibilities, to check for the presence of π^0 candidates with a measured invariant mass 50 MeV $< m_{\pi^0} <$ 350 MeV; if two such candidates are found, the $J/\psi\pi^0\pi^0$ hypothesis is tested with a kinematic fit. If

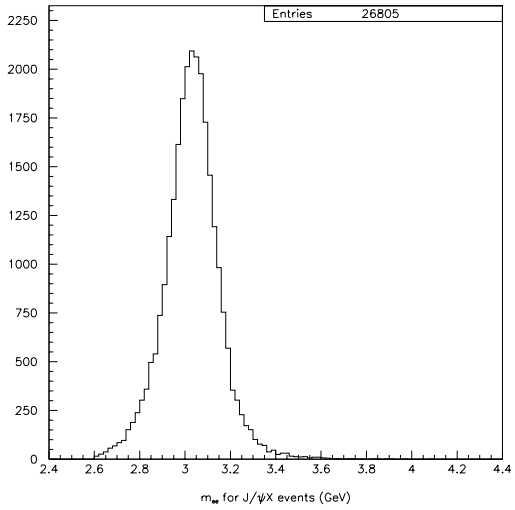

Figure 4.5: m_{ee} distribution for $\psi' \to J/\psi X$ events.

more than one combination passes the kinematic fit selection the one with highest prob(χ^2) is chosen. No cut on the number of extra clusters in CCAL have been applied, as explained in more detail Appendix D.

The cuts applied for the event selection are:

- $15° < \theta_\gamma < 68°$;
- prob($J/\psi\pi^0\pi^0$) $> 10^{-4}$;
- prob($J/\psi\pi^0\pi^0$) $>$ prob(*other channels*);
- opening angle between $e^\pm$ and γ: $\omega_{e\gamma} > 100$ mrad.

The kinematic fit in this case is 7-C. Photon clusters in CCAL in the nearby of $e^\pm$ clusters will modify the $e^\pm$ cluster shape and lower the EW efficiency, as explained in more detail in Appendix C. The last of the above mentioned cut is applied to use for $J/\psi\pi^0\pi^0$ events the same EW efficiency calculated with a sample of e^+e^- exclusive events.

E_γ of low energy photons is not well measured by the calorimeter. A prescription is used in this case: the value assigned to the error on the energy measurement for all the photons with E_γ less than 300 MeV is $\sigma_E = 25\% E_\gamma$ if the σ_E associated to the energy measurement is smaller[2]. This applies to both the $J/\psi\pi^0\pi^0$ and $J/\psi\eta$ analysis.

[2]The error on the cluster energy measurement takes into account the crack correction and is calculated with:

$$\sigma_E = 0.05\sqrt{E} + 0.3(f_{corr} - 1)E + 0.005,$$

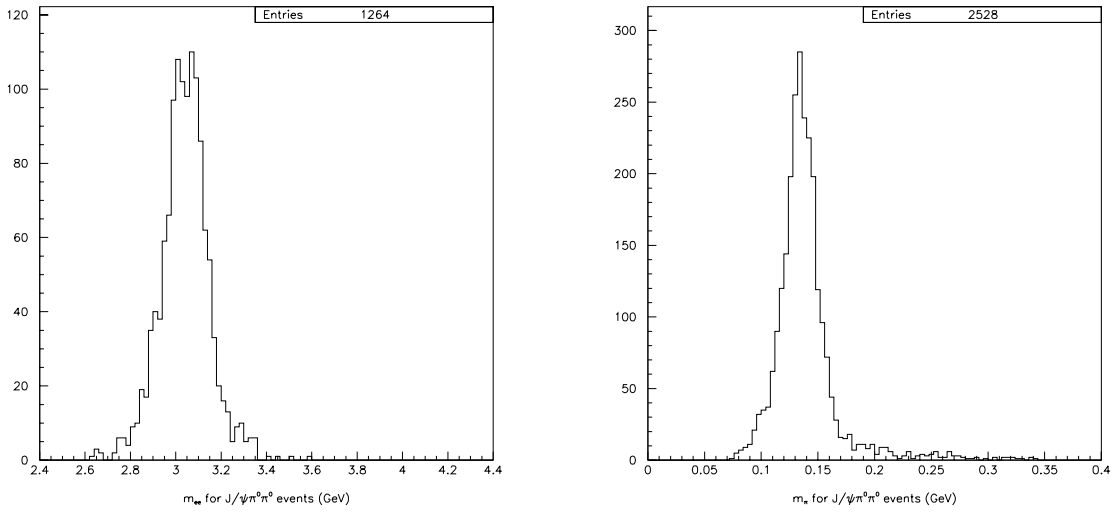

(a) (b)

Figure 4.6: (a) m_{ee} and (b) m_{π^0} distributions for $\psi' \to J/\psi\pi^0\pi^0$ events ((b) has 2 entries per event).

The number of $J/\psi\pi^0\pi^0$ events selected on the whole sample is 1264. Figure 4.6 shows the observed m_{ee} and m_{π^0} distribution for such events.

The observed invariant mass distribution for the dipion (after the kinematic fit) is shown in Figure 4.7.

4.3.4 $\psi' \to J/\psi\eta \to e^+e^-2\gamma$

The $J/\psi\eta$ event selection is similar to the one for $J/\psi\pi^0\pi^0$. The η is detected only through its $\gamma\gamma$ decay so the η candidates are defined as a pair of CCAL clusters with invariant mass 300 MeV $< m_\eta <$ 800 MeV and are searched among all the pair of additional CCAL clusters in the ee_{tot} sample. If more than two additional CCAL clusters are present all the possible combination are checked. The $J/\psi\eta$ hypothesis is then tested with a kinematic fit.

The cuts applied are:

- $15° < \theta_\gamma < 68°$;
- prob$(J/\psi\eta) > 10^{-2}$;
- prob$(J/\psi\eta) >$ prob$(other\ channels)$;

where E is the energy after crack correction $E = f_{corr}E_{meas}$. All the details can be found in [62].

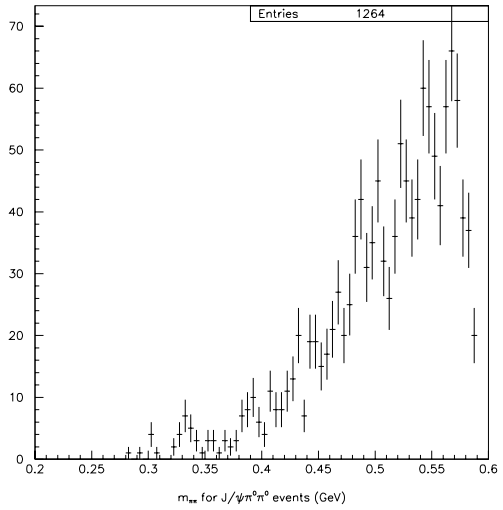

Figure 4.7: $m_{\pi\pi}$ distribution for $\psi' \to J/\psi\pi^0\pi^0$ events.

- opening angle between $e^{\pm}$ and γ: $\omega_{e\gamma} > 100$ mrad.

Differently from all the other channels, for the $J/\psi\eta$ selection the cut on the kinematic fit probability is set at 10^{-2} to decrease the possibility of contamination from internal background due to $J/\psi\pi^0\pi^0$. The kinematic fit is 6-C in this case.

The number of $J/\psi\eta$ events selected on the whole sample is 387. Figure 4.8 shows the observed m_{ee} and m_{η} distributions.

4.3.5 $\psi' \to J/\psi\pi^+\pi^- \to e^+e^-\pi^+\pi^-$

The $J/\psi\pi^+\pi^-$ channel needs a slightly different treatment with respect to the previous selected final states, because of the following considerations:

- the energy of the $\pi^{\pm}$ candidates can not be measured;
- the $\pi^{\pm}$ can not be detected by using CCAL only: the directions of the $\pi^{\pm}$ need to be determined by using the inner tracking system;
- there is no particle ID system in the E835 detector for the identification of $\pi^{\pm}$ tracks. Once identified the $\pi^+\pi^-$ candidates, this hypothesis need to be tested using a kinematic fit.

Differently from E835-I, an improved tracking system allows a kinematic fit selection of the $J/\psi\pi^+\pi^-$ channel. This is the only analysis in this thesis in which the tracking plays a fundamental role, then it is worthwhile to consider it in some detail.

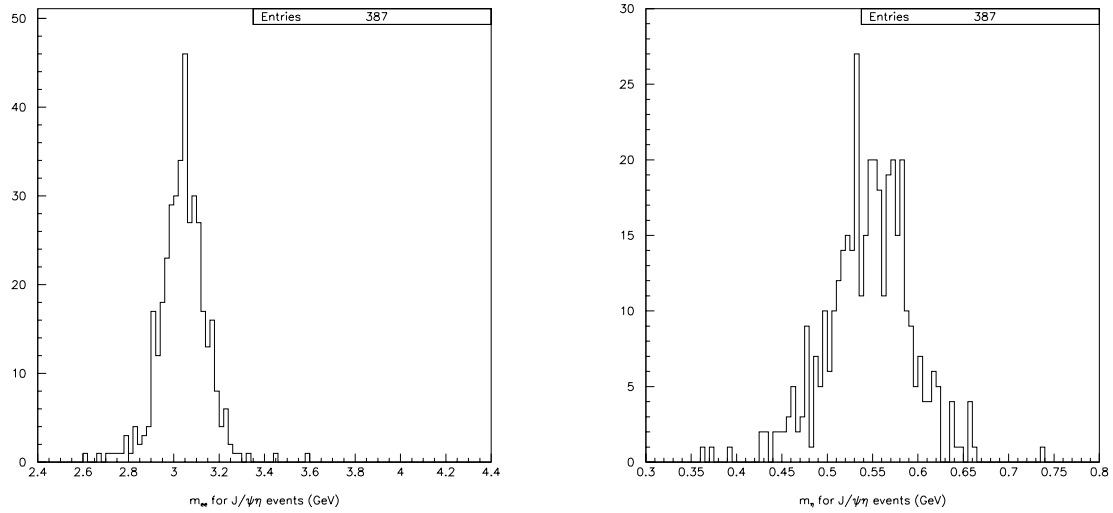

(a) (b)

Figure 4.8: (a) m_{ee} and (b) m_η distributions for $\psi' \to J/\psi\eta$ events.

For the events selection it is not possible to cut on the number of θ and ϕ lines, because of the possibility of additional charged lines due to δ rays or pile-up or spurious hits in fibers and straws that could lead to non physical charged lines.

In order to form a charged track, θ and ϕ lines must be associated. This is usually done using CCAL clusters. For the $\pi^\pm$, the association of θ and ϕ measurements is done using a different procedure. Each possible $\theta - \phi$ combination is used as a $\pi^\pm$ candidate, even if no CCAL cluster is present for the association[3]. The $J/\psi\pi^+\pi^-$ hypothesis is tested with a 3-C kinematic fit for the e^+e^- tracks with all the possible pairs of combinations of θ and ϕ lines detected separately from the fiber and straw detectors. Then the most probable one is chosen. In this way the additional inefficiency due to pion decay in the region between the tracking and CCAL is eliminated.

The intrisic resolution of the scintillating fiber detector is of the order of 1 mrad or better, especially at low θ. In this case, especially for slow particles, the error on the θ measurement is dominated by the multiple scattering. The error σ_θ to be used in the kinematic fit has been assigned to charged tracks as explained in Appendix A. Since in E835 detector it is not possible to measure the charged pion energy, these variables can not be used as a input for the kinematic fit.

[3] This system presents an advantage also from the point of view of the GEANT simulation of $J/\psi\pi^+\pi^-$ events: the reproduction of the energy deposition in CCAL by hadronic showers can be neglected.

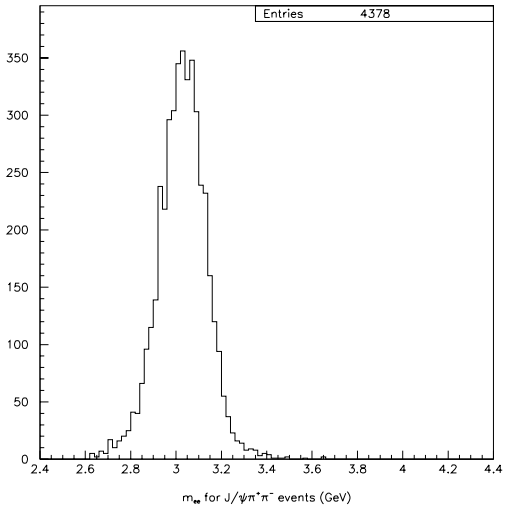

Figure 4.9: m_{ee} distribution for $\psi' \to J/\psi\pi^+\pi^-$ events.

The final event selection is:

- $15° < \theta_{\pi^\pm} < 55°$;
- $\text{prob}(J/\psi\pi^+\pi^-) > 10^{-4}$;
- $\text{prob}(J/\psi\pi^+\pi^-) > \text{prob}(other\ channels)$.
- $p^2_{J/\psi,CMS} - K^2 < 0.01$;

where $p_{J/\psi,CMS}$ and K are the J/ψ and dipion momentum in CM frame, calculated with the output variables of the kinematic fit. This cut is done to avoid convergence of the kinematical fit to non physical states.

The number of $J/\psi\pi^+\pi^-$ events selected on the whole sample is 4378. Figure 4.9 shows the m_{ee} distribution for such events. The measured invariant mass distribution for the dipion (after the kinematic fit) is shown in Figure 4.10.

4.3.6 Stability of the ratios of events

The stability of the selection has been checked looking at the number of events belonging to each channel with respect to the total number of events in the ee_{tot} sample for all the stacks. The number of events in each stack is summarized in Table 4.2 and the ratios of number of events in each channel with the number of ee_{tot} for each stack in Table 4.3.

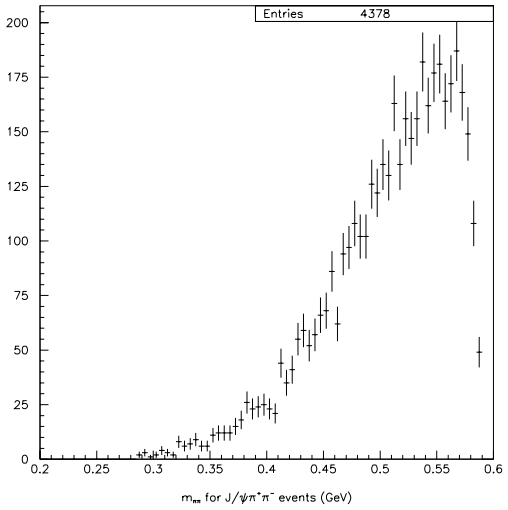

Figure 4.10: $m_{\pi\pi}$ distribution for $\psi' \to J/\psi\pi^+\pi^-$ events.

The total ratios are well reproduced, within the errors, for each stack. The few exception can not be explained looking at the hardware history, for this reason they are mainly considered statistical fluctuations.

Only in stack 50, for the $J/\psi\pi^+\pi^-$ channel there is a fluctuation larger than 4σ, which is very unlikely to happen. Since the ratios of all the other channels are stable, this would suggest the presence of problems in the charged tracking. During this stack, the element number 22 of H2$'$ was disconnected, anyway this effect, evaluated with the Monte Carlo as explained in Section 5.1.5, do not explain completely the loss of efficiency. Since no other hardware explanation is found for the hypothesis of low detector efficiency, we decided to not reject the sample.

4.4 Monte Carlo

In this analysis the Monte Carlo (MC) is used in two ways. For the measurement of the acceptances and the observation of their dependence on the angular and invariant mass distribution parameters, only the kinematics of the reaction is simulated. The full reconstruction of the event in the E835 detector, used for all the other purposes, is based on GEANT 3[63].

A set of data have been produced for each analyzed channel, with the following features:

- the e^+e^- angular distribution in the center of mass system for $\psi' \to e^+e^-$ is $1+\lambda_{\psi'}\cos^2\theta^*_e$. The value $\lambda_{\psi'} = 0.69\pm0.26$, that is used in the event generation, come from the E760 measurement [16];

Stack	e^+e^-	$J/\psi X$	$J/\psi\pi^+\pi^-$	$J/\psi\pi^0\pi^0$	$J/\psi\eta$
1	159	684	122	21	13
2	655	3027	535	136	46
14	403	1903	338	105	29
29	322	1797	290	87	19
30	163	792	139	30	9
49	965	5137	821	246	70
50	623	3127	408	160	44
51	849	4323	700	207	68
54b	1159	6015	1025	272	89
TOT	5298	26805	4378	1264	387

Table 4.2: Number of events divided by stack.

Stack	e^+e^-	$J/\psi X$	$J/\psi\pi^+\pi^-$	$J/\psi\pi^0\pi^0$	$J/\psi\eta$
1	0.184 ± 0.013	0.794 ± 0.014	0.142 ± 0.012	0.024 ± 0.005	0.015 ± 0.004
2	0.175 ± 0.006	0.807 ± 0.006	0.143 ± 0.006	0.036 ± 0.003	0.012 ± 0.002
14	0.171 ± 0.008	0.807 ± 0.008	0.143 ± 0.007	0.045 ± 0.004	0.012 ± 0.002
29	0.147 ± 0.008	0.819 ± 0.008	0.132 ± 0.007	0.040 ± 0.004	0.009 ± 0.002
30	0.166 ± 0.012	0.807 ± 0.013	0.142 ± 0.011	0.031 ± 0.005	0.009 ± 0.003
49	0.155 ± 0.005	0.824 ± 0.005	0.132 ± 0.004	0.039 ± 0.002	0.011 ± 0.001
50	0.163 ± 0.006	0.818 ± 0.006	0.107 ± 0.005	0.042 ± 0.003	0.012 ± 0.002
51	0.160 ± 0.005	0.816 ± 0.005	0.132 ± 0.005	0.039 ± 0.003	0.013 ± 0.002
54b	0.158 ± 0.004	0.818 ± 0.004	0.139 ± 0.004	0.037 ± 0.002	0.012 ± 0.001
TOT	0.161 ± 0.002	0.816 ± 0.002	0.133 ± 0.002	0.038 ± 0.001	0.012 ± 0.001

Table 4.3: Ratios of $N(channel)/N(ee_{tot})$ for each stack.

- $J/\psi\pi\pi$ events are produced with a S wave between the J/ψ and the $(\pi\pi)$ and also among the two π in the dipion center of mass frame;
- in $J/\psi\pi\pi$ events, the J/ψ is supposed to mantain the ψ' helicity, so its subsequent decay to e^+e^- presents the same angular distribution $1 + \lambda_{\psi'} \cos^2\theta_e^*$;
- for $J/\psi\pi\pi$, the dipion mass is generated according to (2.28) with $\lambda_{\pi\pi} = 4$;
- for $J/\psi\eta$ events the e^+e^- angular distribution used is the one discussed in Section 1.2: $(5\lambda_{\psi'} + 4) - 4\lambda_{\psi'} \cos^2\theta_e^*$.

The event vertex is randomly chosen in the interaction region according to the measured vertex distribution.

Stack	Runs	Date	Energy (MeV)	L_I (pb^{-1})
45a	7098 - 7103	12 Aug 00	3809.9	0.4866
45b	7105 - 7107	13 Aug 00	3800.0	0.9551
45c	7109	13 Aug 00	3798.1	0.5125
46	7114 - 7118	17 Aug 00	3769.9	2.1772
48	7138 - 7139	24 Aug 00	3836.1	1.0337
52	7261 - 7263	22 Oct 00	4267.3	0.8485
53	7265 - 7267	31 Oct 00	4267.5	1.2508

Table 4.4: High energy data sample taken from E835-II.

The electromagnetic showers in the calorimeters are tuned with data to reproduce the observed e^+e^- invariant mass distribution as well as the π^0 and η observed mass distribution. The dead or noisy calorimeter channels are taken into account into the simulation.

Also the dead channels in the scintillating fiber tracker are different for each stack: this is reproduced by the simulation and affects the efficiency for the selection of $J/\psi\pi^+\pi^-$ final state.

Some plots regarding the comparison between data and MC are collected in Appendix E.

4.5 Backgrounds and contaminations

Two sources of background contribute to the measured cross section for the resonance: the non resonant background, due to events not related to ψ' formation (i.e. final states with a J/ψ produced directly in $\bar{p}p$ annihilation, not coming from the resonance decay) and the background due to event misidentification.

To evaluate the non resonant background we have used the two data samples of stack 54a and 54c (see Table 4.1).

Also the data on high energy points collected in the 2000 run can be used to check the consistency of the background level at the ψ' . The available data are summarized in Table 4.4. Figure 4.11 show the behavior of the continuum contamination for $\overline{p}p \to J/\psi X,\ J/\psi\pi^+\pi^-$ obtained with a linear fit of all the available background data.

The background measurements made in these two ways (stacks 54a, 54c and high energy points) are compatible and have similar errors. In the following, the background level will be determined as the average of the two background points of stack 54[4]. The number of background events and the level of continuum background

[4]For the high energy points, small contributions to the total number of events coming from

Stack	e^+e^-	$J/\psi X$	$J/\psi\pi^+\pi^-$	$J/\psi\pi^0\pi^0$	$J/\psi\eta$
54a	1	36	1	1	0
54b	0	19	1	0	0
45a	0	22	0	0	0
45b	0	57	8	1	0
45c	1	21	5	0	0
46	0	80	4	1	1
48	0	35	6	1	0
52	0	45	5	0	0
53	0	77	10	2	0
$\frac{N_{bkg}}{L_I}$ (pb)	$0.5^{+1.2}_{-0.4}$	28 ± 4	$1.2^{+1.6}_{-0.8}$	$0.5^{+1.2}_{-0.4}$	< 0.9 (68% C.L.)

Table 4.5: Number of background events. N_{bkg}/L_I is obtained as the average of stacks 54a and 54c. In stack 54a the straws were off for $\sim 60\%$ of run 7270, that means about 260 nb^{-1} of integrated luminosity. In this period the $J/\psi\pi^+\pi^-$ could not be detected so the background for this channel is calculated for an integrated luminosity of 1.7 pb^{-1}.

are summarized in Table 4.5.

The background level from misidentified events can be evaluated using GEANT. A sample of 50000 events for each considered final state has been generated and analyzed to evaluate the number misidentified events.

Table 4.6 summarizes the misidentification level for the analyzed channels. The main sources of misidentification are:

- e^+e^- events tagged as $J/\psi X$. This is because $e^\pm$ from exclusive ψ' decay can lose part of their energy in a passive material (the CCAL cracks or the Čerenkov septum, for example) or by bremsstrahlung. The reconstructed invariant mass in this case turns out to be lower than the real one;

- $J/\psi\pi^0\pi^0$ tagged as $J/\psi\eta$. When one of the four photons escape the detector acceptance, the event can not be tagged as $J/\psi\pi^0\pi^0$ and there is the possibility that it is identified as $J/\psi\eta$, even if the kinematic fit probability is more likely to be distributed around small values.

charmonium states with mass above the open charm threshold can not be excluded.

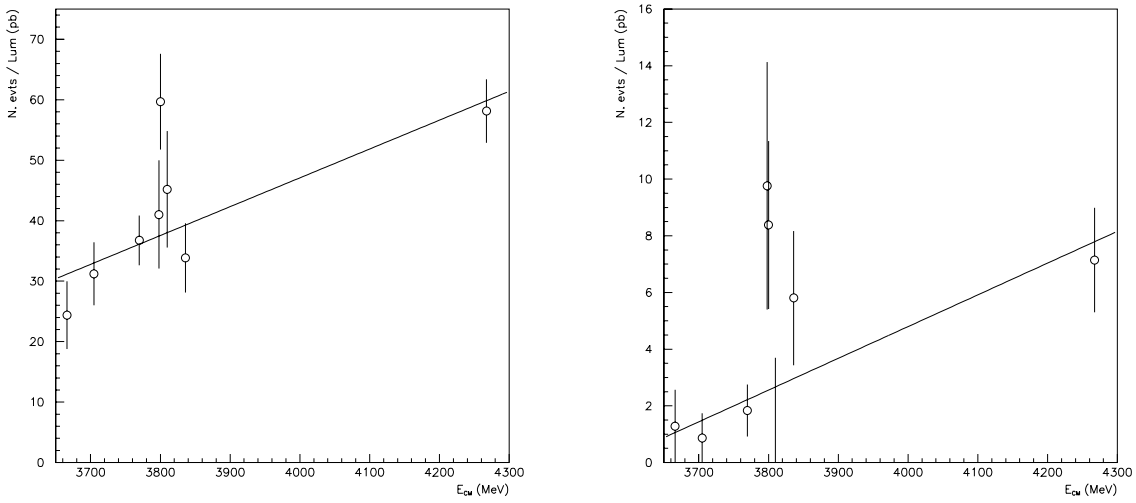

(a) (b)

Figure 4.11: N_{events}/L_I (pb) for (a) $\overline{p}p \rightarrow J/\psi X \rightarrow e^+e^-X$ and (b) $\overline{p}p \rightarrow J/\psi\pi^+\pi^- \rightarrow e^+e^-\pi^+\pi^-$ for energies far from ψ' resonance. Stack 52 and 53 have been considered together because of their tiny E_{CM} difference. The points are fitted with a first order polynomial; the fitted value for the continuum contamination at the ψ' energy are: (a) $N_{bkg}(J/\psi X)/L_I = 32 \pm 3$ pb ($\chi^2/ndf = 1.9$) and (b) $N_{bkg}(J/\psi\pi^+\pi^-)/L_I = 1.3 \pm 0.6$ pb ($\chi^2/ndf = 1.6$).

	Classified as				
Generated	e^+e^-	$J/\psi X$	$J/\psi\pi^+\pi^-$	$J/\psi\pi^0\pi^0$	$J/\psi\eta$
e^+e^-	-	0.046 ± 0.001	$< 10^{-4}$	$< 10^{-4}$	$< 10^{-4}$
$J/\psi\pi^+\pi^-$	$< 10^{-3}$	-	-	$< 10^{-4}$	$< 10^{-4}$
$J/\psi\pi^0\pi^0$	$< 10^{-3}$	-	0.0024 ± 0.0002	-	0.0057 ± 0.0004
$J/\psi\eta$	$< 10^{-3}$	-	$< 10^{-3}$	$< 10^{-4}$	-

Table 4.6: Event misidentification fractions f_{mis-id}.

Chapter 5

Results

In this chapter, the event samples that have been selected for all the ψ' decay channels will be used to measure the ratio of BR. To achieve this result the evaluation of the selection efficiency for all the analyzed channels is needed.

Using the $\psi' \to J/\psi\pi\pi$ selected samples it will be also possible to measure the dipion invariant mass distribution.

5.1 ψ' branching ratios

The cross section for a process

$$a + b \to R \to c + d$$

is proportional to the decay width , $(R \to c + d)$, as discussed in (3.1). The cross section can be obtained from (3.2), after deconvolution with the beam energy distribution, using the equation:

$$\sigma = \frac{N_{tot} - N_{bkg}}{\epsilon_{tot} \cdot \int \mathcal{L} dt}. \tag{5.1}$$

The total efficiency ϵ_{tot} of the selection is obtained as the product of the acceptance for the channel and of the efficiencies for each cut applied in the selection:

$$\epsilon_{tot} = \alpha \cdot \epsilon_{trig} \cdot \epsilon_{mdst} \cdot \epsilon_{EW} \cdot \epsilon_{fit} \tag{5.2}$$

where α is the acceptance for the e^+e^- due to charmonium decay, ϵ_{trig} the e^+e^- trigger efficiency, ϵ_{mdst} the efficiency ot the mdst preselection, ϵ_{EW} the EW cut efficiency and ϵ_{fit} is the kinematic fit selection efficiency. All these terms will be described in more detail later.

Some of these efficiency contributions may be the same for different channels; in this case, in the calculation of ratio of BR, they can be eliminated. Also, if

the analysis for different channels is done on the same data sample, the luminosity cancels and it is possible to write:

$$\frac{\mathcal{B}(\psi' \to X_1)}{\mathcal{B}(\psi' \to X_2)} = \frac{\epsilon_{tot}(X_2)}{\epsilon_{tot}(X_1)} \cdot \frac{N_{X_1}}{N_{X_2}}, \tag{5.3}$$

where $N_X = N_{X,tot} - N_{X,bkg}$ are the number of events after the background subtraction.

If the decay process proceeds through intermediate resonances, its BR to the observed final state must be included in (5.3). In this analysis the J/ψ is detected only via its e^+e^- decay and the π^0 and η by their $\gamma\gamma$ decay. The BR of these decay modes, according to the PDG, are [3]:

$$\mathcal{B}(J/\psi \to e^+e^-) = 5.93 \pm 0.10\% \tag{5.4}$$

$$\mathcal{B}(\eta \to \gamma\gamma) = 39.43 \pm 0.26\% \tag{5.5}$$

$$\mathcal{B}(\pi^0 \to \gamma\gamma) = 98.798 \pm 0.032\% \tag{5.6}$$

When the ratio of BR is calculated for final states $J/\psi + A$ and $J/\psi + B$ the contribution of (5.4) to the two channel cancels:

$$\frac{\mathcal{B}(\psi' \to J/\psi + A)}{\mathcal{B}(\psi' \to J/\psi + B)} = \frac{(\alpha\epsilon_{trig}\epsilon_{EW}\epsilon_{fit})(J/\psi + B)}{(\alpha\epsilon_{trig}\epsilon_{EW}\epsilon_{fit})(J/\psi + A)} \cdot \frac{N_{J/\psi+A}}{N_{J/\psi+B}}; \tag{5.7}$$

in this case also the ϵ_{mdst} factor can be simplified, as will be explained in Section 5.1.3. If one of the two channels is ψ' exclusive e^+e^- decay, the ratio of BR must also include $\mathcal{B}(J/\psi \to e^+e^-)$:

$$\frac{\mathcal{B}(\psi' \to e^+e^-)}{\mathcal{B}(\psi' \to J/\psi + A) \cdot \mathcal{B}(J/\psi \to e^+e^-)} = \\ = \frac{(\alpha\epsilon_{trig}\epsilon_{mdst}\epsilon_{EW}\epsilon_{fit})(J/\psi + A)}{(\alpha\epsilon_{trig}\epsilon_{mdst}\epsilon_{EW}\epsilon_{fit})(e^+e^-)} \cdot \frac{N_{e^+e^-}}{N_{J/\psi+A}}, \tag{5.8}$$

or, in the case of $J/\psi\eta$:

$$\frac{\mathcal{B}(\psi' \to J/\psi\eta) \cdot \mathcal{B}(\eta \to \gamma\gamma)}{\mathcal{B}(\psi' \to J/\psi + A)} = \\ = \frac{(\alpha\epsilon_{trig}\epsilon_{EW}\epsilon_{fit})(J/\psi + A)}{(\alpha\epsilon_{trig}\epsilon_{EW}\epsilon_{fit})(J/\psi\eta)} \cdot \frac{N_{J/\psi\eta}}{N_{J/\psi+A}}, \tag{5.9}$$

5.1.1 Acceptance

In the following, the acceptance α is intended for the requirement that both $e^\pm$ due to ψ' or J/ψ decay fall within the CCAL and Čerenkov fiducial region ($15° < \theta < 60°$), without requirements on the other particles of the final state.

	$\lambda_{\psi'} = 0.43$	$\lambda_{\psi'} = 0.69$	$\lambda_{\psi'} = 0.95$
$\alpha(e^+e^-)$	0.5752(5)	0.5517(5)	0.5326(5)
$\alpha(J/\psi\pi^+\pi^-)$	0.5479(5)	0.5242(5)	0.5037(5)
$\alpha(J/\psi\pi^0\pi^0)$	0.5479(5)	0.5242(5)	0.5031(5)
$\alpha(J/\psi\eta)$	0.6411(5)	0.6558(5)	0.6651(5)
$\alpha(J/\psi X)$	0.5531(6)	0.5316(7)	0.5125(8)

Table 5.1: Monte Carlo evaluation of acceptances for the e^+e^- pair ($15° < \theta_{e^\pm} < 60°$) for different channels. The acceptance for the J/ψ inclusive decay is obtained as the weighted average of the exclusive channels. The error is statistical only; for $J/\psi X$ the systematic error due to uncertainty in the $J/\psi\eta$ BR is also taken into account.

As was mentioned in Section 1.2, the angular distribution of e^+e^- coming from $\psi' \to e^+e^-$ was measured by E760 to be $\propto 1+\lambda_{\psi'}\cos^2\theta_e^*$ with $\lambda_{\psi'} = 0.69 \pm 0.26$. For this reason three samples of events with $\lambda_{\psi'} = 0.43$, 0.69, 0.95 have been generated.

For $J/\psi\pi\pi$ we used the hypothesis that the J/ψ has the same polarization than the ψ' , so for the decay $J/\psi \to e^+e^-$ we used $1 + \lambda_{\psi'}\cos^2\theta_e^*$ with the same $\lambda_{\psi'}$ value used in the $\psi' \to e^+e^-$ decay. Also the uncertainty on the shape of the dipion invariant mass distribution affects the acceptance evaluation. This effect is found to be of the order of 0.1% and has been neglected.

In the case of $J/\psi\eta$ the angular distribution for the two electrons is given by $1 + \frac{5}{4}\lambda_{\psi'} - \lambda_{\psi'}\cos^2\theta_e^*$, as discussed in [17].

The results for the acceptance, determined with the simulation of 10^6 events for each decay channel, are summarized in Table 5.1.

The main source of error on α comes from the uncertainty on $\lambda_{\psi'}$. Anyway the ratio of acceptances for different channels is less sensitive to $\lambda_{\psi'}$ so, the values of α ratios that will be used in the analysis are:

$$\frac{\alpha(J/\psi X)}{\alpha(e^+e^-)} = 0.963 \pm 0.001, \tag{5.10}$$

$$\frac{\alpha(J/\psi X)}{\alpha(J/\psi\pi^+\pi^-)} = 1.014 \pm 0.004, \tag{5.11}$$

$$\frac{\alpha(J/\psi X)}{\alpha(J/\psi\pi^0\pi^0)} = 1.014 \pm 0.004, \tag{5.12}$$

$$\frac{\alpha(J/\psi X)}{\alpha(J/\psi\eta)} = 0.81 \pm 0.05, \tag{5.13}$$

$$\frac{\alpha(J/\psi\pi^+\pi^-)}{\alpha(J/\psi\pi^0\pi^0)} = 1.000 \pm 0.001. \tag{5.14}$$

5.1.2 Trigger efficiency

The E835 (e^+e^-) trigger, already illustrated in Section 3.4, is the OR of three branches:

$$\begin{aligned}(e^+e^-) &= (2e)\otimes(H2\leq 5)\otimes(PBG3)\\ &\oplus\ (1e)\otimes(2h)\otimes(H2=2)\otimes(H2copl1/3)\otimes(PBG3)\\ &\oplus\ (2e)\otimes(H2=2)\otimes(H2copl1/3)\otimes\overline{(FCH)}.\\ &= (b1)\oplus(b2)\oplus(b3)\end{aligned}$$

$(b1)$ is the main branch; $(b2)$ and $(b3)$ require exactly 2 $H2$ elements hit, therefore they are very inefficient in the case of $J/\psi\pi^+\pi^-$, where 4 charged particles are present. For this reason two different values for the trigger efficiency are expected: one for $e^+e^- + charged$ and the other for $e^+e^- + neutrals$ channels.

The trigger efficiency has been measured by selecting a clean e^+e^- sample from data of stack 29, where a looser "one electron" trigger is used[1]. From the analysis of this sample, it has been determined that $\epsilon_{trig}(e^+e^-) = 0.90 \pm 0.02$, where the efficiency of $(b1)$ is $\epsilon_{(b1)} = 0.86 \pm 0.02$ [64]. The statistic error dominates the ϵ_{trig} measurement so a precision measurement of the trigger efficiency is done with the Monte Carlo.

100000 events for each reaction have been simulated. The results for the trigger efficiency are summarized in Table 5.2. As expected, the $e^+e^- + neutrals$ channels have almost the same efficiency.

5.1.3 Invariant mass cut efficiency

The mdst preselection requires that the invariant mass of the two e^+e^- candidates is $m_{ee} \geq 2.6$ GeV. The efficiency of the mdst preselection is $\sim 96\%$. In the framework adopted, the absolute value of ϵ_{mdst} is not very important, however the ratio of ϵ_{mdst} for different channels must be determined with high precision.

ϵ_{mdst} is different if the e^+e^- pair is due to a ψ' or a J/ψ decay. The measured invariant mass distribution for the e^+e^- candidates obtained with the GEANT Monte Carlo is shown in Figure 5.1. The low energy tail is a consequence of the $e^\pm$ loss of energy in the detector material and of the resolution of the CCAL. Since $M_{J/\psi} < M_{\psi'}$, the fraction of J/ψ events with a measured m_{ee} below the mdst threshold will be

[1] The "one electron" trigger used during stack 29 data taking requires $(1e)\otimes(PBG3)$ for branch $(b2)$. So it is:

$$\begin{aligned}(e^+e^-)_{stack\ 29} &= (2e)\otimes(H2\leq 5)\otimes(PBG3)\\ &\oplus\ (1e)\otimes(PBG3)\\ &\oplus\ (2e)\otimes(H2=2)\otimes(H2copl1/3)\otimes\overline{(FCH)};\end{aligned}$$

the notation used is the one of Section 3.4.

	N. events				
	e^+e^-	$J/\psi\pi^+\pi^-$	$J/\psi\pi^0\pi^0$	$J/\psi\eta$	$J/\psi X$
$\epsilon_{(b1)}$	0.872(1)	0.872(1)	0.871(1)	0.874(1)	
$\epsilon_{(b2)}$	0.813(1)	0.068(1)	0.651(2)	0.730(1)	
$\epsilon_{(b3)}$	0.779(1)	0.035(1)	0.604(2)	0.689(1)	
ϵ_{trig}	0.900(1)	0.876(1)	0.897(1)	0.901(1)	0.887(1)

Table 5.2: Charged trigger efficiency from Monte Carlo. $\epsilon_{trig}(J/\psi X)$ is obtained as the weighted average of the exclusive channels. For the full reconstruction of the $J/\psi\pi^+\pi^-$ final states both pions must be in the inner tracking acceptance and the trigger efficiency could be different with respect to the one quoted here, evaluated without any requirement on the $\pi^\pm$ directions, because of the higher average number of H1 elements hit and the $(b2)$ and $(b3)$ correlated inefficiency. Anyway, the efficiency of the two branches is already low for $J/\psi\pi^+\pi^-$ and it has been verified that, even requiring $15° < \theta_{\pi^\pm} < 55°$, the efficiency does not change: $\epsilon_{trig}(J/\psi\pi^+\pi^-,\ 15° < \theta_{\pi^\pm} < 55°) = 0.877 \pm 0.002$.

higher than the corresponding fraction of ψ' events, and so $\epsilon_{mdst}(J/\psi) < \epsilon_{mdst}(\psi')$. The efficiency ratio has been determined with GEANT to be:

$$\frac{\epsilon_{mdst}(J/\psi)}{\epsilon_{mdst}(\psi')} = 0.992 \pm 0.001, \tag{5.15}$$

in perfect agreement with the number determined for E835-I [31].

5.1.4 Electron Weight efficiency

The precise evaluation of the EW efficiency for different channels can be obtained from data, without using the simulation, as described in Appendix C. In the exclusive selection of events opening angles between photons coming from π^0 or η decay and $e^\pm$ tracks are required larger than 100 mrad, then the additional γ's should not affect the electron shower shape. For this reason ϵ_{EW} is the same for all $J/\psi + neutrals$ channels.

For $J/\psi\pi^+\pi^-$ the situation is different. The EW of the $e^\pm$ tracks is lowered due to the energy deposit in the hodoscopes if a $\pi^\pm$ hit the same hodoscope element (see Appendix C.1). Since H1 is segmented into 8 parts, a cut on the opening angle requiring that the two $\pi^\pm$ tracks hit different (with respect to $e^\pm$) hodoscope element will result in a substantial reduction of the sample. For this reason we have decided to measure ϵ_{EW} using a clean $J/\psi\pi^+\pi^-$ sample, selected without EW cut but with a 1% cut on the kinematic fit probability. All the details are given in Appendix C.

In the selection of J/ψ inclusive events, containing all the $J/\psi\pi^+\pi^-$, $J/\psi\pi^0\pi^0$ and $J/\psi\eta$ contributions, no checks on the opening angles of additional photons or

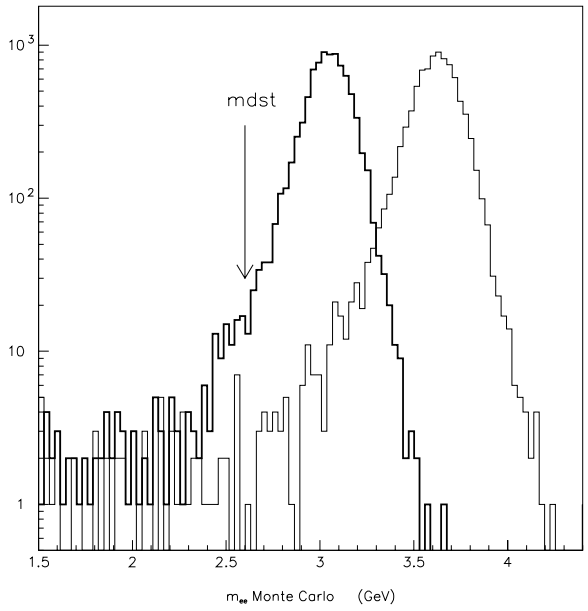

Figure 5.1: m_{ee} distribution for $\psi' \to e^+e^-$ and $J/\psi \to e^+e^-$ (bold). The arrow indicates the cut of the mdst preselection at 2.6 GeV.

	ϵ_{EW}
$e^+e^- + neutrals$	0.929 ± 0.004
$e^+e^- + \pi^+\pi^-$	0.887 ± 0.009
$e^+e^- + X$	0.883 ± 0.004

Table 5.3: Electron Weight selection efficiency for E835-II for the cut $EW_1 \cdot EW_2 > 1.5$.

charged tracks can be performed. Therefore it is expected that $\epsilon_{EW}(e^+e^- + X)$ value is lower than $\epsilon_{EW}(e^+e^- + neutrals)$.

The results, obtained from the analysis of the data are summarized in Table 5.3.

5.1.5 Kinematic fit efficiency

The efficiency of the selection is evaluated with the GEANT Monte Carlo. A sample of 50000 events for each one of the analyzed channels, with both e^+e^- within the detector fiducial region, have been produced. The hits in the detector are reconstructed and analyzed with the same procedure used for the data.

When other particles are present in the final state they should hit the detector

Stack	ϵ_{fit}
1	0.314 ± 0.002
2	0.313 ± 0.002
14	0.319 ± 0.002
29	0.329 ± 0.002
30	0.329 ± 0.002
49	0.328 ± 0.002
50	0.314 ± 0.002
51	0.326 ± 0.002
54	0.308 ± 0.002

Table 5.4: Values of ϵ_{fit} for $J/\psi\pi^+\pi^-$ events divided by stack, evaluated with the GEANT Monte Carlo. The error is statistical only.

	ϵ_{fit}
e^+e^-	0.935 ± 0.033
$J/\psi\pi^+\pi^-$	0.319 ± 0.014
$J/\psi\pi^0\pi^0$	0.157 ± 0.016
$J/\psi\eta$	0.484 ± 0.053
$J/\psi X$	0.990 ± 0.015

Table 5.5: Monte Carlo evaluation of kinematic fit efficiency ($\text{prob}(\chi^2) > 10^{-2}$ for $J/\psi\eta$ and $\text{prob}(\chi^2) > 10^{-4}$ for all the other channels). The systematic error is obtained by trying different probability cuts. $\epsilon_{fit}(J/\psi\pi^+\pi^-)$ is the weighted average of the values in Table 5.4.

to be detected before applying the kinematic fit. ϵ_{fit} measured in this case is the product of the kinematic fit efficiency and the acceptance for all the particles to be within the detector fiducial volume.

The simulated events, satisfying the software (e^+e^-) trigger requirements, are passed to the kinematic fit analysis with the same procedure used for data. The cut on the kinematic fit probability is the same that has been used in Section 4.3 for data ($\text{prob}(\chi^2) > 10^{-2}$ for $J/\psi\eta$ and $\text{prob}(\chi^2) > 10^{-4}$ for all the other channels). The systematic error associated to the efficiency is calculated by changing the kinematic fit probability cuts.

For $J/\psi\pi^+\pi^-$, the event detection efficiency depends on the efficiency of the tracking detector. While the straw chambers and the hodoscopes behaviors are stable over all the data taking period, during each stack some fibers were off because of fiber or VLPC damage, high VLPC temperature or broken QPA02 card. Once per stack a calibration on the fiber detector was done and this is used into the GEANT

Channel	e^+e^-	$J/\psi X$	$J/\psi\pi^+\pi^-$	$J/\psi\pi^0\pi^0$	$J/\psi\eta$
N_{evts}	5300 ± 70	26810 ± 160	4380 ± 70	1264 ± 36	387 ± 20
N_{ext}	6^{+15}_{-5}	350 ± 50	15^{+20}_{-10}	6^{+15}_{-5}	< 11 (68% C.L.)
N_{int}	< 27	260 ± 9	19 ± 2	< 2	46 ± 3
N	5300 ± 75	26200 ± 170	4350 ± 70	1260 ± 40	341 ± 23

Table 5.6: Number of events observed in the E835-II sample. N_{evts} is the number of observed events with the statistical error; N_{ext} are events due to non resonant J/ψ production and N_{int} come from event misidentification; N is the number of events from charmonium decay.

simulation to simulate the fiber signals. In addition, in stack 50, the element number 22 of H2′ was not connected. All this effects are taken into account for the evaluation of the analysis efficiency for each stack, done with GEANT. The same set of 50000 events have been analyzed with different calibrations and running conditions. The values for $\epsilon_{fit}(J/\psi\pi^+\pi^-)$ for each ψ' stack are summarized in Table 5.4. The results for all channels are in Table 5.5

5.1.6 Background subtraction

The number of events due to continuum (non resonant) production and misidentified events, evaluated in Section 4.5, has to be subtracted from the total number of events observed in each channel. The integrated luminosity collected in the ψ' resonance energy region is $\int \mathcal{L}_{\psi'} dt = 12.5$ pb^{-1}.

The number of background events due to non resonant J/ψ events (or "external" background) N_{ext} is obtained from $N_{bkg}/L_{I,bkg}$ given in Table 4.5:

$$N_{ext} = \frac{N_{bkg}}{L_{I,bkg}} \int \mathcal{L}_{\psi'} dt. \tag{5.16}$$

The number of misidentified events ("internal" background) is obtained as a fraction f_{mis-id} (given in Table 4.6) of the total number of "contaminating" events:

$$N_{int} = N_{cont} \cdot f_{mis-id}. \tag{5.17}$$

Table 5.6 shows the total number of events after background subtraction.

5.1.7 Ratios of BR

Inserting the background subtracted number of events and the calculated efficiencies in (5.7), (5.8) and (5.9) it is now possible to calculate:

$$\frac{\mathcal{B}(\psi' \to e^+e^-)}{\mathcal{B}(\psi' \to J/\psi X)\mathcal{B}(J/\psi \to e^+e^-)} = 0.192 \pm 0.008, \tag{5.18}$$

$$\frac{\mathcal{B}(\psi' \to J/\psi\pi^+\pi^-)}{\mathcal{B}(\psi' \to J/\psi X)} = 0.527 \pm 0.027, \tag{5.19}$$

$$\frac{\mathcal{B}(\psi' \to J/\psi\pi^0\pi^0)\mathcal{B}(\pi^0 \to \gamma\gamma)^2}{\mathcal{B}(\psi' \to J/\psi X)} = 0.288 \pm 0.031, \tag{5.20}$$

$$\frac{\mathcal{B}(\psi' \to J/\psi\eta)\mathcal{B}(\eta \to \gamma\gamma)}{\mathcal{B}(\psi' \to J/\psi X)} = 0.0202 \pm 0.0028; \tag{5.21}$$

and using the PDG values (5.4), (5.5) and (5.6):

$$\frac{\mathcal{B}(\psi' \to e^+e^-)}{\mathcal{B}(\psi' \to J/\psi X)} = 0.0114 \pm 0.0005, \tag{5.22}$$

$$\frac{\mathcal{B}(\psi' \to J/\psi\pi^0\pi^0)}{\mathcal{B}(\psi' \to J/\psi X)} = 0.295 \pm 0.032, \tag{5.23}$$

$$\frac{\mathcal{B}(\psi' \to J/\psi\eta)}{\mathcal{B}(\psi' \to J/\psi X)} = 0.051 \pm 0.007. \tag{5.24}$$

The results are in agreement with the PDG values, with the only exception of (5.22).

A direct calculation of the ratio $\mathcal{B}(\psi' \to J/\psi\pi^0\pi^0)/\mathcal{B}(\psi' \to J/\psi\pi^+\pi^-)$ is independent from the acceptance α, which is the same for the two channels. By selecting only the events in which the $\pi^\pm$ hit different hodoscope elements with respect to the ones hit by $e^\pm$, also ϵ_{EW} is the same for the two samples and the systematic error associated to the selection can be further reduced. In this case the number of $J/\psi\pi^+\pi^-$ selected events is 2545. The selection efficiency, determined as before with GEANT events is $\epsilon_{fit}(J/\psi\pi^+\pi^-) = 0.195 \pm 0.006$. The ratio of BR for the two channels is:

$$\left.\frac{\mathcal{B}(\psi' \to J/\psi\pi^0\pi^0)}{\mathcal{B}(\psi' \to J/\psi\pi^+\pi^-)}\right|_{restricted\ sample} = 0.615 \pm 0.069. \tag{5.25}$$

By using the ratio of ϵ_{EW} it is possible to use the whole $J/\psi\pi^+\pi^-$ sample to obtain:

$$\left.\frac{\mathcal{B}(\psi' \to J/\psi\pi^0\pi^0)}{\mathcal{B}(\psi' \to J/\psi\pi^+\pi^-)}\right|_{all\ sample} = 0.560 \pm 0.064, \tag{5.26}$$

which is in good agreement with (5.25).

The (5.25) and (5.26) show that the possibility of isospin violation in $\psi' \to J/\psi\pi\pi$ is at most at a level of a few percent, as discussed in Section 1.4.1.

The contributions to the total number of observed e^+e^- candidates from all the analyzed decay channels, obtained scaling the number of events for each channel with the efficiency for the reconstruction of the full event, are shown in Figure 5.2. The missing events might be related to the double radiative decays

$$\psi' \to \chi_J\gamma \to J/\psi\gamma\gamma \quad (J = 0, 1, 2),$$

which have not been analyzed in this work.

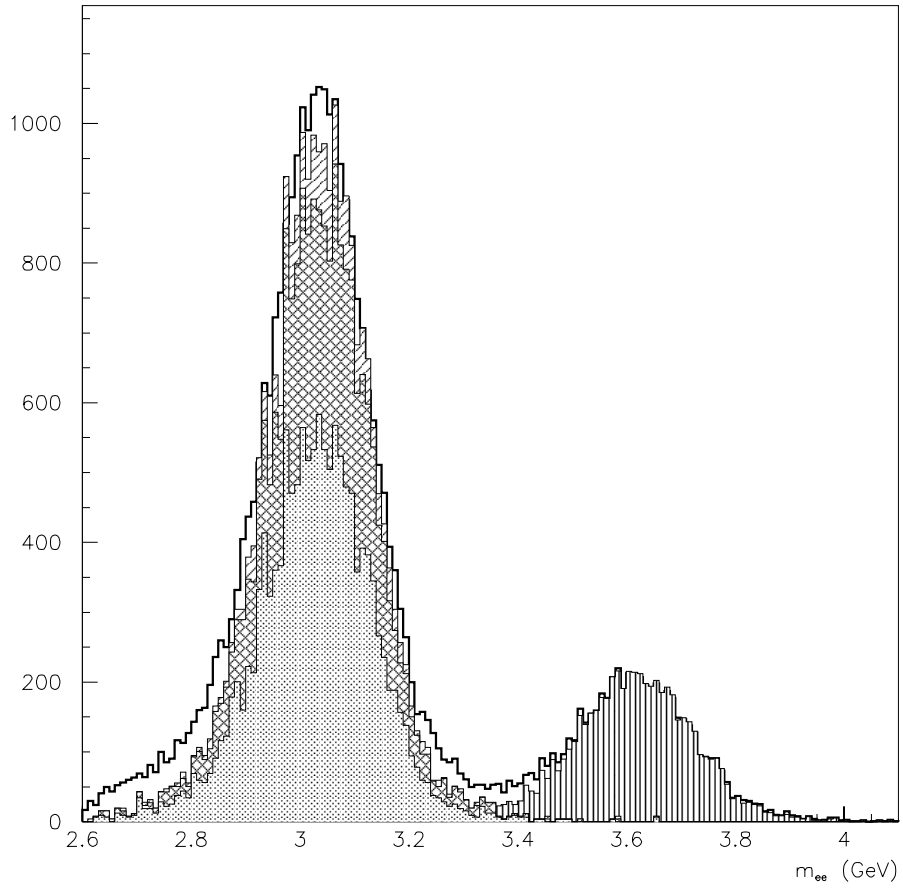

Figure 5.2: Contributions to the total number of observed e^+e^- candidates from all the exclusive channels analyzed. Vertical lines: e^+e^- exclusive; dot shaded area: $J/\psi\pi^+\pi^-$; cross hatched: $J/\psi\pi^0\pi^0$; diagonal lines: $J/\psi\eta$. The errors on the contributions are not shown.

5.1.8 Comparison with previous experiments

Using the PDG value $\mathcal{B}(\psi' \to J/\psi X) = 0.557 \pm 0.026$ [3], it is possible to extract from (5.22), (5.19), (5.20) and (5.24) the branching ratios for the exclusive ψ' decays:

$$\mathcal{B}(\psi' \to e^+e^-) = 0.0063 \pm 0.0004, \quad (5.27)$$

$$\mathcal{B}(\psi' \to J/\psi\pi^+\pi^-) = 0.294 \pm 0.020, \quad (5.28)$$

$$\mathcal{B}(\psi' \to J/\psi\pi^0\pi^0) = 0.164 \pm 0.019, \quad (5.29)$$

$$\mathcal{B}(\psi' \to J/\psi\eta) = 0.028 \pm 0.004, \quad (5.30)$$

that can be compared with the measurements by other experiments. The comparison is not always straightforward because the BR values are often obtained measuring combinations of branching ratios for different channels and using BR values taken from the PDG published at the time, as discussed in Chapter 2. Figures 5.3 to 5.6 show the comparison between the BR values obtained in this thesis and other experiments; for each measurement we report the result as it is given in the original paper.

Each measurement obtained in this thesis has an error comparable with the PDG fit. The values are compatible within 1σ with the PDG, with the only exception of $\mathcal{B}(\psi' \to e^+e^-)$, which is slightly smaller.

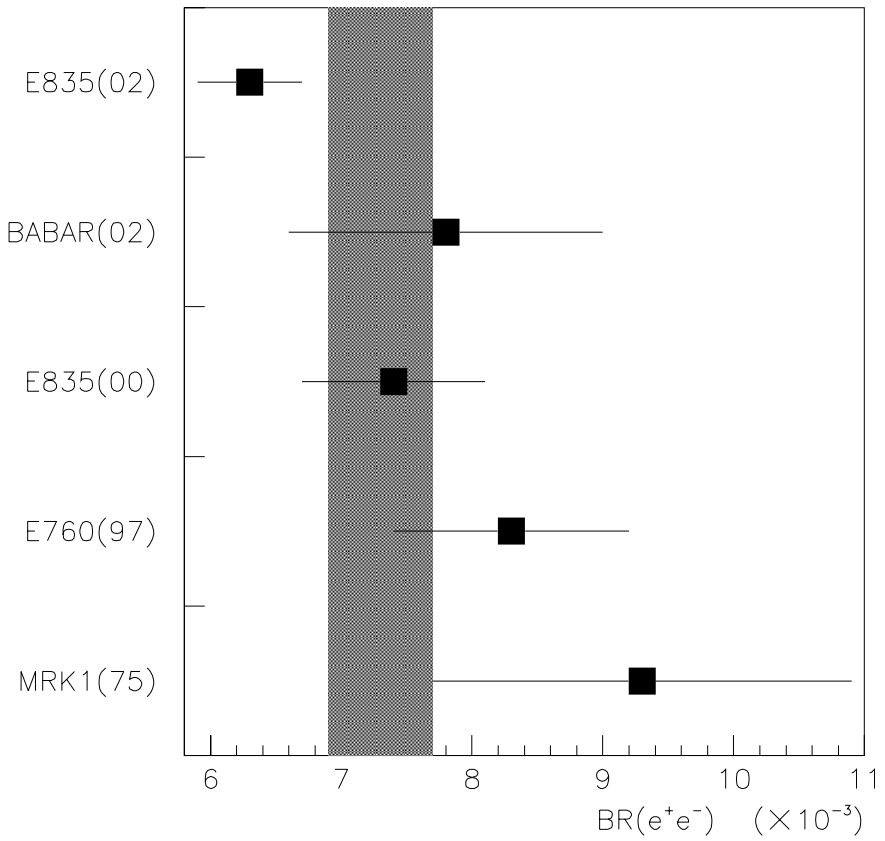

Figure 5.3: $\mathcal{B}(\psi' \to e^+e^-)$ as measured by various experiments. E835(02) value is this analysis. The shaded region is the 1σ PDG value. Related references: MRK1(75) [29], E760(97) [16], E835(00) [31], BABAR(02) [32]. The MRK1(75) value is not used in the PDG fit.

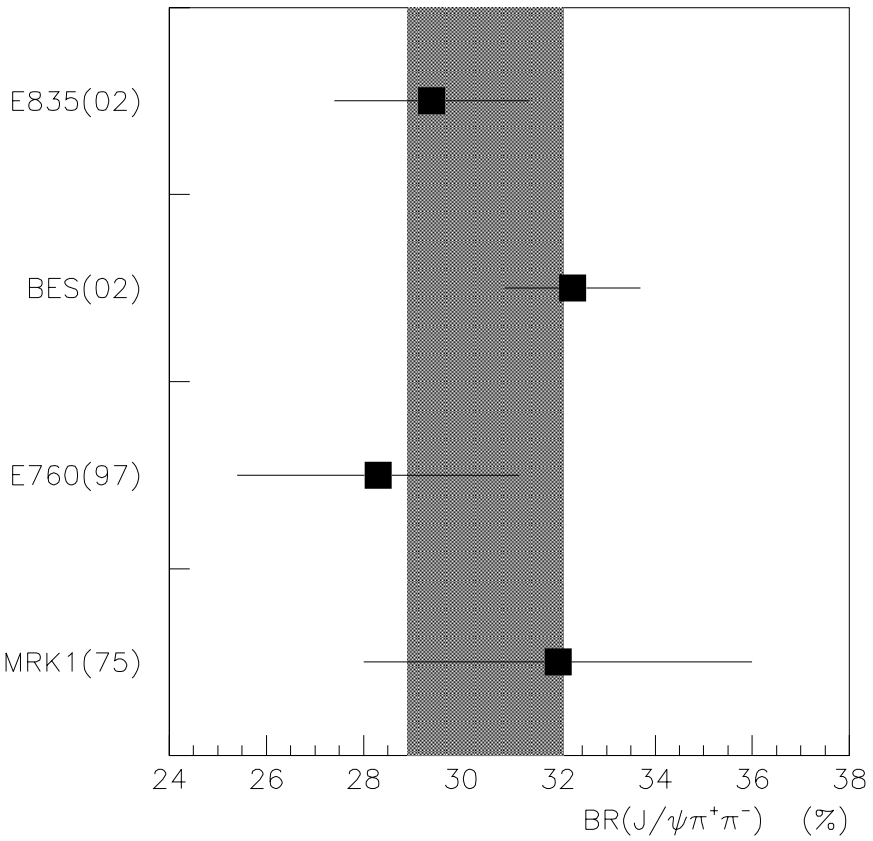

Figure 5.4: $\mathcal{B}(\psi' \to J/\psi\pi^+\pi^-)$ as measured by various experiments. E835(02) value is this analysis. The shaded region is the 1σ PDG value. Related references: MRK1(75) [33], E760(97) [16], BES(02) [38]. The BES(02) value is not used in the PDG fit.

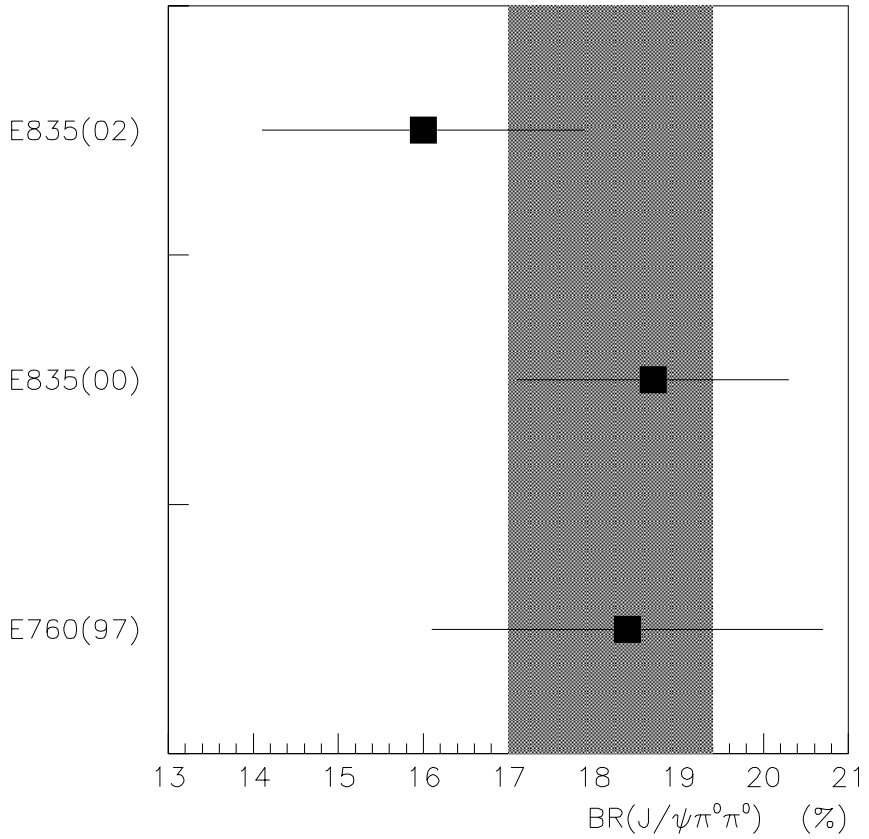

Figure 5.5: $\mathcal{B}(\psi' \to J/\psi\pi^0\pi^0)$ as measured by various experiments. E835(02) value is this analysis. The shaded region is the 1σ PDG value. Related references: E760(97) [16], E835(00) [31].

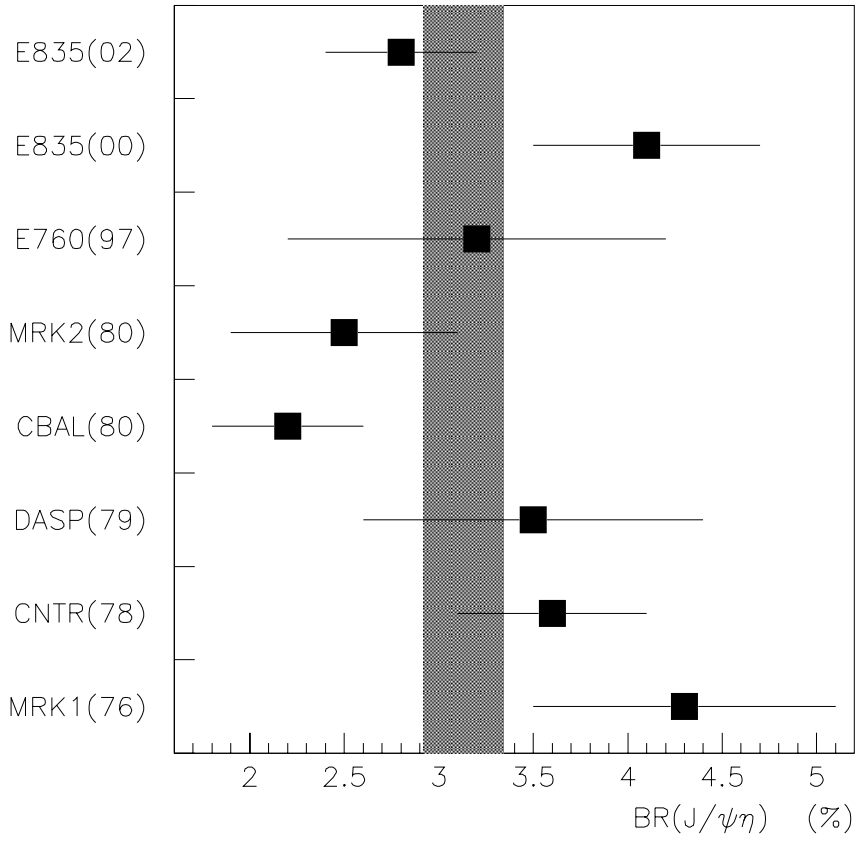

Figure 5.6: $\mathcal{B}(\psi' \to J/\psi\eta)$ as measured by various experiments. E835(02) value is this analysis. The shaded region is the 1σ PDG value. Related references: MRK1(76) [34], CNTR(78) [42], DASP(79) [41], CBAL(80) [40], MRK2(80) [39], E760(97) [16], E835(00) [31]. The MRK1(76) value is not used in the PDG fit.

5.2 Dipion invariant mass distribution in $\psi' \to J/\psi\pi\pi$

More than 5000 $\psi' \to J/\psi\pi\pi$ events are identified and fully reconstructed. With this sample it is possible to make a measurement of the dipion invariant mass distribution.

Bin-by-bin corrections for the acceptance have been calculated and applied to the data before fitting the distributions. The corrected $m_{\pi\pi}$ distributions are shown in Figure 5.7. (2.28) and (2.29) can be used to fit the reconstructed distribution of $m_{\pi\pi}$.

The $\lambda_{\pi\pi}$ value obtained have been checked on a set of GEANT $\psi' \to J/\psi\pi\pi$ events produced under the assumption that:

- the dipion invariant mass distribution is (2.28) with $\lambda_{\pi\pi} = 4$;
- the J/ψ and the dipion are in a relative S wave;
- the two pions in the $(\pi\pi)$ system are in S wave.

The analysis of GEANT data shows that the dipion invariant mass distribution is correctly reconstructed (see Figure 5.8) but a systematic error $\sigma_\lambda(\pi^+\pi^-) = \pm 0.25$ and $\sigma_\lambda(\pi^0\pi^0) = \pm 0.10$ must be associated to the measurement.

Tables 5.7 and 5.8 show the stability of the fit result by changing the binning of the data. An additional 7% systematic error has been associated to the binning choice for both channels.

The behavior of the χ^2 for the fit to the $m_{\pi\pi}$ distribution with (2.28) at different $\lambda_{\pi\pi}$ is summarized in Table 5.9.

The results are:

$$\lambda_{\pi^+\pi^-} = 2.86 \pm 0.14 \pm 0.30, \tag{5.31}$$

$$\lambda_{\pi^0\pi^0} = 3.71 \pm 0.28 \pm 0.27, \tag{5.32}$$

or, in the Novikov - Shifman parametrization, fitting with (2.29):

$$\mathcal{K}_{\pi^+\pi^-} = 0.117 \pm 0.006 \pm 0.012, \tag{5.33}$$

$$\mathcal{K}_{\pi^0\pi^0} = 0.166 \pm 0.006 \pm 0.012. \tag{5.34}$$

The results for $J/\psi\pi^+\pi^-$ are not consistent with the only other measurement by BES, quoted in Section 2.3.1.

The χ^2 values obtained fitting the distribution with the two theoretical parametrizations are almost the same. Hence it is not possible to determine which one is in better agreement with the data.

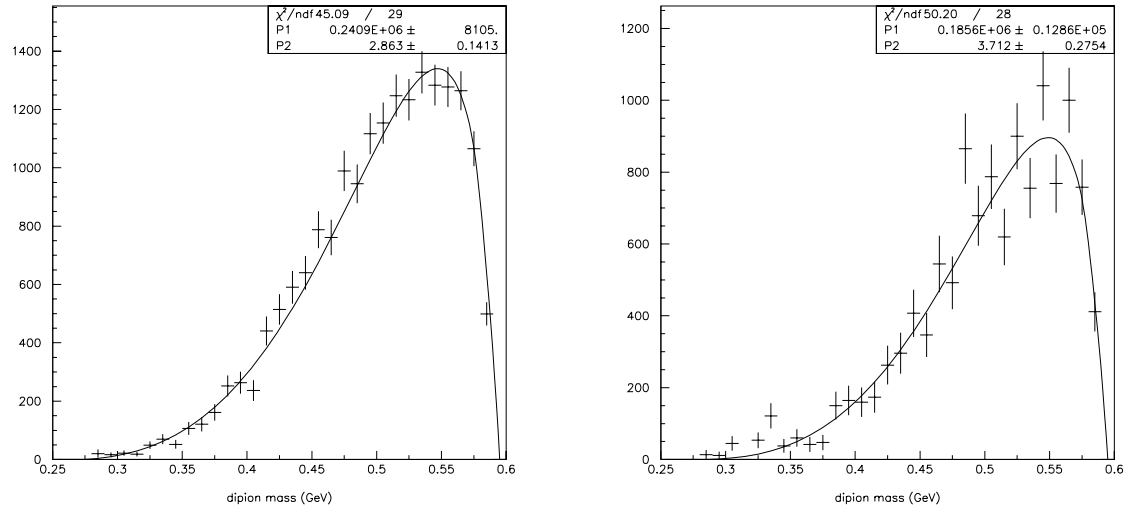

(a) (b)

Figure 5.7: (a) $J/\psi\pi^+\pi^-$ and (b) $J/\psi\pi^0\pi^0$ corrected $m_{\pi\pi}$ distributions. The solid line is the fit with (2.28).

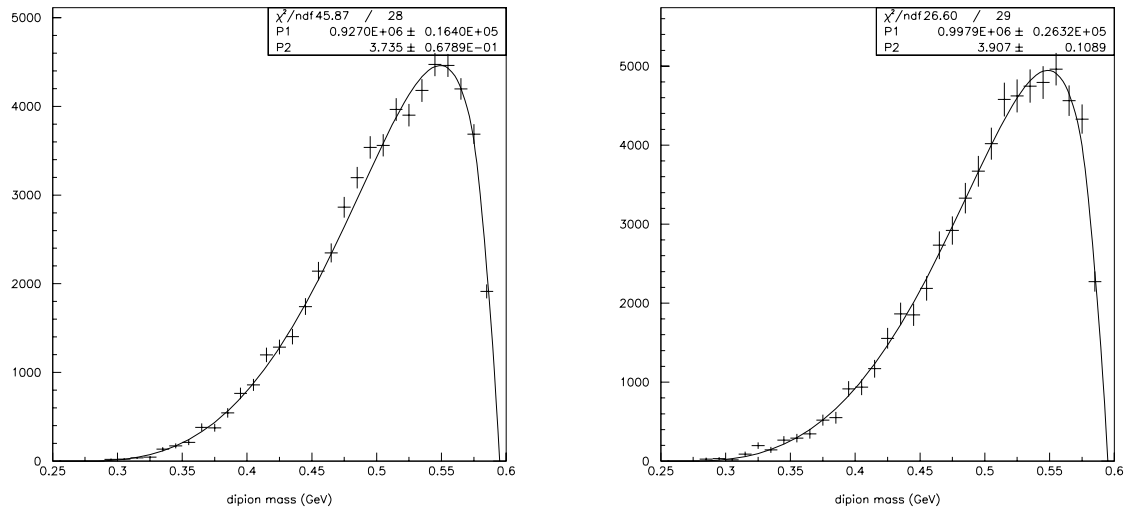

(a) (b)

Figure 5.8: (a) $J/\psi\pi^+\pi^-$ and (b) $J/\psi\pi^0\pi^0$ corrected $m_{\pi\pi}$ distribution on Monte Carlo data. The solid line is the fit with (2.28).

N. bins	$\lambda_{\pi\pi}$	χ^2/ndf	$\mathcal{K}$	χ^2/ndf
25	2.81 ± 0.14	2.4	0.115 ± 0.006	2.3
30	2.85 ± 0.14	1.3	0.116 ± 0.006	1.2
35	2.86 ± 0.14	1.6	0.117 ± 0.006	1.4
40	2.86 ± 0.14	1.4	0.117 ± 0.006	1.3
45	2.90 ± 0.14	0.9	0.119 ± 0.006	0.8
50	3.05 ± 0.14	2.1	0.125 ± 0.006	2.0

Table 5.7: Stability of the results of the fit to $m_{\pi\pi}$ for $J/\psi\pi^+\pi^-$ events, by changing the binning of the data. The number of bins corresponds to the region $0.25 < m_{\pi\pi} < 0.6$ GeV.

N. bins	$\lambda_{\pi\pi}$	χ^2/ndf	$\mathcal{K}$	χ^2/ndf
25	4.02 ± 0.27	2.1	0.162 ± 0.013	2.2
30	3.91 ± 0.30	1.8	0.159 ± 0.014	1.9
35	4.06 ± 0.29	1.8	0.166 ± 0.006	1.8
40	4.17 ± 0.29	1.7	0.172 ± 0.014	1.7
45	4.27 ± 0.29	1.7	0.177 ± 0.014	1.7
50	4.24 ± 0.28	1.8	0.174 ± 0.013	1.8

Table 5.8: Stability of the results of the fit to $m_{\pi\pi}$ for $J/\psi\pi^0\pi^0$ events, by changing the binning of the data. The number of bins corresponds to the region $0.25 < m_{\pi\pi} < 0.6$ GeV.

$\lambda_{\pi\pi}$	χ^2/ndf $(\pi^+\pi^-)$	χ^2/ndf $(\pi^0\pi^0)$
2.0	2.8	3.2
2.5	1.8	2.7
3.0	1.6	2.2
3.5	2.2	1.9
4.0	3.7	1.8
4.5	5.9	1.9
5.0	8.7	2.1
5.5	11.7	2.6
6.0	15.0	3.2

Table 5.9: χ^2/ndf values obtained fitting the $m_{\pi\pi}$ distribution with (2.28) fixing the λ parameter.

Conclusions

The measurement of the ψ' branching ratios for the decay channels e^+e^-, $J/\psi X$, $J/\psi\pi^+\pi^-$, $J/\psi\pi^0\pi^0$ and $J/\psi\eta$ is reported in this thesis.

The measurement is based on the analysis of $\sim$ 33000 high invariant mass e^+e^- pair due to ψ' or J/ψ decay, and the following reconstruction of the exclusive channels when all the final state particles are observed. The analysis has been made on the ψ' data sample collected by the Fermilab E835 experiment in the second run (year 2000),

Using the PDG value $\mathcal{B}(\psi' \to J/\psi X) = 0.557 \pm 0.026$ we obtained:

$$\begin{aligned}
\mathcal{B}(\psi' \to e^+e^-) &= 0.0063 \pm 0.0004, \\
\mathcal{B}(\psi' \to J/\psi\pi^+\pi^-) &= 0.294 \pm 0.020, \\
\mathcal{B}(\psi' \to J/\psi\pi^0\pi^0) &= 0.164 \pm 0.019, \\
\mathcal{B}(\psi' \to J/\psi\eta) &= 0.028 \pm 0.004,
\end{aligned}$$

all the BR are measured with a precision comparable with the PDG fit.

All the exclusive channels have been fully reconstructed, allowing the measurement of the dipion invariant mass distribution for both $J/\psi\pi^+\pi^-$ and $J/\psi\pi^0\pi^0$, which is a test of the appropriateness of the multipole expansion treatment for the description of the gluon emission in the $\bar{c}c$ hadronic deexcitation. The results obtained show a good agreement between the data and the theoretical predictions.

The measurement:

$$\frac{\mathcal{B}(\psi' \to J/\psi\pi^0\pi^0)}{\mathcal{B}(\psi' \to J/\psi\pi^+\pi^-)} = 0.615 \pm 0.069$$

shows the possibility of an isospin violation at the level of few percent, in agreement with the light quark mass difference effect and the scale of electromagnetic to strong interaction at the quarkonium dimension scale.

Appendix A

Multiple Scattering Effect

When a charged particle travels in a medium, its motion direction is deflected because of coulomb scattering on several nuclei. This is called multiple scattering (MS). The angular deviation distribution is roughly gaussian for small deflections, with Rutherford-like tails at large angles.

The rms angular deviation θ_0 is given by [3]:

$$\theta_0 = \frac{13.6 \text{ MeV}}{\beta cp} z \sqrt{\frac{x}{X_0}} \left(1 + 0.038 \ln \frac{x}{X_0} \right), \tag{A.1}$$

where p, βc and z are the momentum, velocity and charge number of the incident particle; x/X_0 is the thickness of the scattering medium in radiation lengths.

It can be seen from (A.1) that the effect of MS increases as the medium thickness increases or the particle velocity decreases.

The detector with the best angular resolution in E835 is the scintillating fiber tracker. Its resolution ranges from less than 1 mrad at small θ to 4 mrad at large θ. The θ measurement process is sketched in Figure A.1. For some of the particles observed in the E835 detector, the multiple scattering deviation is higher than its intrinsic resolution.

The two kind of charged particles analyzed in this thesis are $e^{\pm}$ and $\pi^{\pm}$. Since the $e^{\pm}$ come from J/ψ or ψ' decay, they have a high velocity, then the deviation from original trajectory due to MS is low. On the other hand, $\pi^{\pm}$ come from $\psi' \to J/\psi\pi^+\pi^-$ so their kinetic energy is often low and the MS effect becomes appreciable. In addition, since the final state particles have a non-zero boost, particles moving forward traverse more material than the ones moving backward but they have a greater kinetic energy. For $\pi^{\pm}$ coming from $\psi' \to J/\psi\pi^+\pi^-$ decay, θ_0 is ~ 6 mrad (see Figure A.2).

The uncertainty on the θ measurement given from the detector track reconstruction routines should be corrected in order to take into account MS effect. Considering that:

- the momentum of $\pi^{\pm}$ can not be measured in E835 detector;

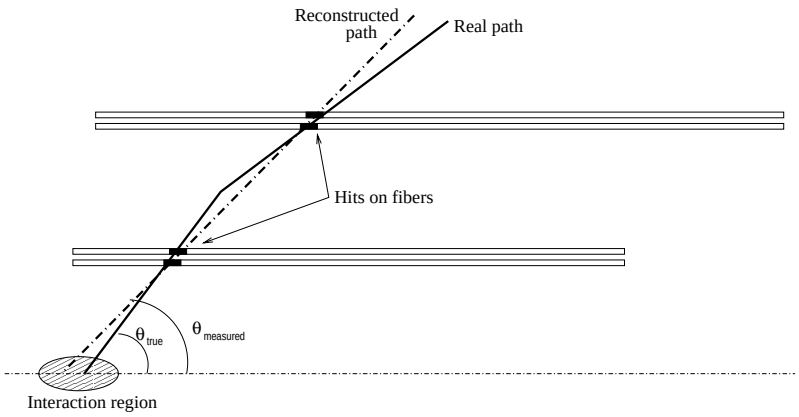

Figure A.1: Effect on MS on θ measurement in the scintillating fiber detector. The difference between measured and true particle emission angle θ could be in some cases greater than the intrinsic angular resolution of the detector.

- the $e^{\pm}$ energy is strongly related to their θ angle, because they come from a two body decay;
- the angular resolution of the scintillating fiber tracker is not uniform in θ because of the granularity of the detector;

we decided to parametrize the error on θ measurement, σ_θ, as a function of θ only, instead of using β and x/X_0.

To do so the GEANT Monte Carlo has been used, looking at the deviation between generated and measured angles for $e^{\pm}$ and $\pi^{\pm}$ for $\psi' \to J/\psi\pi^+\pi^-$ reactions. We obtained the following parametrization:

$$\sigma_{\theta,e}(\theta) = 1 + 5 \cdot \theta^2 \ \text{mrad} \tag{A.2}$$

$$\sigma_{\theta,\pi}(\theta) = -3.2 + 59.8 \cdot \theta - 116.9 \cdot \theta^2 + 76.9 \cdot \theta^3 \ \text{mrad} \tag{A.3}$$

in the angular region $15° \leq \theta \leq 55°$. Since the vertex dimension is simulated in GEANT, the correction include also the effect of the uncertainty in the interaction vertex position. The corrections are shown in Figure A.2.

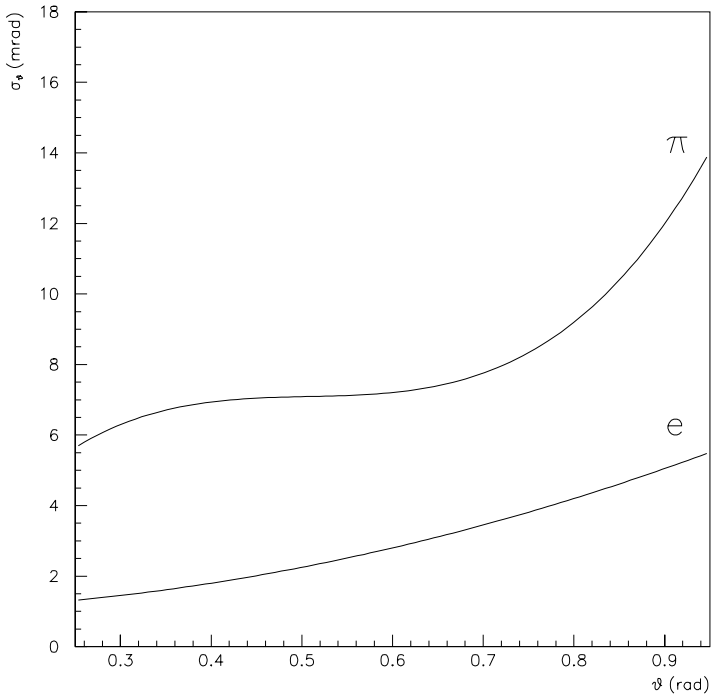

Figure A.2: parametrization of MS correction used in the kinematic fit analysis for $e^{\pm}$ and $\pi^{\pm}$.

Appendix B

Tracking Stability

The $J/\psi\pi^+\pi^-$ channel analysis depends on the behavior of the inner tracking system during data taking. The number of identified events in this channel can vary if the number of θ and ϕ lines is not stable over all the runs.

The number of θ and ϕ lines in the sample after the mdst and EW preselections and for selected $J/\psi\pi^+\pi^-$ events, selected with the kinematic fit analysis, is shown in Figure B.1. These numbers are stable after stack 5 but are both a little higher for lower stack numbers, this effect being mainly due to the different calibration of the detectors during the first period of data taking. This do not affect the number of $J/\psi\pi^+\pi^-$ events, in comparison with other stacks, as shown in Table 4.3.

The number of dead channels in the fiber detector can vary due to loss of VLPC channels or broken QPA02 cards. The number of dead channels is shown in Table B.1. In stack 50 the element number 22 of H2$'$ was not connected. These effects have been taken into account in the Monte Carlo evaluation of the selection efficiency of $J/\psi\pi^+\pi^-$, whose results are summarized in Table 5.4.

Stack	Layer 1	Layer 2	Layer 3	Layer 4
1	32	18	73	80
2	32	18	73	80
14	17	7	56	63
29	18	6	54	59
30	18	6	54	59
49	19	8	62	60
50	19	7	77	73
51	18	7	69	63
51	27	7	86	84

Table B.1: Number of dead channels in the fiber detector for each ψ' stack divided by layers.

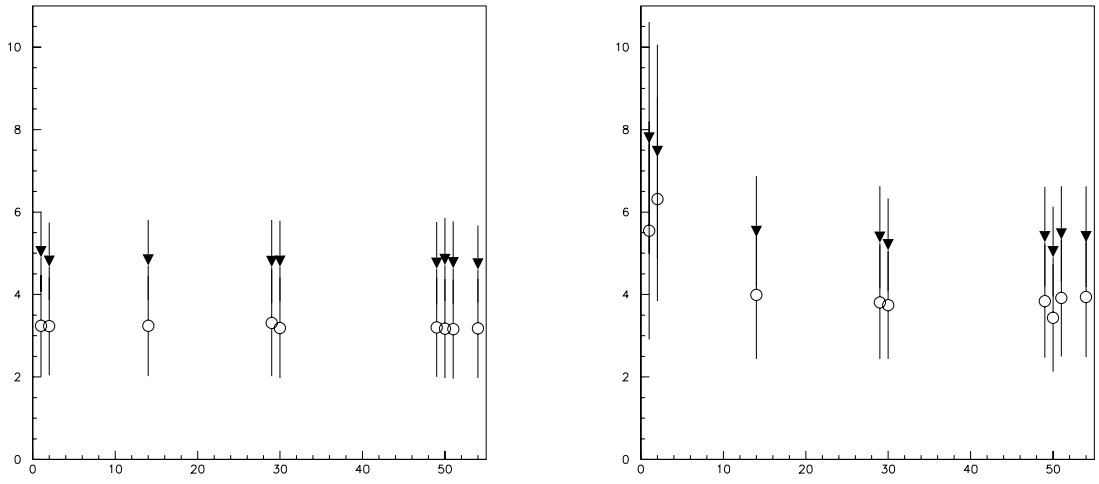

(a) (b)

Figure B.1: Number of (a) θ and (b) ϕ lines vs stack. Open circle: sample after mdst preselection and $EW_1 \cdot EW_2 > 1.5$ cut; filled triangle: $J/\psi\pi^+\pi^-$ selected events. The number of θ and ϕ lines for $J/\psi\pi^+\pi^-$ events is larger than 4 because of spurious hits in fibers and straws originating false tracks.

B.1 Stack 51

At the end of stack 51 (runs 7257 to 7259) the VLPC temperature increased and this can cause changes in the ADC signals. It has been noticed that the average number of fibers' ADC signals[1] per event is decreased. This suggested the possibility of a loss of efficiency of the fiber tracker. In these runs, the average number of fibers' TDC hits did not change significantly.

In the normal running conditions, the number of ADC signals is higher than the number of TDC hits, as shown in Figure B.2. The excess of ADC signals is mainly due to fiber signals with small ADC value: if only the ADC signals above a given threshold are considered, as shown in Figures B.3 and B.4, the two running conditions before and after VLPC warm up show similar behavior.

Let's now sketch how the detection of a charged θ line is done:

- only the fibers presenting both ADC signals and TDC hits have been considered in the formation of the fibers clusters (groups of adjacent fiber hits);
- charged θ lines are built using the fiber clusters and requiring at least one cluster in each one of the two (inner and outer) fiber detectors.

The number of clusters for each fiber layer remains almost constant, as shown in Figure B.5 (with a small exception for layer 1) and the distribution of the number of θ lines is compatible for the two running conditions.

The efficiency of the four layers can be checked using $e^{\pm}$ tracks. Table B.2 shows that the first layer presents a remarkable inefficiency but for the remaining layers the efficiency loss is around $2 \div 3\%$. This suggest that the main loss of ADC signals is due to the loss of spurious hits and the charged track detection efficiency is less affected.

Table B.3 shows the number of events found for the two sets of data in stack 51 and seems to suggest a $\sim 20\%$ loss of $J/\psi\pi^+\pi^-$events for the last three runs. However, the total number of events of the whole stack is compatible with the other stacks, as shown in Table 4.3 and the number of $J/\psi\pi^+\pi^-$events in the two subsamples is compatible within 2σ. For this reason it has been decided to use the whole stack without specific prescriptions.

[1] An ADC signal corresponds to the pedestal subtracted ADC value.

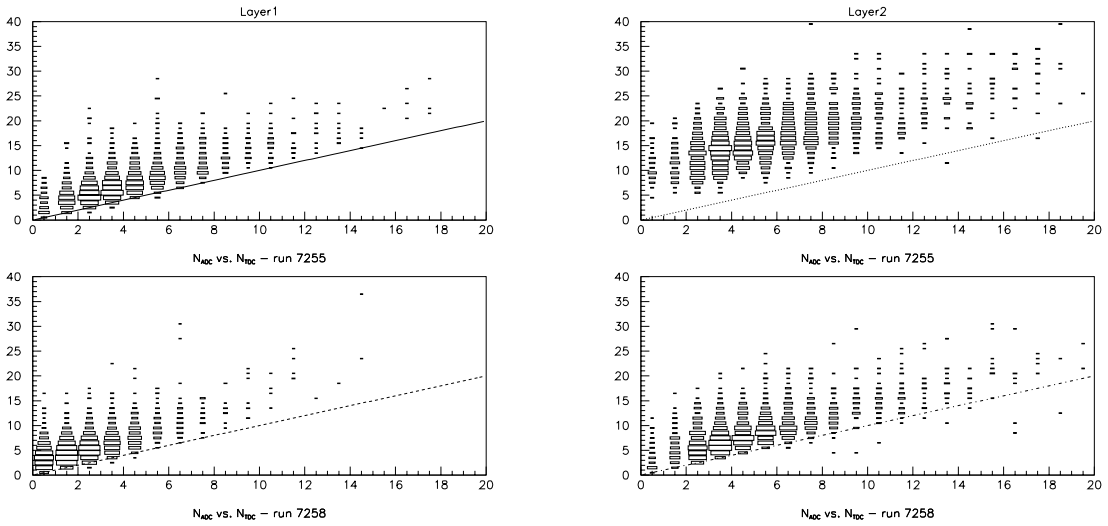

(a) (b)

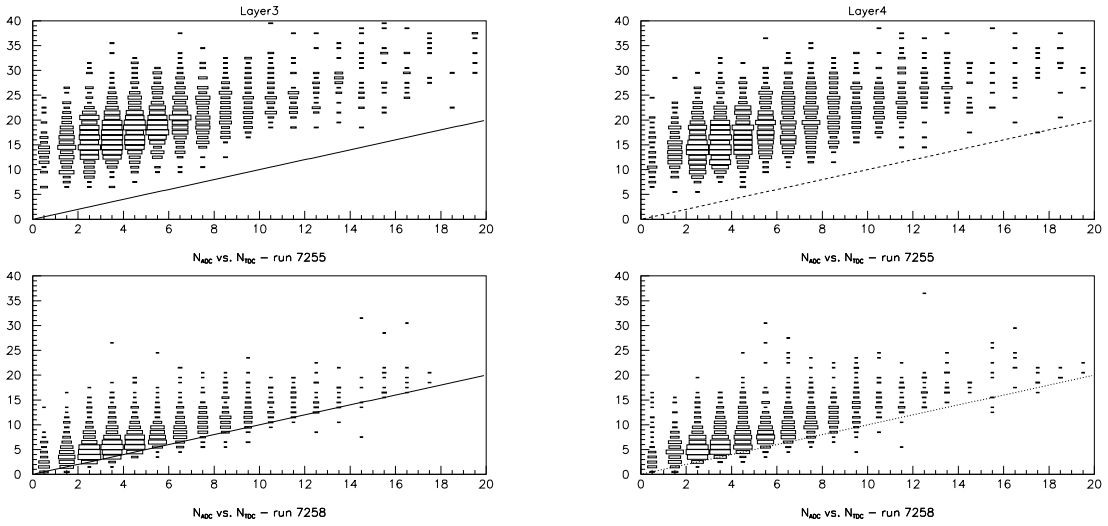

(c) (d)

Figure B.2: Comparison of the number of ADC signals versus TDC hits for run 7255 (top) and 7258 (bottom) in the four layers (a - d) of scintillating fibers. The dotted line is $N_{ADC} = N_{TDC}$.

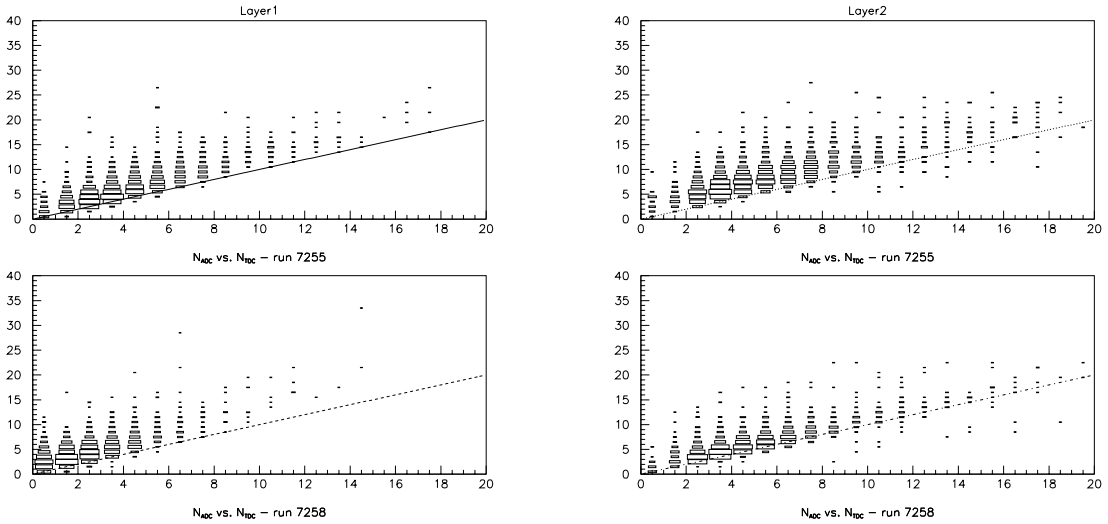

(a)

(b)

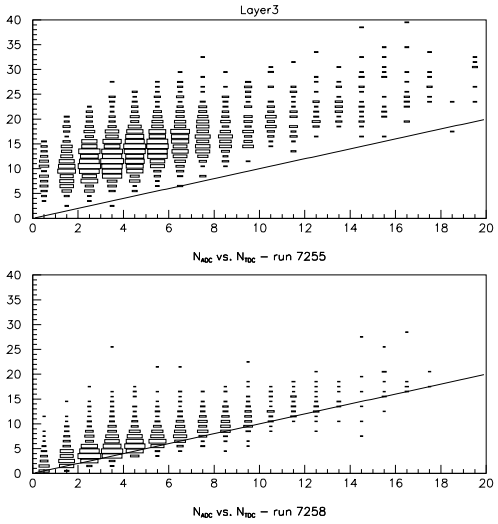

(c)

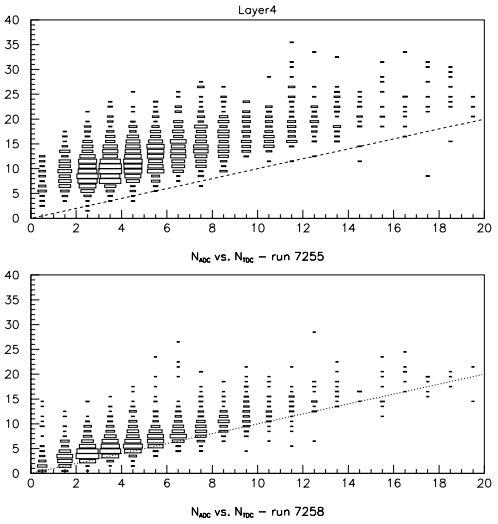

(d)

Figure B.3: Comparison of the number of ADC signals, with threshold at 0.1 mips, versus TDC hits for run 7255 (top) and 7258 (bottom) in the four layers (a - d) of scintillating fibers. The dotted line is $N_{ADC} = N_{TDC}$.

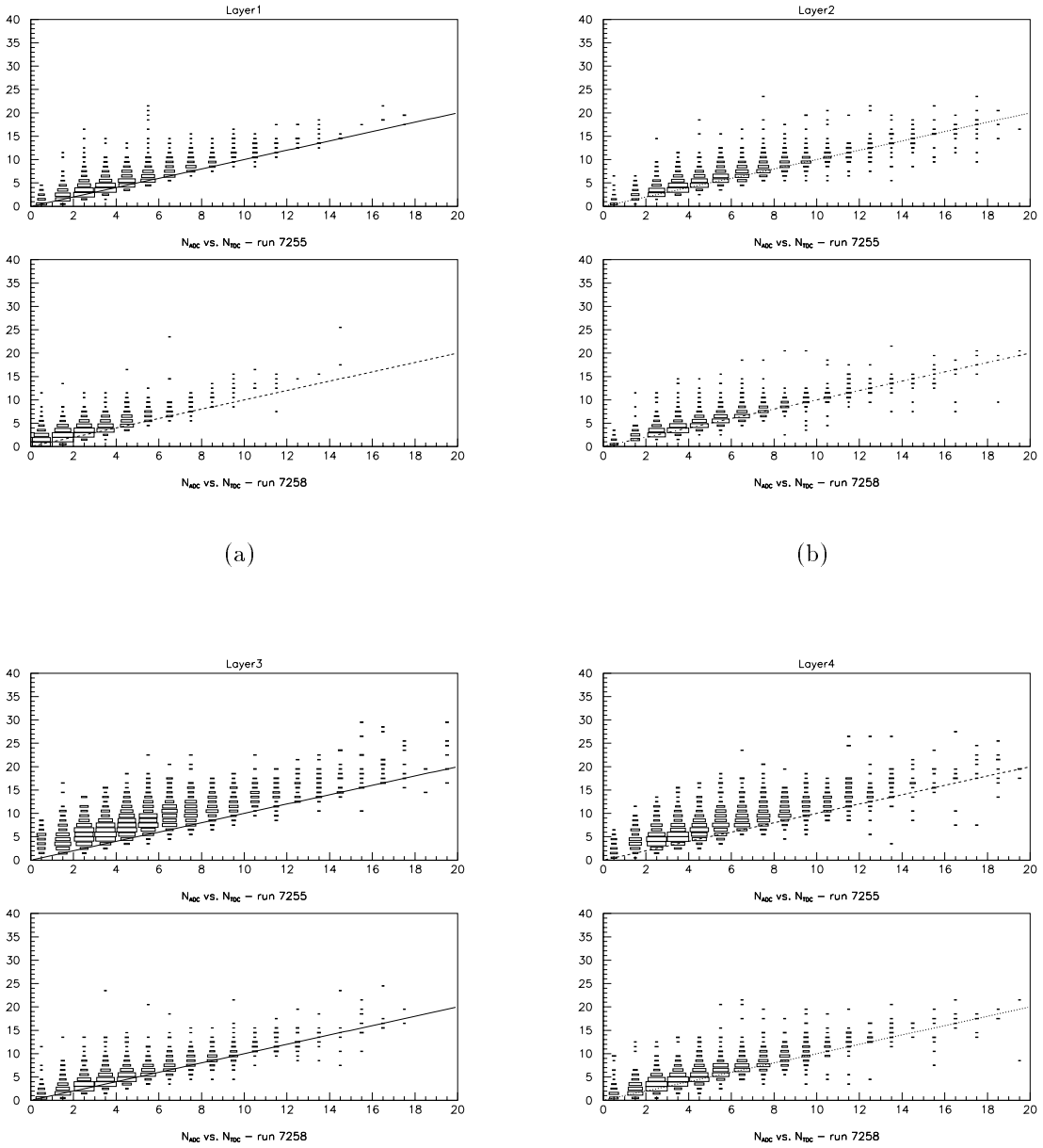

Figure B.4: Comparison of the number of ADC signals, with threshold at 0.2 mips, versus TDC hits for run 7255 (top) and 7258 (bottom) in the four layers (a - d) of scintillating fibers. The dotted line is $N_{ADC} = N_{TDC}$.

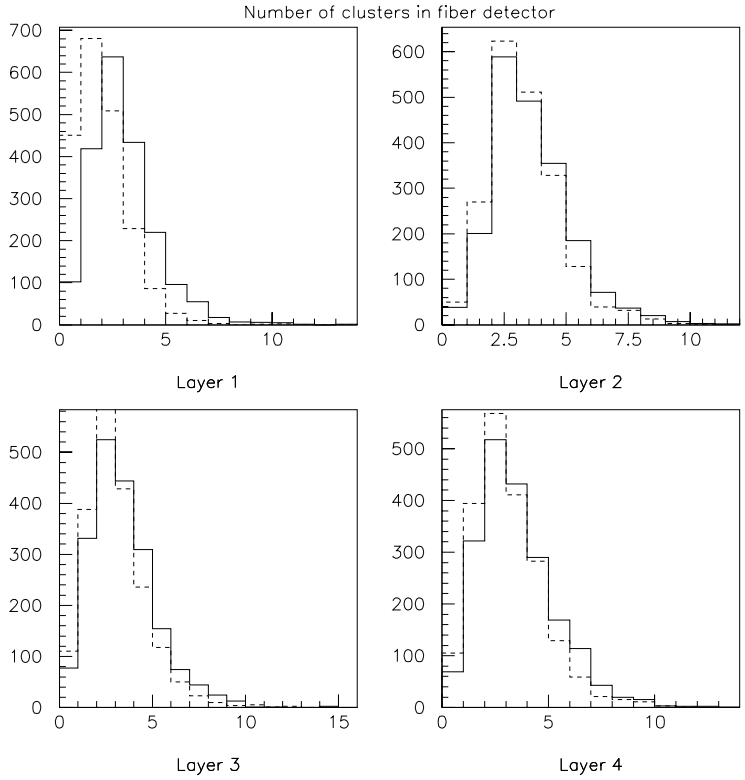

Figure B.5: Number of clusters in the four layers of the fiber detector. Solid line: run 7255, dotted line: run 7258.

Run	7254 - 7256	7257 - 7259
Layer 1	0.732 ± 0.006	0.593 ± 0.007
Layer 2	0.926 ± 0.004	0.908 ± 0.004
Layer 3	0.789 ± 0.006	0.765 ± 0.006
Layer 4	0.793 ± 0.005	0.763 ± 0.006

Table B.2: Efficiency of the four scintillating fiber layers for the two data sets in stack 51, measured with $e^{\pm}$ tracks.

Runs	$N(J/\psi\pi^+\pi^-)$	$N(ee_{tot})$	$\frac{N(J/\psi\pi^+\pi^-)}{N(ee_{tot})}$
7254 - 7256	416	2820	0.148 ± 0.007
7257 - 7259	284	2481	0.114 ± 0.006

Table B.3: Number of $J/\psi\pi^+\pi^-$ events compared to the number of ee_{tot} events detected in stack 51, before and after VLPC heating.

Appendix C

The Electron Weight

The selection of charmonium events, in the huge hadronic background produced in $\bar{p}p$ interaction, can be done by looking for high invariant mass e^+e^- due to charmonium electromagnetic decay. To do so we need a good electron and positron identification method, separating electron tracks from hadronic signals as well as e^+e^- pair due to γ conversions in the beam pipe or coming from Dalitz decay of the π^0.

The detectors that can provide useful information to do this are basically the hodoscopes (H1, H2$'$ and H2), measuring the energy loss into the plastic scintillator, the Čerenkov counter, whose threshold is designed to be above the $\pi^{\pm}$ maximum momentum and CCAL, whose cluster shape is different for single $e^{\pm}$ or pairs.

The electron weight (EW) is the method used by E835 to tag electrons and positrons based on the Neyman Pearson test, also known as the method of the likelihood ratios. From a set of measured quantities $(x_1, ..., x_n)$ of a given event it is possible to determine whether the event belongs to a class A or to a class B by comparing the two likelihood functions $\mathcal{L}_{\mathcal{A}}$ and $\mathcal{L}_{\mathcal{B}}$. We can define:

$$\rho(x_1, ..., x_n) = \frac{\mathcal{L}_{\mathcal{A}}(x_1, ..., x_n)}{\mathcal{L}_{\mathcal{B}}(x_1, ..., x_n)}, \tag{C.1}$$

and if the classes A and B correspond to electrons and background hypothesis, ρ is the electron weight of the charged line.

The variables used to evaluate the EW are:

- H1 energy deposit (corrected by θ angle);
- H2 energy deposit (corrected by θ angle);
- H2$'$ energy deposit (corrected by θ angle);
- Čerenkov pulse height (corrected by θ angle and mirror photoelectron yield);
- CCAL cluster second moment along wedges and rings in a 3×3 blocks area;

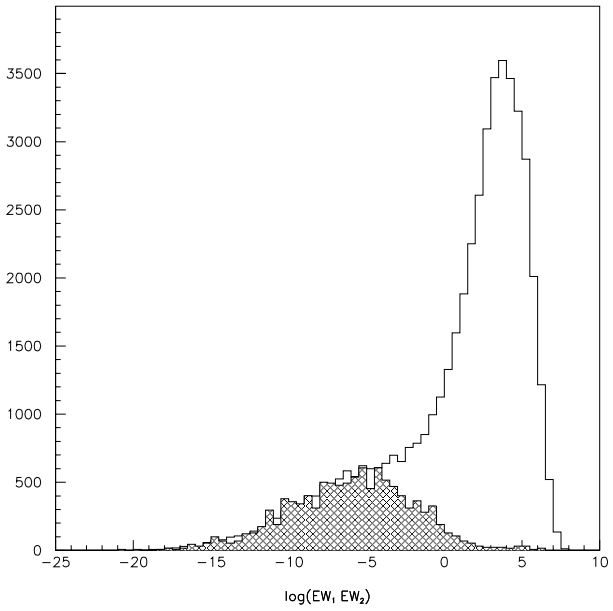

Figure C.1: $\log(EW_1 \cdot EW_2)$ distribution for e^+e^- candidates after the mdst preselection for data at the ψ' energy (open area) and for a background point (cross hatched area) scaled with the luminosity.

- ratio of the energy deposit in a 3×3 block matrix divided by that in a 5×5 block matrix;
- ratio of the energy deposit in a 2×2 block matrix divided by that in a 4×4 block matrix;
- CCAL cluster mass, defined as:

$$M_{cl} = \sqrt{\left(\sum E_i\right)^2 - \left(\sum \vec{p}_i\right)^2},$$

  where the sum is over a 5×5 block matrix, E_i is the energy deposition in the i^{th} CCAL block and $\vec{p}_i = E_i\vec{r}_i$ with $\vec{r}_i$ the unit vector from the interaction point to the center of the i^{th} block.

All the tracks without a Čerenkov signal above pedestal are not associated to electrons. The distribution of the product of the EW for the two e^+e^- candidates is shown in Figure C.1.

In the offline analysis of the events, there is a threshold on M_{cl}. All the clusters with M_{cl} higher than this threshold value are splitted. For $e^{\pm}$ coming from charmonium decay, the M_{cl} threshold is set at 120 MeV. This is determined by selecting a

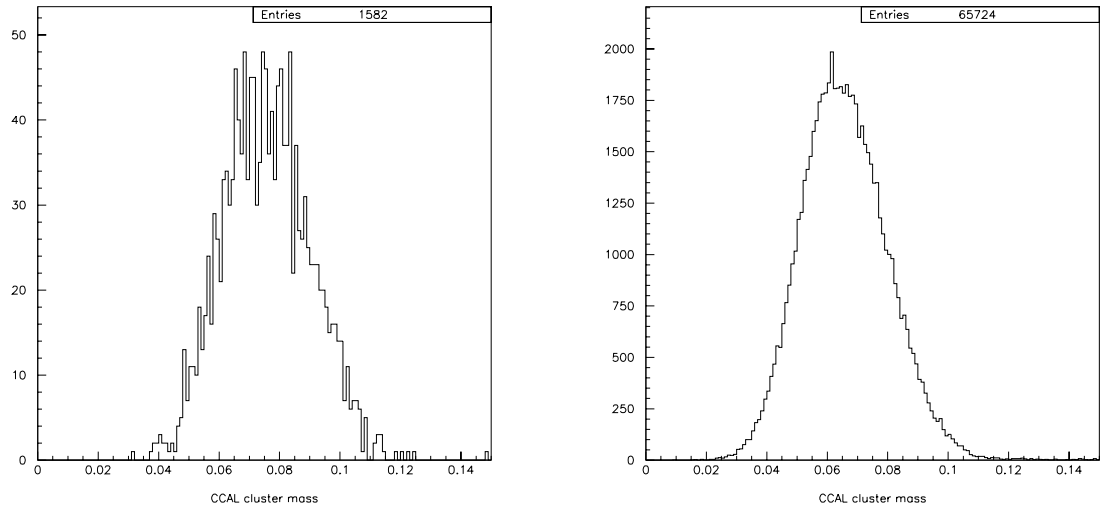

(a) (b)

Figure C.2: (a) M_{cl} distribution for the e^+e^- exclusive events, selected as explained in the text and (b) M_{cl} distribution for all the e^+e^- events in the detector fiducial region ($15° < \theta_{e^\pm} < 60°$) selected with $EW_1 \cdot EW_2 > 1.5$ cut only (2 entries per event).

clean e^+e^- exclusive sample [1] by using the inner tracking only and looking at the M_{cl} distribution for the CCAL clusters associated to the charged tracks (see Figure C.2 (a)). Figure C.2 (b) shows the M_{cl} distribution for all the e^+e^- events in the detector fiducial region selected with EW cut only. The EW efficiency depends on the choice of the M_{cl} splitting threshold.

C.1 Electron weight cut efficiency

All the events with electrons and positrons of physical interest for E835 have a e^+e^- pair in the detector acceptance, so it is reasonable to use the product of EW of the two candidates e^+e^- tracks to select the events.

The optimal $EW_1 \cdot EW_2$ cut, with high background rejection and high efficiency, is determined by comparison of a clean data sample with a background sample, as shown in Figure C.1. In this analysis it $EW_1 \cdot EW_2 > 1.5$ is used (corresponding to

[1] The selection is done by requiring that the highest invariant mass from two CCAL clusters is greater than 3.3 GeV. In addition, the event must have exactly 2 θ and 2 ϕ lines, satisfying the e^+e^- kinematics.

$\log(EW_1 \cdot EW_2) > 0.176$).

ϵ_{EW} can be measured directly from the data by selecting a clean sample of e^+e^- due to charmonium decay. Anyway, each channel will have a different ϵ_{EW} because of its specific features.

As said before, the EW is calibrated to distinguish between pairs and single $e^\pm$ by using the pulse height information in the hodoscopes and the Čerenkov. When other charged particles out of the e^+e^- are present in the final state, as it is the case of $J/\psi\pi^+\pi^-$, if they hit the same hodoscope element hit by the $e^\pm$, the energy deposition in the scintillator will be larger than expected and this cause a decrease of ϵ_{EW} for this channel.

Since the EW is calculated also using information about the CCAL cluster shape, in the case of $J/\psi\pi^0\pi^0$ and $J/\psi\eta$, the presence of additional photons in the proximity of a $e^\pm$ cluster can affect the shape of the clusters in the CCAL and so the ϵ_{EW} could be lower. To avoid corrections for this effect, in this analysis only events in which all the γ have an angular separation from both $e^\pm$ larger than 100 mrad are accepted.

For the measurement of ϵ_{EW} for all the channels we need to select a clean sample of events without using the EW. The largest source of background comes from $\overline{p}p \to \pi^0\pi^0$ (or $\eta\eta$) $\to 4\gamma$, where the signal in the hodoscopes and Čerenkov can be due to photon conversions or Dalitz decay.

To minimize the possibility of such a contamination, the invariant mass of both $e^\pm$ candidates with all the others CCAL and FCAL clusters have been calculated. Figure C.3 (a) show the $m_{e\gamma}$ distribution of the candidate pair with invariant mass nearest to π^0 or η mass, for all the mdst sample. The event is rejected if the $e^\pm$ candidate presents a potential π^0 ($80 < m_{e\gamma} < 180$ MeV) or η ($450 < m_{e\gamma} < 650$ MeV) contamination. The e^+e^- invariant mass distribution of the events after the selection is shown in Figure C.3 (b).

ϵ_{EW} is measured using the subsample selected in this way; it has been measured for all the channels by selecting the event samples in the same way described in Section 4.3, without using the EW cut but applying a 1% cut on the kinematic fit probability. The distributions of $EW_1 \cdot EW_2$ obtained are shown in Figure C.4; the results are summarized in Table C.1.

As expected, even if $J/\psi\pi^0\pi^0$ and $J/\psi\eta$ have poor statistics, all the $\epsilon_{EW}(J/\psi + neutrals)$ values are compatible so the most precise evaluation, $\epsilon_{EW}(e^+e^-)$, can be used for all these channels.

We expect also that $\epsilon_{EW}(J/\psi\pi^+\pi^-)$ should be consistent with $\epsilon_{EW}(J/\psi + neutrals)$ when the angular separation of $\pi^\pm$ from $e^\pm$ is large. This can be checked by dividing the previous $J/\psi\pi^+\pi^-$ sample in two subsamples: (a) in which both pions are at $\Delta\phi > 300$ mrad from $e^\pm$ tracks; (b) containing events with at least one $\pi^\pm$ at $\Delta\phi < 300$ mrad from an $e^\pm$. The efficiencies for the two subsamples are $\epsilon_{EW}(\mathrm{a}) = 0.932 \pm 0.009$ and $\epsilon_{EW}(\mathrm{b}) = 0.811 \pm 0.018$, in agreement with expectations.

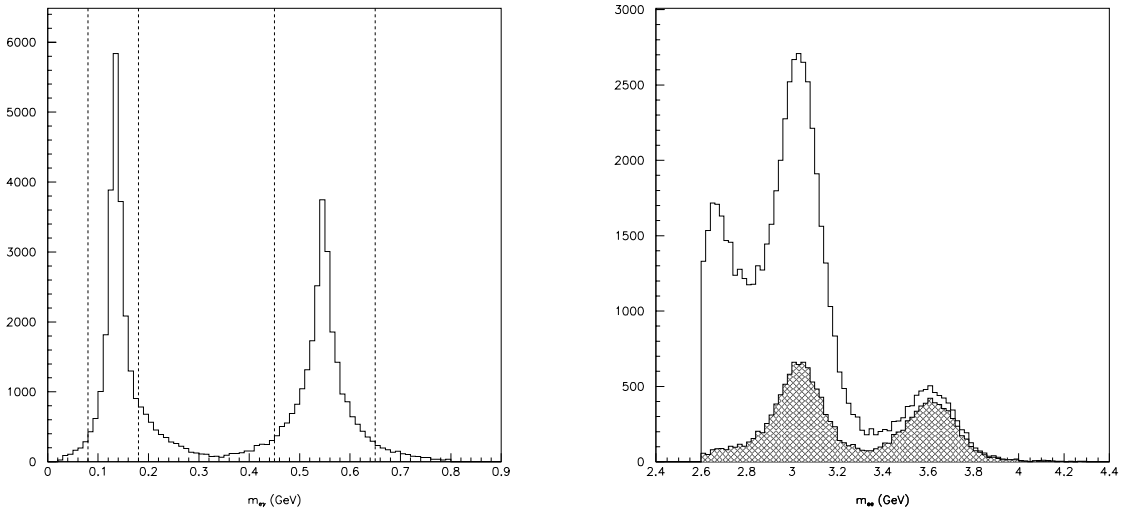

(a) (b)

Figure C.3: (a) $m_{e\gamma}$ distribution for the CCAL or FCAL cluster forming with the $e^{\pm}$ track an invariant mass close to a π^0 or a η. The events within the dashed lines (π^0 and η peaks) are rejected. The e^+e^- invariant mass in the whole mdst sample (solid line) and after the rejection (cross hatched area) are shown in (b).

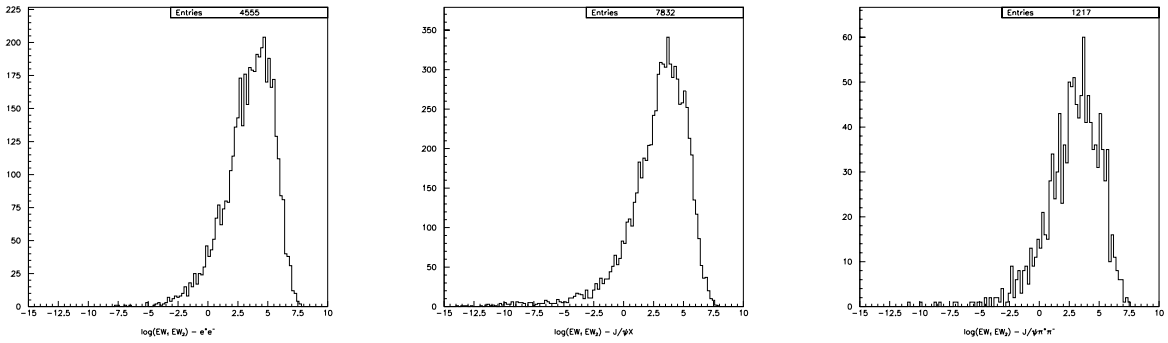

(a) (b) (c)

Figure C.4: $\log(EW_1 \cdot EW_2)$ distribution for (a) e^+e^-, (b) $J/\psi X$ and (c) $J/\psi\pi^+\pi^-$ events, selected with kinematic fit analysis, on the subsample of Figure C.3(b).

	N_{sample}	N_{EW}	ϵ_{EW}
e^+e^-	4555	4231	0.929 ± 0.004
$J/\psi X$	7832	6916	0.883 ± 0.004
$J/\psi\pi^+\pi^-$	1217	1079	0.887 ± 0.009
$J/\psi\pi^0\pi^0$	90	85	0.944 ± 0.024
$J/\psi\eta$	159	149	0.937 ± 0.019

Table C.1: ϵ_{EW} for all channels.

C.2 Summary

We have three values for EW efficiency for different channels when cutting at $EW_1 \cdot EW_2 > 1.5$. The efficieny ratios that are used in the analysis are:

$$\frac{\epsilon_{EW}(e^+e^- + X)}{\epsilon_{EW}(e^+e^- + neutrals)} = 0.950 \pm 0.006 \quad \text{(C.2)}$$

$$\frac{\epsilon_{EW}(e^+e^- + X)}{\epsilon_{EW}(e^+e^- + \pi^+\pi^-)} = 0.995 \pm 0.011 \quad \text{(C.3)}$$

$$\frac{\epsilon_{EW}(e^+e^- + \pi^+\pi^-)}{\epsilon_{EW}(e^+e^- + neutrals)} = 0.955 \pm 0.011 \quad \text{(C.4)}$$

Appendix D

Extra Clusters

In some cases, the events selected contain one or more extra CCAL clusters, namely a cluster which is not associated to any of the particles used for the event reconstruction. The timing classification of CCAL clusters have been discussed in Section 3.6.1; the events are never rejected because of the presence of out-of-time or undetermined extra clusters. The possibility to reject events with extra on-time clusters is discussed here.

For good events, the presence of extra clusters can be due to:

- background events at the same time of a good event (pile-up). The time window for on-time clusters in CCAL is $\tau = 20$ ns, so the background pile-up effect is of the order of:

$$\mathcal{L} \cdot \tau \cdot \sigma_{\overline{p}p}(3686 \text{ MeV}) \approx 2 \div 3 \ \% \tag{D.1}$$

  depending on the luminosity $\mathcal{L}$;

- extra clusters due to $e^{\pm}$ or γ, originally in an electromagnetic shower in the calorimeters, that escape the original shower and hit the calorimeter in other locations (back-splash). The expected amount of such events can be evaluated with the GEANT Monte Carlo, producing a clean sample of events (with no background superimposition). For $\psi' \to e^+e^-$ about 7% of the events have additional clusters with energy above 50 MeV, which is the energy threshold used for CCAL clusters detection in this thesis. The extra cluster energy distribution is shown in Figure D.1.

The possibility of clusters due to bremsstrahlung photons, emitted by the $e^{\pm}$, is taken into account by always accepting extra clusters forming an angle $\theta_{e\gamma} < 100$ mrad with the $e - \gamma$ invariant mass $m_{e\gamma} < 100$ MeV.

If a rejection of events with extra clusters is applied, the total efficiency will include an additional term ϵ_{pu-bs}, of the order of few percent smaller than 100%. This efficiency will cancel in the evaluation of ratios of BR for exclusive channels,

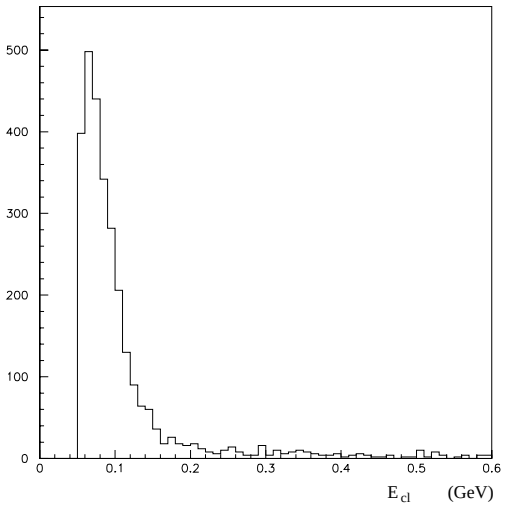

Figure D.1: Energy distribution for the extra clusters in CCAL for e^+e^- GEANT events, produced with no background. A large fraction of the extra clusters have an energy smaller than 150 MeV but a tail at higher energies is also present (CCAL clusters are detected if their energy is greater than 50 MeV, which appears as low energy threshold in the plot).

but the cut can not be applied in the case of inclusive J/ψ selection. In the analysis described in this thesis no cuts on the number of extra calorimeter clusters is used, this choice have been tested in more detail on e^+e^- exclusive events.

D.1 e^+e^- exclusive events

The only channel for which it is relatively easy to study the effect of the cut on the number of extra clusters, and relate it to the pile-up of background events, is the $\psi' \to e^+e^-$.

The total energy for a single reaction in the laboratory is:

$$E_{lab} = \gamma E_{cm} = 7243 \text{ MeV}.$$

If a background event superimpose to a good e^+e^- event, the total energy measured by the calorimeters will be larger. Figure D.2 shows the distribution of the total energy in the laboratory system measured by both CCAL and FCAL for e^+e^- events (selected as explained in Chapter 4). In this case the total energy of the event is measured and it is easy to see the peak of clean e^+e^- events with the tail at higher energies, corresponding to additional energy depositions in coincidence with the event, due to pile-up. Among the events with additional clusters, the ones with total

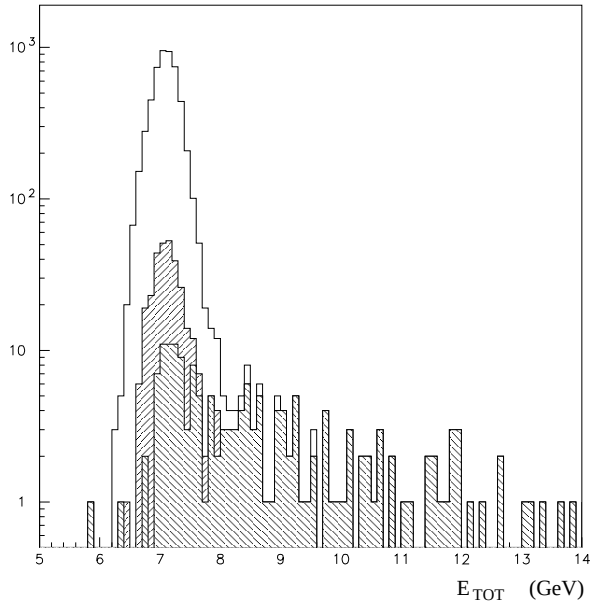

Figure D.2: Distribution of the total energy in the laboratory syste, measured in both CCAL and FCAL, for e^+e^- events (the sum is made over the on-time clusters only). The open area is obtained with no cuts on the number of extra clusters; the two hatched areas are the events with at least one extra cluster of energy greater than 50 MeV and 150 MeV. Almost all the pile-up clusters have $E > 150$ MeV. The extra clusters with $E < 150$ MeV are mainly due to back-splash.

energy falling below the main peak are mainly due to secondary clusters, originated by back-splash.

The fraction of events rejected by a cut on the presence of extraclusters with energy greater than 50 MeV is $7.6 \pm 0.4\%$ (405/5298); at 150 MeV is $3.3 \pm 0.2\%$ (174/5298), which is consistent with the two effects considered.

The $(e^{\pm} - extra\ cluster)$ invariant mass distribution for exclusive e^+e^- events is shown in Figure D.3. Even without rejection of events with extra clusters there is no evidence of contamination of the events from π^0.

A cut on extra clusters will therefore reject good events at the level of few percent with no sensible background reduction, for this reason it is not applied in this thesis.

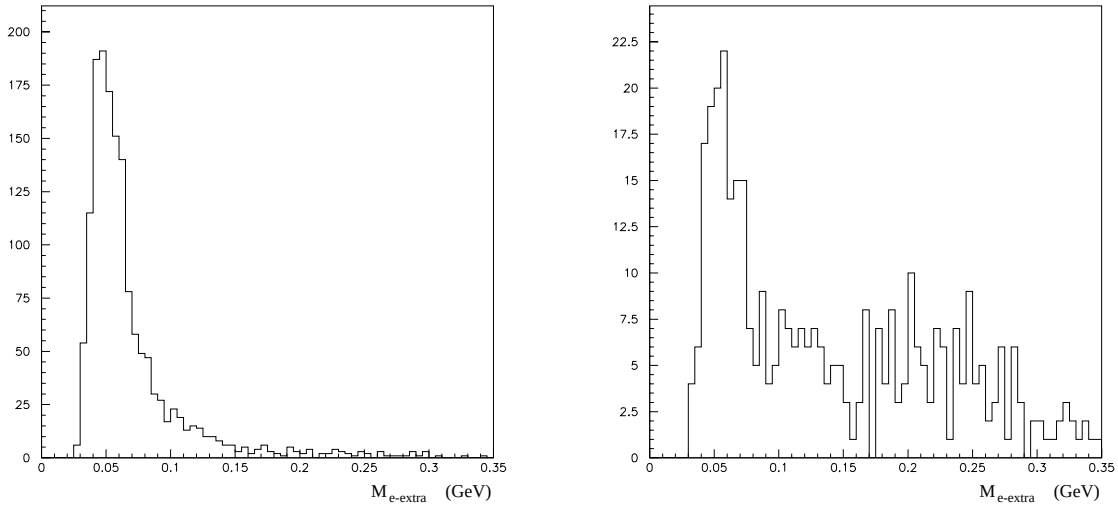

(a) (b)

Figure D.3: $(e^{\pm} - extra\ cluster)$ invariant mass distribution for (a) Monte Carlo and (b) data $\psi' \to e^+e^-$ events with one or more extra clusters. For each event it is plotted the invariant mass nearest to m_{π^0}. The Monte Carlo events are generated with GEANT and no background superimposition, so the additional clusters are due to back-splash. All the extra-clusters with $E > 50$ MeV have been considered.

Appendix E

Comparison Data - Monte Carlo

In this section several plots for the comparison of data and Monte Carlo samples, concerning the variables used for the event selection, are shown. The data distributions are represented by solid lines, the superimposed dots with error bars are the MC distributions, scaled with the number of events.

Figure E.1 shows the e^+e^- invariant mass distribution for all the 5 channels analyzed. Figure E.2 shows the behavior of the χ^2 probability distribution for all the kinematic fits. Figure E.3 shows the measured m_{π^0} and m_η distributions for $J/\psi\pi^0\pi^0$ and $J/\psi\eta$ events. Figures E.4 and E.5 show the measured angular and energy distributions for $\pi^\pm$ and γ used as input for the $J/\psi\pi^+\pi^-$ and $J/\psi\pi^0\pi^0$ kinematic fits. Figure E.6 shows the energy distribution and its dependence on θ for $\pi^\pm$ (due to $J/\psi\pi^+\pi^-$ decay) and γ ($J/\psi\pi^0\pi^0$) reconstructed with the kinematic fit.

The "pull" of a single measured variable x is defined as:

$$pull_x = \frac{x_{meas} - x_{fit}}{\sqrt{\sigma^2_{x,meas} - \sigma^2_{x,fit}}}, \tag{E.1}$$

the pull distribution for a set of measurements should be close to a gaussian centered in 0 and $\sigma = 1$. If the pull distribution is shifted relatively to zero, this means that a certain bias on the measurement is present; moreover, a broader distribution suggests an underestimation of the error on the measurement (on the contrary, if the distribution is narrower, the error is probably overestimated). Figures E.7 to E.14 show all the pulls distributions, comparing data and Monte Carlo, for all the variables used as input for the kinematic fits. The pulls of all the variables have been fit with a gaussian. The results are summarized in Table E.1.

		$\overline{x}$	σ_x	χ^2/ndf
e^+e^-				
$e^\pm$	E	-0.016 ± 0.011	1.039 ± 0.009	3.6
	θ	0.097 ± 0.010	0.965 ± 0.009	3.5
	ϕ	0.000 ± 0.011	1.131 ± 0.010	1.8
$J/\psi X$				
$e^\pm$	E	-0.079 ± 0.004	0.894 ± 0.004	19.8
	θ	-0.068 ± 0.004	0.769 ± 0.003	25.9
	ϕ	-0.017 ± 0.004	0.932 ± 0.004	15.2
$J/\psi\pi^+\pi^-$				
$e^\pm$	E	-0.095 ± 0.012	1.073 ± 0.011	3.3
	θ	0.080 ± 0.010	0.919 ± 0.014	8.4
	ϕ	0.002 ± 0.012	1.072 ± 0.015	7.3
$\pi^\pm$	E	-	-	-
	θ	0.119 ± 0.010	0.875 ± 0.014	10.5
	ϕ	0.005 ± 0.011	0.989 ± 0.013	6.1
$J/\psi\pi^0\pi^0$				
$e^\pm$	E	0.014 ± 0.022	0.999 ± 0.020	1.7
	θ	0.107 ± 0.025	1.193 ± 0.024	1.5
	ϕ	-0.010 ± 0.024	1.159 ± 0.021	1.2
γ	E	-0.003 ± 0.014	0.915 ± 0.016	4.2
	θ	0.076 ± 0.015	1.044 ± 0.014	1.8
	ϕ	0.000 ± 0.015	1.083 ± 0.013	1.2
$J/\psi\eta$				
$e^\pm$	E	-0.038 ± 0.037	0.917 ± 0.033	1.4
	θ	0.165 ± 0.040	1.016 ± 0.034	1.1
	ϕ	0.023 ± 0.050	1.259 ± 0.051	0.9
γ	E	-0.007 ± 0.040	1.003 ± 0.039	0.9
	θ	0.013 ± 0.038	0.968 ± 0.032	1.0
	ϕ	-0.031 ± 0.047	1.186 ± 0.044	1.0

Table E.1: Results of the gaussian fit of the pull distributions for all the variables used as input of the kinematic fits (data).

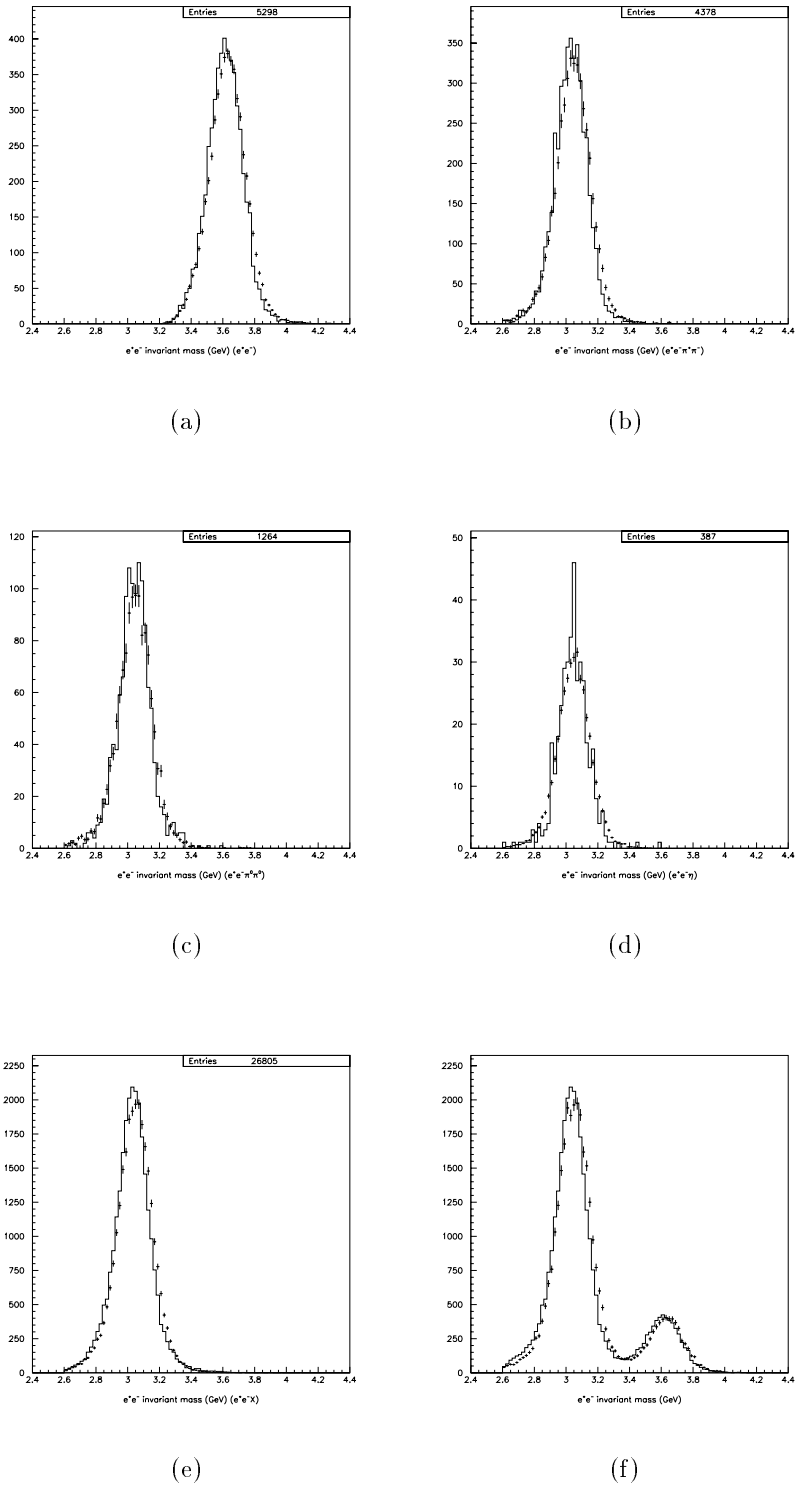

Figure E.1: e^+e^- invariant mass distribution for (a) e^+e^- exclusive, (b) $J/\psi\pi^+\pi^-$, (c) $J/\psi\pi^0\pi^0$, (d) $J/\psi\eta$, (e) $J/\psi X$ events and (f) all e^+e^- candidates. Data (solid line) and Monte Carlo (crosses) samples.

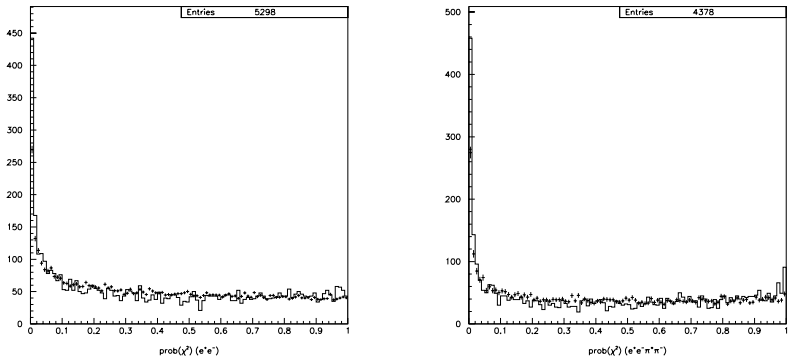

(a)

(b)

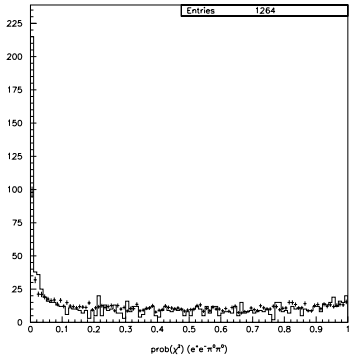

(c)

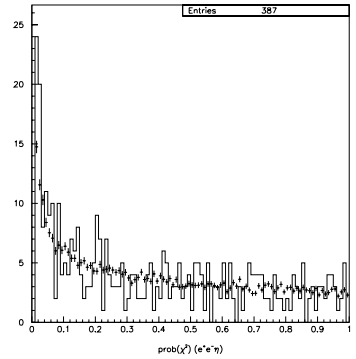

(d)

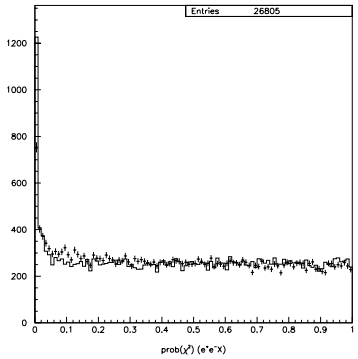

(e)

Figure E.2: Kinematic fit prob(χ^2) distribution for (a) e^+e^-, (b) $J/\psi\pi^+\pi^-$, (c) $J/\psi\pi^0\pi^0$, (d) $J/\psi\eta$ and (e) $J/\psi X$ events. Data (solid line) and Monte Carlo (crosses) samples.

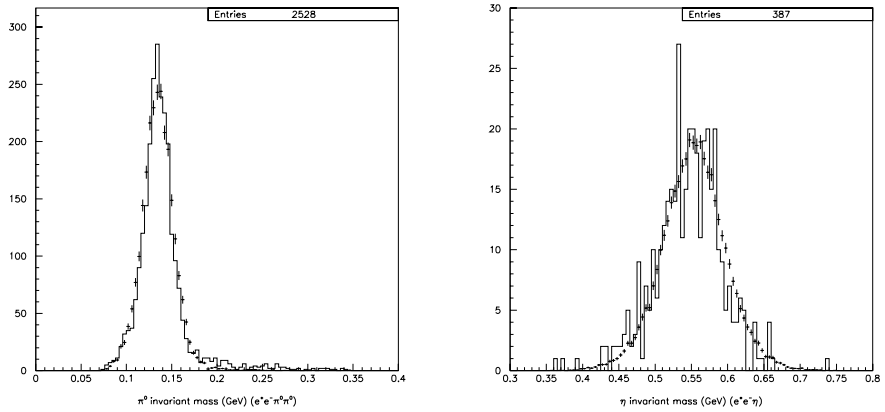

(a) (b)

Figure E.3: (a) m_{π^0} distribution for selected $J/\psi\pi^0\pi^0$ events (2 entries per event) and (b) m_η distribution for selected $J/\psi\eta$ events. Data (solid line) and Monte Carlo (crosses) samples.

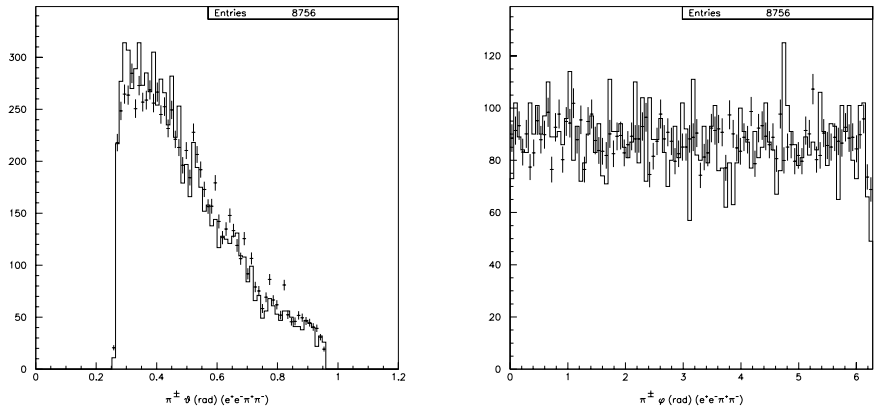

(a) (b)

Figure E.4: Measured angular distribution for pions for selected $J/\psi\pi^+\pi^-$ events. (a) θ_π and (b) ϕ_π. Data (solid line) and Monte Carlo (crosses) samples.

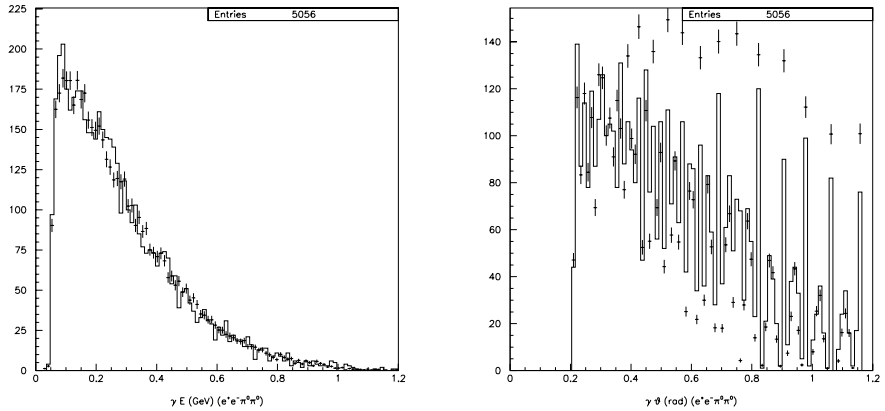

(a) (b)

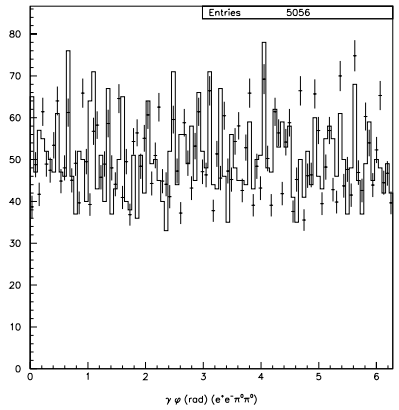

(c)

Figure E.5: Measured energy and angular distribution for photons for selected $J/\psi\pi^0\pi^0$ events. (a) E_γ, (b) θ_γ and (c) ϕ_γ. Data (solid line) and Monte Carlo (crosses) samples.

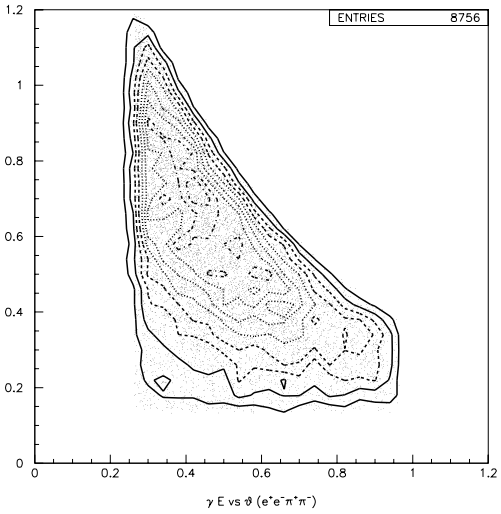

(a)

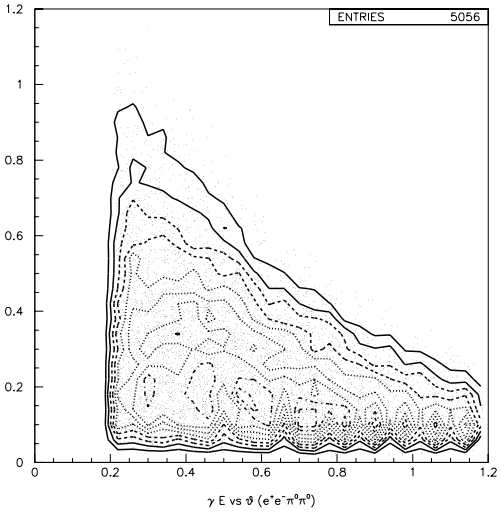

(b)

Figure E.6: Energy distribution versus θ for (a) pions for $J/\psi\pi^+\pi^-$ events and (b) photons for $J/\psi\pi^0\pi^0$ events. Dots represent real data; the superimposed contour plot show the behavior for MC events.

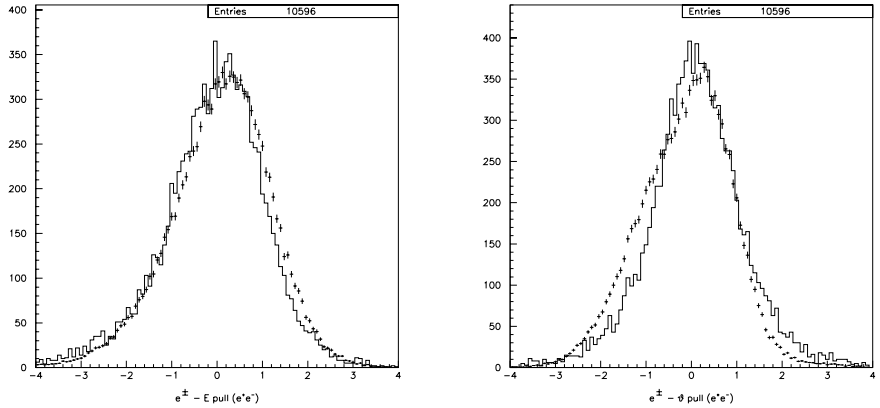

(a) (b)

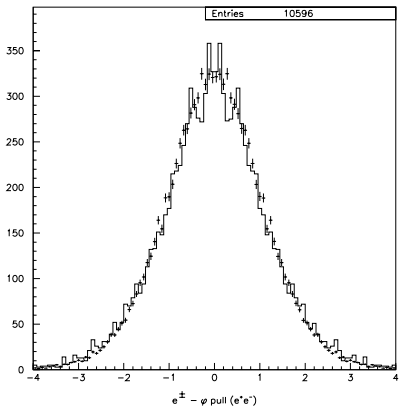

(c)

Figure E.7: (a) energy, (b) θ and (c) ϕ pull distribution for the $e^{\pm}$ after the e^+e^- kinematic fit selection. Data (solid line) and Monte Carlo (crosses) samples.

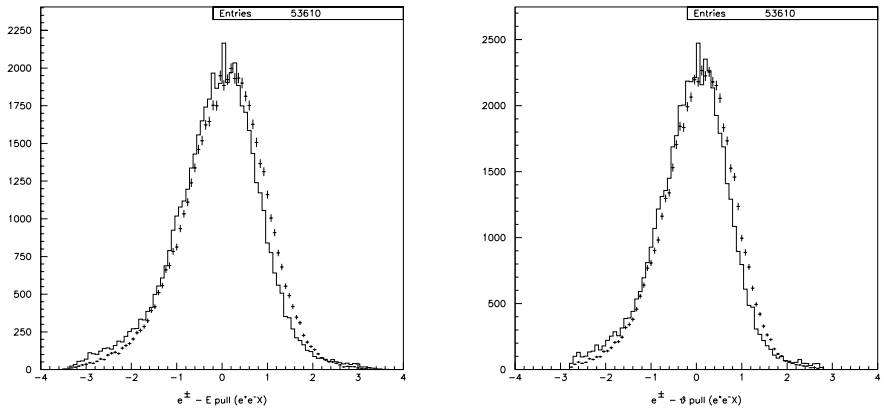

(a) (b)

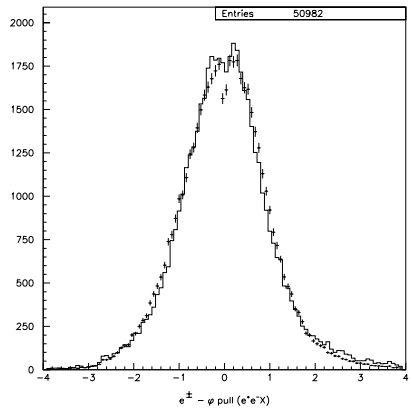

(c)

Figure E.8: (a) energy, (b) θ and (c) ϕ pull distribution for the $e^{\pm}$ after the $J/\psi X$ kinematic fit selection. Data (solid line) and Monte Carlo (crosses) samples.

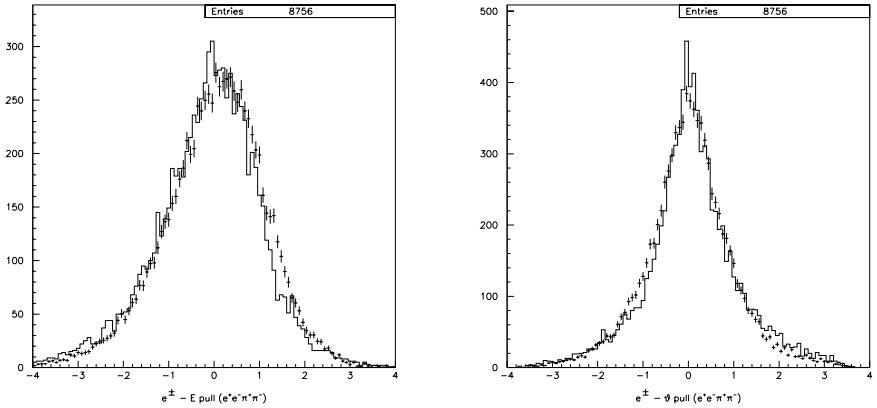

(a) (b)

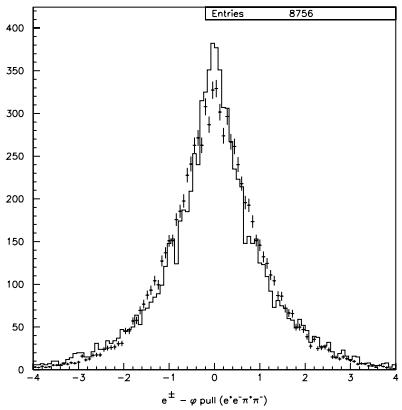

(c)

Figure E.9: (a) energy, (b) θ and (c) ϕ pull distribution for the $e^{\pm}$ after the $J/\psi\pi^+\pi^-$ kinematic fit selection. Data (solid line) and Monte Carlo (crosses) samples.

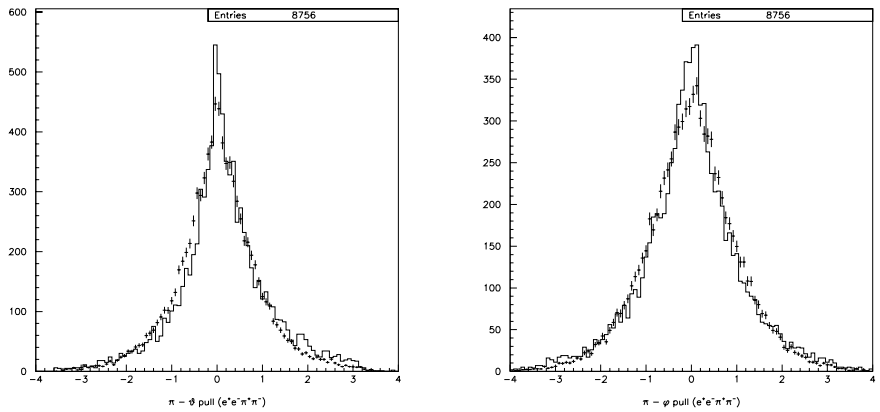

(a) (b)

Figure E.10: (a) θ and (b) ϕ pull distribution for the $\pi^{\pm}$ after the $J/\psi\pi^{+}\pi^{-}$ kinematic fit selection. Data (solid line) and Monte Carlo (crosses) samples.

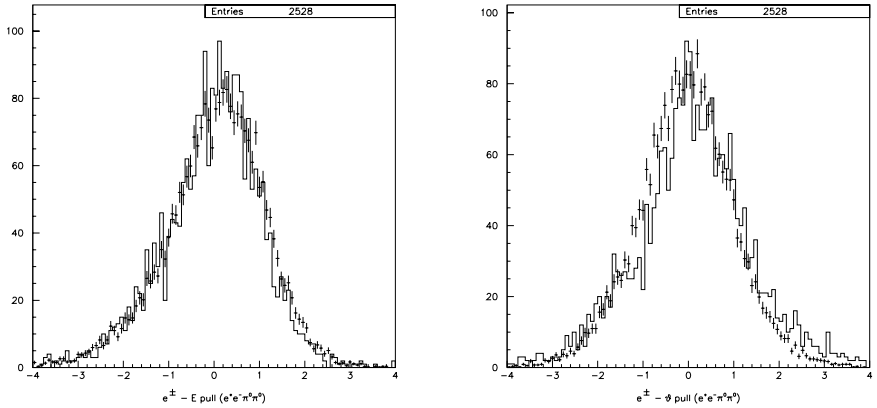

(a) (b)

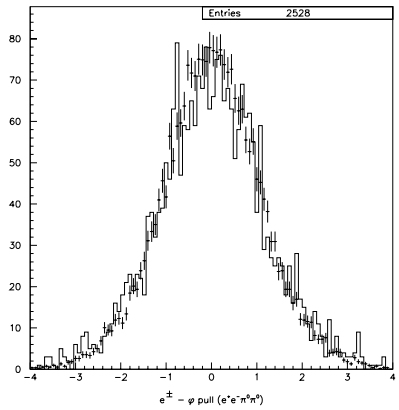

(c)

Figure E.11: (a) energy, (b) θ and (c) ϕ pull distribution for the $e^{\pm}$ after the $J/\psi\pi^0\pi^0$ kinematic fit selection. Data (solid line) and Monte Carlo (crosses) samples.

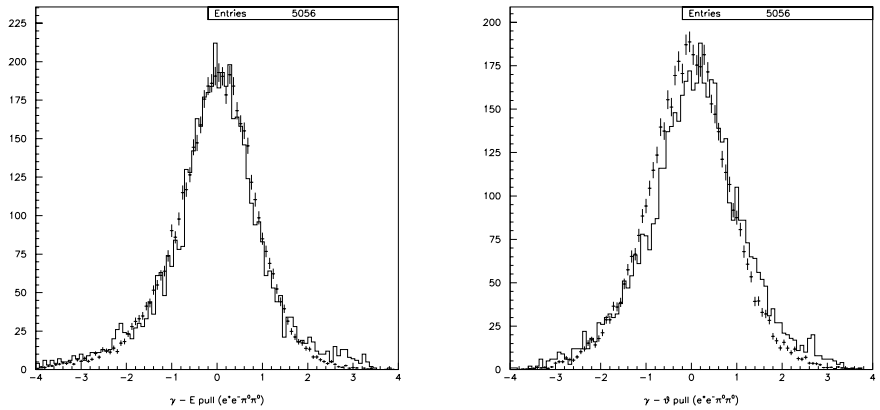

(a) (b)

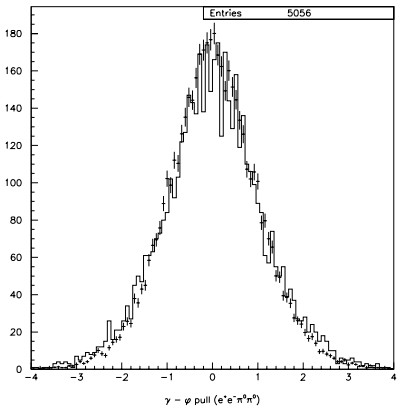

(c)

Figure E.12: (a) energy, (b) θ and (c) ϕ pull distribution for the γ after the $J/\psi\pi^0\pi^0$ kinematic fit selection. Data (solid line) and Monte Carlo (crosses) samples.

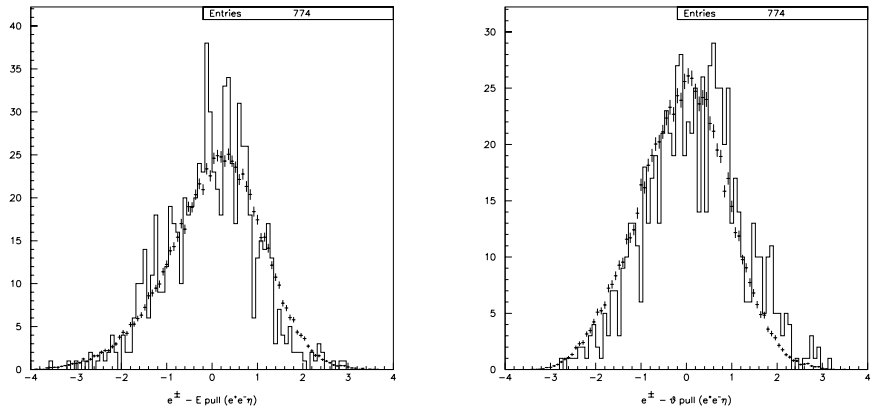

(a) (b)

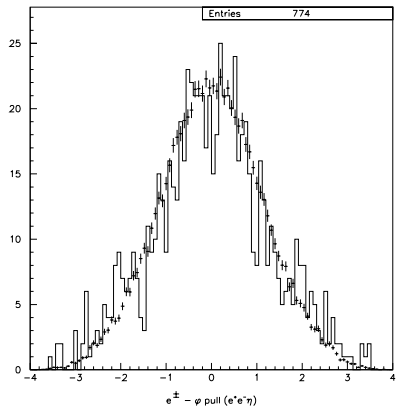

(c)

Figure E.13: (a) energy, (b) θ and (c) ϕ pull distribution for the $e^{\pm}$ after the $J/\psi\eta$ kinematic fit selection. Data (solid line) and Monte Carlo (crosses) samples.

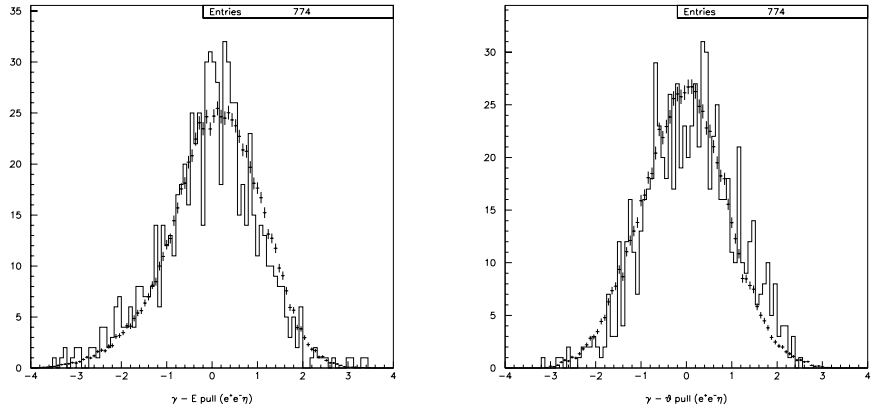

(a) (b)

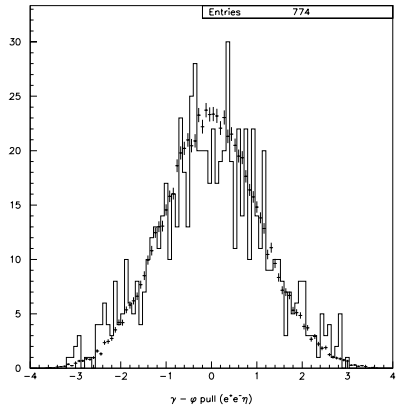

(c)

Figure E.14: (a) energy, (b) θ and (c) ϕ pull distribution for the γ after the $J/\psi\eta$ kinematic fit selection. Data (solid line) and Monte Carlo (crosses) samples.

Acknowledgments

I would like to thank my advisor, Prof. Roberto Calabrese, for giving me the possibility to work in the E835 experiment. Besides his deep knowledge of physics and his experimental ability, working with him is a real pleasure.

Prof. Diego Bettoni demonstrated to trust my work involving me in interesting projects and always willing to help me whith brilliant discussions when I was losing the right way.

I am very grateful to them for having always helped me by sharing ideas until the end, reading the draft of this thesis and contributing to it with stimulating comments.

I am yery grateful to all the E835 collaborators for the realization of the experiment and the really nice time spent at Fermilab. A special thank to the spokepersons Prof. Rosanna Cester and Prof. Stephen Pordes for the tenacious guide of the collaboration. Working in such a pleasant group of skillful physicists is a great experience!

Many thanks also to Prof. Eleonora Luppi for all the discussion and the unfailing support here at the Physics Department in Ferrara.

The INFN supported part of my work. For this I wish to thank the director of the Ferrara section Prof. Pietro Dalpiaz, always demonstrating to appreciate my work.

Questa tesi conclude un periodo in cui, oltre a lavorare, ho avuto la fortuna di incontrare nuovi amici. Non ho dubbi che ricorderò molto volentieri tutti i momenti trascorsi insieme a Wander (insaziable divoratore di ottimi CD e profondo conoscitore di Chicago), Gigi (l'universo di D.&D. e il tè alla mattina), Margherita (e le chiacchierate a casa Torino), Federica (che mi ha sempre stracciato nella corsa), Gabriele (e le nostre cantate all'Auditorium), Giovanni (che ha abbandonato la carriera di chitarrista per poter lavorare con me a quest'analisi), Paolo (la buona cucina piemontese... e le orecchiette con i broccoli), Mirco (e il suo zoo), Giulio, Michelle e Arianna (e la loro simpatia e ospitalità) Ted, Matt e Seon-Hee ma anche Keith, Bombo, Nadia, Claudia, Palla e tantissimi altri.

Un carissimo saluto a tutti i miei amici, per non avermi fatto mancare il loro affetto anche nei periodi trascorsi lontano. Al ritorno ho ritrovato ancora tutta la vostra amicizia, imparando ad apprezzarla di più. Un grosso abbraccio a Mala,

China, Sabi, Carlo, Nicola, Reggio, Sara, Davide e Emanuela, Panna, Anna, Paola, Andrea e Eva, Corrado e Lara, Manuele, Panf... senza dimenticare Daniele, Enrica, Paolo, Riccardo, Marcella, Bruno, Cristiano, Luca, Enrico, Lorenzo, Alessio, Donato, Sara, Alfredo e tutti coloro che sicuramente avrò omesso ma non dimenticato.

Infine, il più grande riconoscimento va alla mia famiglia che mi ha sempre incoraggiato, pur non capendo appieno ciò che faccio. Anche se non lo capirete, questo lavoro è dedicato a voi.

Bibliography

[1] J. J. Aubert *et al.*, Phys. Rev. Lett. **33** (1974) 1404.

[2] J. E. Augustin *et al.*, Phys. Rev. Lett. **33** (1974) 1406.

[3] K. Hagiwara *et al.* [Particle Data Group Collaboration], Phys. Rev. D **66** (2002) 010001.

[4] S. Bagnasco *et al.* [Fermilab E835 Collaboration], Phys. Lett. B **533** (2002) 237.

[5] E. Eichten, K. Gottfried, T. Kinoshita, K. D. Lane and T. M. Yan, Phys. Rev. D **17** (1978) 3090 [Erratum-ibid. D **21** (1980) 313].

[6] W. Kwong, J. L. Rosner and C. Quigg, Ann. Rev. Nucl. Part. Sci. **37** (1987) 325.

[7] R. McClary and N. Byers, Phys. Rev. D **28** (1983) 1692.

[8] S. N. Gupta, C. J. Suchyta and W. W. Repko, Phys. Rev. D **39** (1989) 974.

[9] S. N. Gupta, J. M. Johnson, W. W. Repko and C. J. Suchyta, Phys. Rev. D **49** (1994) 1551 [arXiv:hep-ph/9312205].

[10] R. Gupta, arXiv:hep-lat/9807028.

[11] P. Boyle [UKQCD Collaboration], arXiv:hep-lat/9903017.

[12] P. Chen, Phys. Rev. D **64** (2001) 034509 [arXiv:hep-lat/0006019].

[13] M. Okamoto *et al.* [CP-PACS Collaboration], Phys. Rev. D **65** (2002) 094508 [arXiv:hep-lat/0112020].

[14] S. K. Choi *et al.* [BELLE collaboration], Phys. Rev. Lett. **89** (2002) 102001 [Erratum-ibid. **89** (2002) 129901] [arXiv:hep-ex/0206002].

[15] F. Halzen and A. D. Martin, John Wiley & Sons, Inc. (1987)

[16] T. A. Armstrong *et al.* [Fermilab E760 Collaboration], Phys. Rev. D **55** (1997) 1153.

[17] A. J. Smith, Ph. D. thesis, University of California, Irvine (1993).

[18] R. Van Royen and V. F. Weisskopf, Nuovo Cim. A **50** (1967) 617 [Erratum-ibid. A **51** (1967) 583].

[19] W. Kwong, P. B. Mackenzie, R. Rosenfeld and J. L. Rosner, Phys. Rev. D **37** (1988) 3210.

[20] G. T. Bodwin, E. Braaten and G. P. Lepage, Phys. Rev. D **51** (1995) 1125 [Erratum-ibid. D **55** (1997) 5853] [arXiv:hep-ph/9407339].

[21] M. L. Mangano and A. Petrelli, Phys. Lett. B **352** (1995) 445 [arXiv:hep-ph/9503465].

[22] H. W. Huang, H. M. Hu and X. F. Zhang, Phys. Rev. D **56** (1997) 5816.

[23] G. T. Bodwin, D. K. Sinclair and S. Kim, Int. J. Mod. Phys. A **12** (1997) 4019 [arXiv:hep-ph/9609371].

[24] M. Bace, Phys. Rev. D **4** (1971) 2838.

[25] W. R. Gibbs, L. Ai and W. B. Kaufmann, Phys. Rev. Lett. **74** (1995) 3740.

[26] E. Matsinos, Phys. Rev. C **56** (1997) 3014.

[27] S. Gardner and G. Valencia, Phys. Rev. D **62** (2000) 094024 [arXiv:hep-ph/0006240].

[28] G. S. Abrams *et al.*, Phys. Rev. Lett. **33** (1974) 1453.

[29] V. Luth *et al.*, Phys. Rev. Lett. **35** (1975) 1124.

[30] R. Brandelik *et al.* [DASP COLLABORATION Collaboration], Z. Phys. C **1** (1979) 233.

[31] M. Ambrogiani *et al.* [E835 Collaboration], Phys. Rev. D **62** (2000) 032004.

[32] B. Aubert *et al.* [BABAR Collaboration], Phys. Rev. D **65** (2002) 031101 [arXiv:hep-ex/0109004].

[33] G. S. Abrams *et al.*, Phys. Rev. Lett. **34** (1975) 1181.

[34] W. M. Tanenbaum *et al.*, Phys. Rev. Lett. **36** (1976) 402.

[35] E. Hilger *et al.*, Phys. Rev. Lett. **35** (1975) 625.

[36] A. Gribushin *et al.* [E672 and E706 Collaborations], Phys. Rev. D **53** (1996) 4723.

[37] Y. F. Gu and X. H. Li, Phys. Lett. B **449** (1999) 361 [arXiv:hep-ex/9812027].

[38] J. Z. Bai *et al.* [BES Collaboration], Phys. Lett. B **550** (2002) 24 [arXiv:hep-ph/0209354].

[39] T. Himel *et al.*, Phys. Rev. Lett. **44** (1980) 920.

[40] M. Oreglia *et al.*, Phys. Rev. Lett. **45** (1980) 959.

[41] R. Brandelik *et al.* [DASP Collaboration], The Decays Psi-Prime → Eta J / Psi, Pi0 J / Psi," Nucl. Phys. B **160** (1979) 426.

[42] W. Bartel *et al.*, Phys. Lett. B **79** (1978) 492.

[43] H. Goldberg, Phys. Rev. Lett. **35** (1975) 605.

[44] K. Gottfried, Phys. Rev. Lett. **40** (1978) 598.

[45] M. B. Voloshin and V. I. Zakharov, Phys. Rev. Lett. **45** (1980) 688.

[46] V. A. Novikov and M. A. Shifman, Z. Phys. C **8** (1981) 43.

[47] T. N. Pham, B. Pire and T. N. Truong, Phys. Lett. B **61** (1976) 183.

[48] T. M. Yan, Phys. Rev. D **22** (1980) 1652.

[49] J. Z. Bai *et al.* [BES Collaboration], Phys. Rev. D **62** (2000) 032002.

[50] T. A. Armstrong *et al.* [E-760 Collaboration], FERMILAB-PROPOSAL-P-835-REV.

[51] T. A. Armstrong *et al.* [E760 Collaboration], Phys. Rev. D **47** (1993) 772.

[52] G. Garzoglio, E835 internal memo 401 (unpublished) (1998).

[53] D. Allspach *et al.* [E835 Collaboration], Nucl. Instrum. Meth. A **410** (1998) 195.

[54] S. Trokenheim, M. Sarmiento, K. K. Seth and L. Bartoszek, Nucl. Instrum. Meth. A **355** (1995) 308.

[55] T. A. Armstrong *et al.* [E760 Collaboration], Phys. Lett. B **385** (1996) 479.

[56] L. Bartoszek *et al.*, Nucl. Instrum. Meth. A **301** (1991) 47.

[57] M. A. Hasan *et al.*, Nucl. Instrum. Meth. A **295** (1990) 73.

[58] S. Bagnasco *et al.*, Nucl. Instrum. Meth. A **424** (1999) 304.

[59] M. Ambrogiani *et al.*, Nucl. Phys. Proc. Suppl. **61B** (1998) 384.

[60] W. Baldini, D. Bettoni, R. Calabrese, E. Luppi, R. Mussa and G. Stancari, Nucl. Instrum. Meth. A **449** (2000) 331.

[61] R. Ray, J. L. Rosen, M. Masuzawa and J. Zhao, Nucl. Instrum. Meth. A **307** (1991) 254.

[62] M. D. Stancari, FERMILAB-THESIS-1999-47

[63] CERN Program Library Long Writeup W5013 (1993).

[64] W. Baldini, E835 internal memo 420 (unpublished) (2000).